# Development of Heterodyne High Field / High Frequency Electron Paramagnetic Resonance Spectrometer at 285 GHz

Petr Neugebauer

UNIVERSITÉ GRENOBLE 1 - JOSEPH FOURIER

THÈSE

# Développement d'un Spectromètre de Résonance Paramagnétique Électronique Haute Fréquence / Haut Champ Hétérodyne fonctionnant autour de 285 GHz

pour obtenir le grade de Docteur de l'Université Joseph Fourier
Discipline: Physique

Préesentée et publiquement soutenue par

**Petr NEUGEBAUER**

le 15 Janvier 2010

Thèse préparée au sein du Laboratoire National des Champs Magnétiques Intenses, CNRS, Grenoble, France.

| Composition du jury : | | |
|---|---|---|
| BARRA, Anne-Laure | LNCMI, CNRS, Grenoble, France | directeur de thèse |
| GAMBARELLI, Serge | CEA, Grenoble, France | examinateur |
| PARDI, Luca A. | CNR, Pisa, Italy | rapporteur |
| POTEMSKI, Marek | LNCMI, CNRS, Grenoble, France | examinateur |
| SMITH, Graham M. | University of St. Andrews, St. Andrews, UK | rapporteur |
| STEPANOV, Anatoli | Université Paul Cézanne, Marseille, France | préesident |

This thesis was submitted by:

**Petr NEUGEBAUER**

**Address:**

Laboratoire National des Champs Magnétiques Intenses, CNRS Grenoble
(Grenoble High Magnetic Field Laboratory)
25, avenue des Martyrs, BP 166
38 042 Grenoble Cedex 9
France

**Email address:**

petr.neugebauer@lncmi.cnrs.fr
petr.neugebauer@email.cz

This thesis was supervised by:

**Dr. Anne - Laure BARRA**

**Address:**

Laboratoire National des Champs Magnétiques Intenses, CNRS Grenoble
(Grenoble High Magnetic Field Laboratory)
25, avenue des Martyrs, BP 166
38 042 Grenoble Cedex 9
France

**Email address:**

anne-laure.barra@lncmi.cnrs.fr

**Electronic version of the thesis available on:** http://tel.archives-ouvertes.fr

to my family

# Acknowledgements

In this occasion, I would like to thank those people, who helped me during this work. It should be obvious that this thesis could not be achieved without significant help from them. First of all, I would like to thank the direction and management of the Grenoble High Magnetic Field Laboratory (GHMFL) as well as the administration department of the Institute Néel in Grenoble, which made my stay pleasant and comfortable. I want to express my acknowledgements to Anne-Laure Barra, Serge Gambarelli, Marek Potemski, Anatoli Stepanov who agreed to be a member of my jury, particularly to Luca A. Pardi and Graham M. Smith who were referees of my thesis.

I wish to emphasise my supervisor Dr. Anne-Laure Barra, who gave me the opportunity to study in GHMFL and introduced me such a challenging field as is the high field / frequency electron paramagnetic resonance (HF-EPR).

I would like express my thanks to Prof. Klaus Möbius (Berlin), Prof. Thomas F. Prisner (Frankfurt am Main), Prof. Jan Schmidt and Dr. Huib Blok (Leiden), and Dr. Graham M. Smith (St. Andrews), and to their groups, who were all the time "present" and open for discussion as well as were providing the possibility for short stays in their groups during my first steps in HF-EPR developments.

I express my gratitude to Prof. Andrea Cornia and his group in Modena, where beautiful Single Molecule Magnets (SMMs) were synthesised and used during my study in Grenoble and to Dr. Høgni Weihe (Copenhagen), who helped me with the simulation of single crystal spectra of a tetrairon(III) complex and whose programs were used for the simulation of all SMMs presented here. I cannot neglect Dr. Wolfgang Wernsdorfer (Grenoble) and Prof. Dominique Luneau (Lyon) for their collaboration as well as Dr. Milan Orlita (Grenoble), who introduced me the problematic of graphene and helped me a lot during my studies.

Then I would like to thank all the staff of the GHMFL. My thanks go to the staff of Nanofab of Institute Néel, where instrumentations necessary for preparation of microwave meshes were located.

Finally, of course to my family and my friends I want to express my sincere thanks.

Financial support:

This work would have not been possible without the financial support which came from the EU through EC-RTN **QuEMolNa** (FP6-CT-2003-504880) and NE **MagMaNet** (FP6-NMP3-CT-2005-515767), from the **CNRS** and the **COST P15 Action**, which I would like to acknowledge as well.

# Preface

My four year stay in Grenoble High Magnetic Field Laboratory (GHMFL) was devoted to the upgrade of an existing continuous wave High Field - Electron Paramagnetic Resonance (cw-HF-EPR) spectrometer, which relies on the quasi-optical (QO) microwave (MW) propagation using two phase-locked Gunn diodes (95 and 115 GHz, Table 3.1) MW sources associated with multipliers to produce higher harmonics for a multi-frequency EPR, to a pulsed HF-EPR spectrometer. This pulsed spectrometer should operate close to the frequency of 285 GHz. To achieve this, several steps were needed. First, a slow homodyne (bolometric) detection, used previously, had to be replaced by a faster heterodyne technique, enabling detection of short MW pulses. An excitation source which produces the MW pulses, as well as a cavity which enhances an excitation power, had to be bought and developed.

The new 283.2 GHz excitation source, based on a phase-locked Gunn diode (141.6 GHz), was bought in order to work a few GHz below the existing 285 GHz source. Consequently, the existing source can be used for the superheterodyne detection. To create MW pulses, a fast 140 GHz PIN switch was implemented in the excitation source after the Gunn diode. To enhance the excitation power on a sample, a Fabry - Pérot resonator (cavity) was designed as described in Chapter 4. The whole spectrometer with a Fabry - Pérot resonator and a superheterodyne detection is discussed in Chapter 3 in detail.

Nevertheless, problems with the new excitation source appeared and finally led to the failure of the Gunn diode before any pulsed experiment could be performed. The necessary replacement of the whole excitation source by a new one slowed down the progress in the development of the pulsed spectrometer. The delay in the fabrication of the new source and its adaptation to the already existing setup of the superheterodyne detection, did not allow us to perform the basic spin-echo experiment before submission of this thesis. However, the performance of the FP resonator was estimated, and some results were obtained with the superheterodyne detection.

During the development of the pulsed HF-EPR spectrometer, a new software for the existing cw-HF-EPR was created with the possibility to implement further features for the planned pulsed operation (Appendix B). The knowledge gained during the development of the FP resonator helped in the construction of a rotating sample holder for a single crystal orientation study as described in Chapters 3 and 4.

The HF-EPR spectrometer as well as the FP resonator rely on QO propagation, whose basics are given in Chapter 2, after a short introduction into HF-EPR. The experimental

parts of the thesis are devoted to the study of Single Molecule Magnets (SMMs) (Chapter 5) and to the study of Graphene (Chapter 6), where the whole experimental setup was successfully employed.

The work in GHMFL, extended my previous knowledge of work with MWs, high magnetic fields as well as work with the cryogenic equipment necessary for operating a HF-EPR spectrometer. I had the possibility to be involved in all the possible applications of HF-EPR, with difficult and beautiful experimental techniques as well as to be involved in European project dealing with molecular magnetism though QuEMolNa and MagMaNet networks. I was introduced to the French and the European EPR society which became very familiar to me. Finally, I learned to be independent both at work and in my personal life.

Petr Neugebauer
Grenoble 2009

# List of Abbreviations and Acronyms

| | |
|---|---|
| OD, 1D, 2D, 3D | zero, one, two, three dimensions, respectively |
| BPF | Band Pass Filter |
| BDPA | $\alpha,\gamma$-bisdiphenylene-$\beta$-phenylallyl (radical) |
| CEA | Commissariat à l'Énergie Atomique |
| CNR | Consiglio Nazionale delle Ricerche |
| CNRS | Centre National de la Recherche Scientifique |
| CR | Cyclotron Resonance |
| CW | continuous wave |
| DEER | Double Electron–Electron Resonance (or PELDOR) |
| DNP | Dynamic Nuclear Polarisation |
| DOS | Density of States |
| DP | Dirac Point |
| ENDOR | Electron Nuclei DOuble Resonance |
| EPR (ESR) | Electron Paramagnetic Resonance (Electron Spin Resonance) |
| ESEEM | Electron Spin Echo Envelop Modulation |
| FIR | Far InfraRed |
| FP | Fabry - Pérot Resonator |
| FWHM | Full Width at Half of Maxima |
| GHMFL | Grenoble High Magnetic Field Laboratory |
| HF-EPR | High Field / High Frequency Electron Paramagnetic Resonance |
| HYSCORE | Hyperfine Sublevel Correlation Spectroscopy |
| IF | Intermediate Frequency |
| ISMAR | International Society of Magnetic Resonance |
| INS | Inelastic Neutron Scattering |
| LL | Landau Level |
| LNCMI | Laboratoire National des Champs Magnétiques Intenses |
| MagMaNet | Molecular Approach to Nanomagnets and Multifunctional Materials |
| MW | Microwave |
| NMR | Nuclear Magnetic Resonance |
| ORTEP | Oak Ridge Thermal-Ellipsoid Plot Program, used for crystal structure illustrations. |

| | |
|---|---|
| PELDOR | Pulsed Electron DOuble Resonance (or DEER) |
| QHE | Quantum Hall Effect |
| QO | Quasi Optics |
| QTM | Quantum Tunneling Magnetisation |
| QuEMolNa | Quantum Effects in Molecular Nanomagnets |
| RADAR | RAdio Detection And Ranging |
| RLC | Resistor (R), Inductor (L), Capacitor (C) |
| RF | Radio Frequency |
| SMM | Single Molecule Magnet |
| STM | Scanning Tunneling Microscopy |
| STS | Scanning Tunneling Spectroscopy |
| SWN | Single Walled Nanotube |
| TEMPO | 2,2,6,6-Tetramethylpiperidine-1-oxyl (radical) |
| UV | Ultraviolet |
| VTI | Variable Temperature Insert |
| X, Q,...-Bands | Frequency bands, see Table 2 |
| ZFS | Zero Field Splitting |

Table 1: Table of physical constants used in the theory of magnetic resonance.

| **Constant** | **Symbol** | **Value** | **Unit** |
|---|---|---|---|
| Elementary charge | $e$ | $1.602 \times 10^{-19}$ | C |
| Planck constant | $h$ | $6.626 \times 10^{-34}$ | J.s |
| Reduced Planck constant | $\hbar = h/2\pi$ | $1.054 \times 10^{-34}$ | J.s |
| Boltzmann constant | $k_B$ | $1.381 \times 10^{-23}$ | $\mathrm{J.K^{-1}}$ |
| Speed of light | $c$ | $2.998 \times 10^{8}$ | $\mathrm{m.s^{-1}}$ |
| Electron mass | $m_e$ | $9.109 \times 10^{-31}$ | kg |
| Proton mass | $m_p$ | $1.673 \times 10^{-27}$ | kg |
| Neutron mass | $m_n$ | $1.675 \times 10^{-27}$ | kg |
| Bohr magneton | $\mu_B = e\hbar/2m_e$ | $9.274 \times 10^{-24}$ | J/T |
| Nuclear magneton | $\mu_N = e\hbar/2m_p$ | $5.051 \times 10^{-27}$ | J/T |
| Free electron $g$ factor | $g_e$ | 2.00231930 | 1 |
| Gyromagnetic ratio of free electron | $\gamma_e$ | $1.761 \times 10^{-11}$ | 1/sT |
| Reduced gyromagnetic ratio of free electron | $\gamma_e/2\pi$ | 28.025 | GHz/T |

Table 2: Frequency bands (IEEE Standard 521-1984) with corresponding wavelengths and resonance magnetic fields for Electron Paramagnetic Resonance (EPR) transition ($g_e = 2$), and the Electronic Industry Association (EIA) waveguide designation [1, 2]. The frequency ranges slightly differ from source to source for historical reasons.

| **Band** | **Frequency Range $f$ (GHz)** | **Wavelength Range $\lambda$ (mm)** | **Res. Field $B_{g_e=2}$ (T)** | **Waveguide Designation** |
|---|---|---|---|---|
| **X** | 8.2 - 12.4 | 36.59 - 24.19 | 0.29 - 0.44 | WR90 |
| **Ku** | 12.4 - 18.0 | 24.19 - 16.67 | 0.44 - 0.64 | WR62 |
| **K** | 18.0 - 26.5 | 16.67 - 11.32 | 0.64 - 0.95 | WR42 |
| **Ka** | 26.5 - 40.0 | 11.32 - 7.50 | 0.95 - 1.43 | WR28 |
| **Q** | 33.00 - 50.0 | 9.09 - 6.00 | 1.18 - 1.79 | WR22 |
| **U** | 40.0 - 60.0 | 7.50 - 5.00 | 1.43 - 2.14 | WR19 |
| **V** | 50.0 - 75.0 | 6.00 - 4.00 | 1.79 - 2.68 | WR15 |
| **E** | 60.0 - 90.0 | 5.00 - 3.33 | 2.14 - 3.22 | WR12 |
| **W** | 75.0 - 110.0 | 4.00 - 2.73 | 2.68 - 3.93 | WR10 |
| **F** | 90.0 - 140.0 | 3.33 - 2.14 | 3.22 - 5.00 | WR8 |
| **D** | 110.0 - 170.0 | 2.73 - 1.76 | 3.93 - 6.07 | WR6 |
| **G** | 140.0 - 220.0 | 2.14 - 1.36 | 5.00 - 7.86 | WR5 |
| **-** | 170.0 - 260.0 | 1.76 - 1.15 | 6.07 - 9.29 | WR4 |
| **-** | 220.0 - 325.0 | 1.36 - 0.92 | 7.86 - 11.61 | WR3 |
| **Y** | 325.0 - 500.0 | 0.92 - 0.60 | 11.61 - 17.86 | WR2 |

# Contents

# Résumé Chapitre 1

# Introduction à la Résonance Paramagnétique Electronique à Haut Champ / Haute Fréquence (RPE-HF)

Ce chapitre introduit les bases de la Spectroscopie de Résonance Paramagnétique Electronique à Haut Champ / Haute Fréquence (RPE-HF).

**Quelques aspects historiques de la Résonance Magnétique:** La technique RPE a été initiée par E. K. Zavoisky à la fin de la Deuxième Guerre Mondiale à Kazan (URSS, maintenant Russie) du fait de la disponibilité des composants microondes (MW) développés pour les RADAR. Le spectromètre RPE fonctionnait alors en mode continu (cw). Le premier spectromètre RPE en onde impulsionnelle est apparu à la fin des années soixante [3, 4, 5].

Le premier spectromètre de RPE-HF a été développé par le groupe de Ya. S. Lebedev à Moscou dans les années soixante-dix [6]. Dans les années quatre-vingt, plusieurs groupes ont suivi le travail de Lebedev: K. Möbius [7], J. H. Freed [8], J. Schmidt [9]. Dans la même période, un spectromètre RPE-HF multifréquence a été construit à Grenoble [10, 11]. Plus tard, un spectromètre en onde impulsionnelle fonctionnant à 600 GHz et utilisant un laser infra-rouge lointain (FIR) a aussi été construit [12]. En 1998, le groupe de P. C. Riedi a décrit un spectromètre RPE utilisant les techniques de Quasi-Optique (QO) [13] sous la forme qui est maintenant mise en œuvre dans la plupart des laboratoires de RPE-HF.

**Le Phénomène de Résonance Magnétique:** La RPE peut être expliquée simplement dans le cas de l'atome d'hydrogène qui a un électron ($S = 1/2$). Cet électron, en l'absence de champ magnétique extérieur, possède deux états dégénérés, appelés spin Up ($m = 1/2$) ou spin Down ($m = -1/2$). En présence d'un champ magnétique extérieur B, la dégénérescence de l'état de spin 1/2 est levée par l'effet Zeeman. La différence d'énergie $\Delta E$ (séparation Zeeman) entre les niveaux Up et Down vaut:

$$\Delta E = h f_{ex} = g_e \mu_B B, \tag{1}$$

où $g_e$ est le facteur g (facteur de Landé) de l'électron et $\mu_B$ est le magnéton de Bohr. Lorsque l'on applique un champ magnétique oscillant $B_1$ perpendiculaire au champ magnétique externe B et de fréquence d'oscillation $f_{ex}$ adaptée (Eq. (1.1)), l'absorption résonnante peut apparaître. Cependant, pour observer une résonance il est nécessaire d'avoir une différence de population entre ces deux niveaux d'énergie.

**Pourquoi la RPE Haut Champ / Haute Fréquence?:** Une des raisons pour utiliser des champs magnétiques élevés repose sur l'augmentation de la résolution spectrale quand on augmente le champ magnétique et la fréquence d'excitation MW comme illustré sur la Fig. 1.1. De même, la RPE-HF permet d'augmenter la résolution spectrale pour les mesures sur les systèmes non orientés, provenant de distribution d'orientations (poudre ou solution gelée). Enfin, les systèmes possédant un grand écart d'énergie en champ nul (zero field splitting, ZFS) associé à un spin entier ne peuvent être étudiés sans la RPE-HF. Les transitions paramagnétiques ont une différence d'énergie plus grande que l'énergie d'un photon de bandes X ou Q (Chapitre 5).

**Spectromètre RPE:** Pour obtenir les spectres d'absorption MW, le spectromètre RPE utilise une fréquence d'excitation $f_{ex}$ fixe et balaye le champ magnétique $B$ à travers la résonance. Le spectre est donc enregistré en fonction du champ magnétique B. Les spectromètres RPE-HF sont construits sur le même principe que le spectromètre RPE standard en onde continue (bande X), comme illustré par la Fig. 1.3. Notre spectromètre RPE-HF est décrit dans le Chapitre 3.

**Sensibilité du Spectromètre RPE:** La sensibilité absolue d'un spectromètre RPE en onde continue peut être exprimée (et mesurée) par le nombre de spins minimum que l'on peut détecter [14, 15, 16, 17]. La sensibilité théorique d'un spectromètre RPE dépend linéairement de la fréquence d'excitation $f_{ex}$ et de l'amplitude de modulation du champ $B_{mod}$, ce qui est favorable à la RPE-HF. La puissance MW $P_0$ au niveau de l'échantillon, qui intervient dans l'expression de la sensibilité, dépend de la source et des pertes le long du chemin jusqu'à l'échantillon. Cette dernière partie peut être nettement améliorée par l'utilisation de méthodes de propagation QO (Chapitres 2 et 3).

**Conclusion:** Ce chapitre a permis d'introduire rapidement la technique RPE, une méthode très puissante dans les domaines de la physique, de la chimie et de la biologie. Les avantages de la RPE-HF tels que la grande résolution spectrale ainsi que la possibilité d'étudier les systèmes à grand ZFS, etc. ont aussi été évoqués.

# Chapter 1

# Introduction to High Field / High Frequency Electron Paramagnetic Resonance (HF-EPR)

This chapter will introduce High Field / High Frequency Electron Paramagnetic Resonance (HF-EPR), starting from the first realization of this experimental technique by E. K. Zavoisky and going to the sophisticated techniques used nowadays. The basic principles of magnetic resonance as well as the advantages of going to higher magnetic fields and thus to higher excitation frequencies (HF-EPR) will be described. The HF-EPR spectrometer will be compared with a standard X-band EPR spectrometer in the last section.

We would like to refer to the Volume 22 of Biological Magnetic Resonance (Ref. [6]) devoted to HF-EPR, where chapters written by T. F. Prisner, J. H. Freed, D. E. Budil *et al.* discuss the main technical aspects of HF-EPR, as well as to Refs. [9, 14, 18, 19, 15, 20, 21, 22, 23, 24, 25, 26, 27, 28, 29, 30] where both reviews of HF-EPR and description of HF-EPR spectrometers are given. The MW components are described in details in Ref. [31].

## 1.1 Historical Aspects of Magnetic Resonance

The EPR technique was first invented by E. K. Zavoisky at the end of the Second World War in Kazan (USSR, today Russia) as a consequence of the availability of microwave (MW) components developed for RADAR.[1] He employed the newly developed MW techniques in the construction of the first EPR spectrometer. Two years later (in 1946), and independently of E. K. Zavoisky, the Nuclear Magnetic Resonance (NMR) technique was also developed by E. M. Purcell (NMR spectrometer) in the United States [32]. Whereas E. M. Purcell together with F. Bloch were honoured in 1952 by the Nobel prize: "for their development of new methods for nuclear magnetic precision measurements and discoveries in connection therewith" [33], the work of E. K. Zavoisky was only honoured posthumously by the prestigious ISMAR Award of the International Society of Magnetic Resonance in 1977 [18].

[1] The abbreviation RADAR comes from Radio Detection And Ranging. In RADAR MW frequencies are applied due to their low atmospheric absorption in rain, snow and fog.

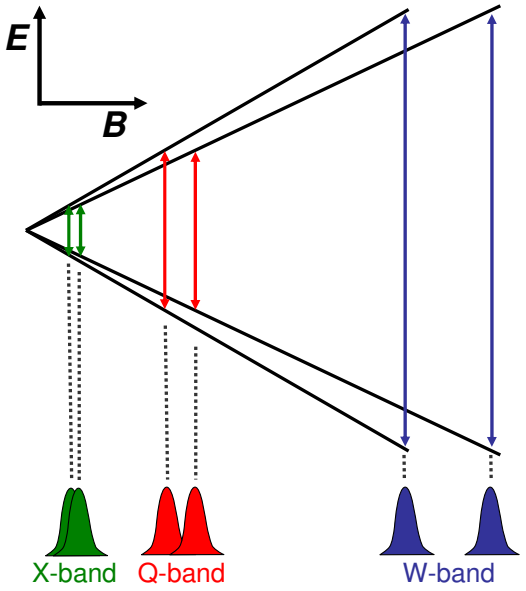


Figure 1.1: Two species of different $g$-values are very difficult to distinguish at the X-band frequency. The situation gets better for the Q-band frequency where we can already see the two lines presented. However, only the lines for the W-band frequency are fully separated. The resolution of a W-band spectrometer can be considered as one order of magnitude higher than that of a X-band spectrometer.

Both techniques, NMR and EPR, were used in the continuous wave (cw) regime until 1950, when E. L. Hahn realized an experiment with radio frequency (rf) pulses and observed a nuclear spin echo, which was the starting point for pulsed NMR techniques [34]. At the end of the 1960s, the first pulsed EPR spectrometer appeared [3, 4, 5]. It took a decade from the first pulsed NMR experiment to fully explore the possibilities of the pulsed NMR technique. At the same time, NMR and EPR techniques developed in different ways. Whereas for NMR it was much easier to create coherent MHz pulses and thus fully explore the pulsed technique, creating new pulse sequences, multi-dimensional experiments etc., the situation for EPR was completely different. Today NMR almost completely moved from cw to pulsed operation (except for rare solid state physics applications) as fast calculations on computers are available. The problem in creating sufficiently short pulses and detecting fast transitions, often more than one order of magnitude faster than in NMR, limited EPR mainly to cw-EPR applications for a long time.

In 1957, G. Feher published a work where he pointed out the importance of the increase of the irradiation frequency for the sensitivity and the resolution of EPR spectrometers [14], see Fig. 1.1. However, it took a few decades until this prediction could be experimentally realized. The first to overcome the initial problems was the group of Ya. S. Lebedev from Moscow in the 1970s with the implementation of the first 148 GHz EPR spectrometer [6]. The work of Lebedev was followed by several groups in the 1980s. The group of K. Möbius reported in 1985 an EPR spectrometer operating at 94 GHz [7]; the group of J. H. Freed pushed the limit to 250 GHz [8] in 1988. The first pulsed HF-EPR spectrometer operating at 95 GHz was reported in 1989 by the group of J. Schmidt [9]. Simultaneously, a multi-frequency high field EPR spectrometer was developed in Grenoble [10, 11]. In 1995 a pulsed HF-EPR spectrometer operating at 600 GHz was reported in Grenoble [12]. In 1998, the group of P. C. Riedi reported on an EPR spectrometer relying on QO techniques [13] in the form, that is used nowadays in most HF-EPR laboratories.

EPR methods are progressing now as fast as the NMR technique in the second half of the last century. Pulsed X-band, Q-band and W-band spectrometers are commercially

available and many pulsed experiments have become routine today (ESEEM, HYSCORE, etc.) [35]. Double resonance techniques such as PELDOR (DEER) enable determination of the structure and kinetic properties of large molecules, which for different reasons were impossible before [36] and have become a useful complementary method to NMR and X-ray diffraction techniques in structure determination. Furthermore, electrically detected EPR was recognized as a powerful tool in the semiconductor industry [37]. Moreover, both techniques NMR and HF-EPR start to be combined in Dynamic Nuclear Polarisation (DNP) experiments, where HF-EPR techniques are used to polarize nuclei via electronic cross relaxation (Overhauser effect, thermal effect, etc.) [38, 39].

The scope of EPR is very broad; it goes from solid state physics to chemistry and biology. Many techniques based on EPR have been omitted here, such as ENDOR, transient EPR, etc. The renaissance of EPR is largely due to the HF-EPR and the developments in this field. Whereas NMR remains fully pulsed technique, the EPR takes advantages of both cw-EPR and pulsed EPR modes. For example, the multi-frequency cw-EPR will remain a very powerful technique in the study of systems with large Zero Field Splittings (ZFS) [10, 18, 19, 40, 41].

## 1.2 Magnetic Resonance Phenomenon

Particles such as, for instance, electrons possess an intrinsic magnetic moment called spin, marked $S$. The total magnetic moment $J$ of a particle is then composed of its spin $S$ and its orbital moment $L$ ($J = L + S$). In presence of an external magnetic field $B$, the total magnetic moment starts to precess around the direction of the applied field $B$ with an angular (Larmor) frequency $\omega_L = \gamma B$ which depends on the nature of the magnetic moment. In the following, we will consider only electrons and the corresponding magnetic resonance, electron paramagnetic resonance (EPR). EPR can be easily explained on the hydrogen atom which has one electron ($S = 1/2$, $L = 0$). In zero external magnetic field, the electron has two degenerate eigenstates, called spin UP ($m = 1/2$) or spin DOWN ($m = -1/2$). The presence of an external magnetic field $B$ lifts the degeneracy of the $1/2$ spin state (Zeeman effect). The energy difference $\Delta E$ (Zeeman splitting) between the upper and lower state is

$$\Delta E = h f_{ex} = g_e \mu_B B, \tag{1.1}$$

where $g_e$ is the g-factor (Landé factor) of the electron and $\mu_B$ is the Bohr magneton. The above equation implies that the splitting is directly proportional to the external magnetic field $B$. Resonance absorption can occur if we apply an appropriate oscillating magnetic field $B_1$, perpendicular to the external field $B$, oscillating at frequency $f_{ex}$ (Eq. (1.1)). However, to observe a resonance absorption it is necessary to have a population difference between these two energy levels.

The main difference between EPR and NMR techniques is in the magnitude of the magnetic interaction, which is connected to the gyromagnetic ratio $\gamma = qg/(2m)$ where $q$ is charge, $g$ is g-factor and $m$ is the mass either of the electron or the nucleus which is about three orders of magnitude higher than for the electron. The difference in mass of the electron with respect to the nucleus leads to resonance at different frequencies. When in EPR the resonance is observed in the GHz range, in NMR occurs at MHz frequencies. The lower frequency makes the experiment technically easier, thus the NMR technique progress much faster than EPR.

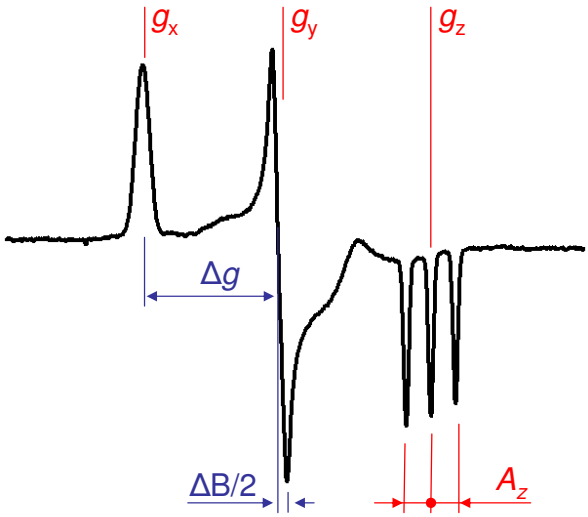


Figure 1.2: Demonstration of the high orientation selectivity, in the picture derivative of the absorption spectrum of a radical (TEMPO) taken at 285 GHz (10.2 T). The $g$-anisotropy as well as the hyperfine interaction is clearly resolved immediately from the spectra. The $g$-anisotropy will be very difficult to determine from low field X-band spectra with satisfying precision.

The interaction of a paramagnetic atom with a constant magnetic field is given by the Hamiltonian $\mathcal{H}$:

$$\mathcal{H} = \mathcal{H}_{elect} + \mathcal{H}_{cf} + \mathcal{H}_{LS} + \mathcal{H}_{SS} + \mathcal{H}_{Zee} + \mathcal{H}_{hfs} + \mathcal{H}_{Q} + \mathcal{H}_{N} \tag{1.2}$$

where the individual components are the following [15]:

| | | | |
|---|---|---|---|
| $\mathcal{H}_{elect}$ | electronic energy (optics) | $\approx 10^4 - 10^5$ | $\mathrm{cm}^{-1}$ |
| $\mathcal{H}_{cf}$ ($\mathcal{H}_{LF}$) | crystal (ligand) field energy (optics & FIR) | $\approx 10^3 - 10^4$ | $\mathrm{cm}^{-1}$ |
| $\mathcal{H}_{LS}$ | spin - orbit interaction | $\approx 10^2$ | $\mathrm{cm}^{-1}$ |
| $\mathcal{H}_{SS}$ | spin - spin interaction | $\approx 0 - 10^1$ | $\mathrm{cm}^{-1}$ |
| $\mathcal{H}_{Zee}$ | Zeeman energy | $\approx 0 - 10^1$ | $\mathrm{cm}^{-1}$ |
| $\mathcal{H}_{hfs}$ | hyperfine structure | $\approx 0 - 10^2$ | $\mathrm{cm}^{-1}$ |
| $\mathcal{H}_{Q}$ | quadrupole energy | $\approx 0 - 10^{-2}$ | $\mathrm{cm}^{-1}$ |
| $\mathcal{H}_{N}$ | nuclear spin energy | $\approx 0 - 10^{-3}$ | $\mathrm{cm}^{-1}$ |

The information gained from the EPR is usually the Zeeman energy and the hyperfine structure.

## 1.3 Why High Field / High Frequency EPR?

There are several reasons to go to higher fields and thus to higher frequencies in an EPR experiment. One of them, as already mentioned, is the enhancement of the spectral resolution with the increase of magnetic fields and MW frequencies. This can be schematically demonstrated on two species of slightly different $g$-values (Fig. 1.1). Whereas at X-band frequencies and even at Q-band frequencies, it could be very difficult to resolve the two components correctly, at W-band frequencies they could be already completely separated and the g-values resolved correctly (Fig. 1.1). The resolution of a W-band spectrometer can be considered as one order of magnitude higher than that of an X-band spectrometer; at 300 GHz the factor is about 30, if no broadening of the absorption lines is induced at higher frequencies.

For the same reasons, HF-EPR leads to enhanced spectral resolution for powder patterns, originating from orientation distribution. For instance, this will be the case of a sample containing only the radical TEMPO in a non oriented form (powder or frozen solution). This is demonstrated in Fig. 1.2, where the $g$-matrix principal values as well as the hyperfine interaction associated with the $z$-axis ($A_z$) are in HF-EPR clearly observed. The spectrum of the same sample at X-band frequency collapses in a single line signal with hyperfine structure. To obtain the $g$-anisotropy or to associate the field independent hyperfine interaction to the $z$-axis is much more complicated.

The general condition (high-field limit) for the spectral resolution could be written in the form:

$$\frac{\Delta B/2}{B} < \frac{\Delta g}{g_{iso}} \tag{1.3}$$

where $g_{iso} = (g_x + g_y + g_z)/3$ is the isotropic $g$ value, $\Delta B$ is the resonance linewidth, $B$ is the resonant field and $\Delta g$ is the smallest difference between the $g_x, g_y, g_z$ components of an anisotropic $g$-matrix, see Fig. 1.2. The condition could be adapted to a sample with two different species and two different $g$-components. Depending on the system under study, the high field limit will be reached at different fields.

Systems which show large zero field splittings (ZFS), often associated with integer spin values, are difficult to study without HF-EPR. The paramagnetic transitions are separated by an energy higher than a standard X-band or Q-band photon could probe. HF-EPR thus allows studying polynuclear systems as are single molecule magnets (SMMs) discussed in Chapter 5.

Similar to systems with large ZFS are systems with a large hyperfine interaction. In this case, when the magnitude of hyperfine interaction is of the order of several tesla (tens of GHz) [42] HF-EPR is needed as well.

## 1.4 HF-EPR Spectrometer

To measure MW absorption spectra, the EPR spectrometer uses a fixed excitation frequency $f_{ex}$ and sweeps the magnetic field $B$ through a resonance. The spectrum is thus recorded as a function of the magnetic field $B$. The absorption spectrum can be recorded by varying the excitation frequency $f_{ex}$ at a fixed magnetic field $B$ as well, but this manner is rather uncommon for technical reasons.

The HF-EPR spectrometer will be compared with a standard (X-band) cw-EPR spectrometer whose layout is displayed in Fig. 1.3. The EPR spectrometer is divided into six parts discussed below, with a focus on HF-EPR spectrometers. Spectrometers operating in pulsed mode (pulsed-EPR) are also mentioned.

**1. Microwave Source:** In contrast to cw-EPR experiments, where MW sources with a stable frequency (low phase and amplitude noise) and an adequate irradiation power are sufficient, in pulsed-EPR experiments high power sources providing short coherent pulses are needed.

Nowadays, X- or Q-band spectrometers use solid state sources like higher frequency spectrometers. Especially Gunn diodes, named after the physicist J. B. Gunn, phase-locked to a stable oscillator (quartz) are often used due to better phase noise characteristic with respect to free running Gunn diode [29]. Phase-locked Gunn diodes typically offer power

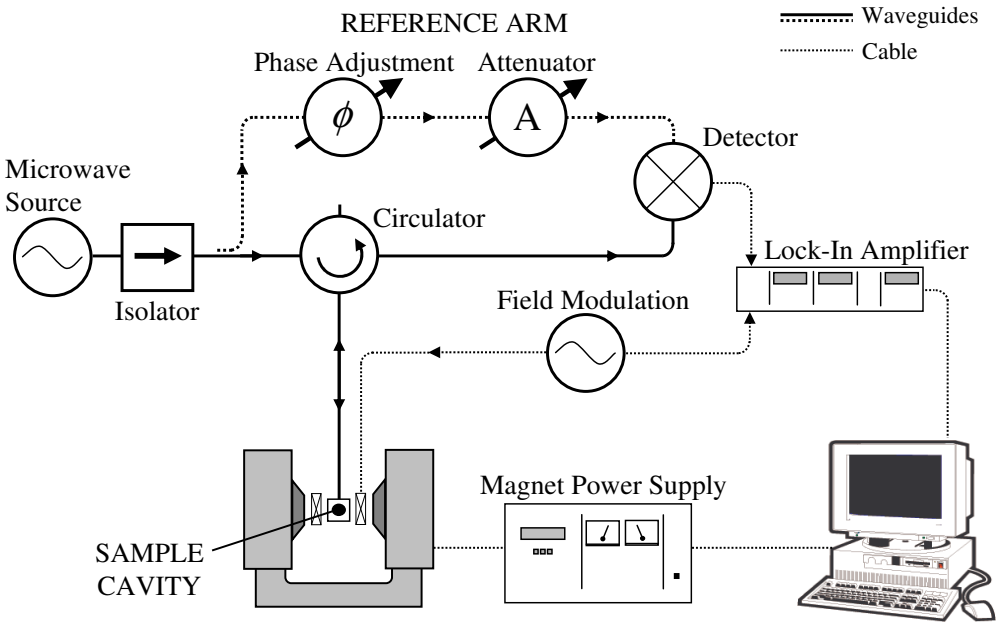


Figure 1.3: Scheme of a standard (X-band) cw-EPR spectrometer with homodyne detector. The MW bridge of the EPR spectrometer utilizes single mode rectangular waveguides and other MWs components depicted in the figure. Samples are usually placed into a single mode cavity in the center of a resistive magnet.

of $\sim 50\,\mathrm{mW}$ at $100\,\mathrm{GHz}$. The Gunn diodes can be followed by multipliers, semiconductor devices which multiply the basic frequency to higher harmonics allowing multi-frequency EPR in a simple spectrometer. The MW power at $300\,\mathrm{GHz}$ is then reduced to $\sim 10\,\mathrm{mW}$. An advantage of Gunn diodes is that they do not need high voltage power supplies (typically $\sim 10\,\mathrm{V}$). Nowadays, Gunn diodes, due to significant improvements of multipliers, are slowly replaced by sources based on actively multiplied low-frequency sources ($\sim 10\,\mathrm{GHz}$), usually dielectric resonance oscillators (DROs). Then these sources can provide more than twice higher MW power on the output in comparison to standard Gunn diodes.

MW pulses, in pulsed HF-EPR spectrometers, are produced by fast PIN switches (diodes). By changing a bias current through a PIN diode, it is possible to quickly (order of nanoseconds) change the RF resistance and thus to attenuate (switch) the MW. The PIN switches are usually implemented into a bridge after the basic frequency of the source (Gunn diode or DRO) and thus take advantage of the non-linearity of the multiplication which leads to a better isolation and a better MW pulse shape.

There are other MW sources which are used in HF-EPR, e.g. backward-wave oscillators (BWO) [43, 44], FIR Lasers [12, 45], Orotrons [46] and Gyrotrons [47] etc., which offer a very large excitation power but their use is rather rare due to their difficult use and high costs. The discussed solid state sources are widely used in atmospheric and RADAR applications and thus they are available for a reasonably low price.

**2. Microwave Bridge:** MW components (circulators, phase shifters etc.) and waveguides are used to direct (propagate) the MW and to create a MW bridge.

At high frequencies (> 100 GHz), single-mode rectangular waveguides, commonly used in standard EPR spectrometers (Fig. 1.3), become extremely lossy [8, 20]. This can be overcome by employing either oversized (overmoded) waveguides or the quasi-optical (QO) free space propagation.[2] Oversized waveguides have lower losses in comparison to a single-mode rectangular waveguide and are defined by the condition $2\pi a/\lambda > 1$, where $2a$ is the inner dimension of the waveguide. Such waveguides (circular or rectangular) can have smooth or corrugated walls. Smooth circular waveguides are simple metallic hollow pipes, and are used for frequencies over 500 GHz [10, 12], however corrugated waveguides are known to provide better propagation properties [13]. If the corrugation has a groove depth $d \approx \lambda/4$ and a period $p < \lambda/3$ (Fig. 2.2), the MW propagates with negligible losses and with an excellent polarisation purity, as will be discussed in Chapter 3.

While the waveguides are used to propagate MW, circulators (nonreciprocal devices) are used to direct the MW. A circulator is a multiport (usually 4 ports) device used to direct the MW power in the waveguide from a source (port 1) to a cavity (port 2) and then to direct the signal reflected from the cavity (port 2) towards a detector (port 3), see Fig. 1.3, usually the port 4 is terminated thus no-signal is coming to the source (port 1); In this way the circulator protects a MW source from backward travelling waves which are strongly attenuated by this component. However, an additional isolator is often used in front of the MW source to prevent any backward reflection.

Other components such as attenuators, phase shifters and detectors are not discussed here and can be found in Ref. [31]. Their QO equivalents will be discussed in Chapter 3.

**3. Sample Holders (Cavities):** Eventually, the sample should be placed in the maximum of the $B_1$ field of the excitation radiation $f_{ex}$. To maximize the excitation power, and thus $B_1$, the sample is placed in a resonant cavity. A MW resonance cavity, in general, is a metallic box fabricated from a highly conductive metal with dimensions defined by the MW wavelength. The MW enhancement depends on the type of the cavity (single-mode cavity, Fabry - Pérot resonator, etc.), on the quality factor $Q$ of the cavity as well as on the sample which often defines the suitable type of the cavity [16]. In the case of samples having low losses induced by the electrical component of MW (low dielectric losses), the number of spins in the cavity is important. This means that the best solution is to boost the sample holder to maximize the filling factor $\eta$ and thus the number of spins in the cavity [14, 16]. For this type of samples, non-resonant (double or single pass) cavities are well suited. For samples with higher losses (dielectric losses), the exciting MW power on the sample is crucial. Here cavities with high quality factors $Q$ are needed.[3] The optimal signal is obtained when the cavity is filled by a volume of sample such that it will reduce the unloaded quality factor $Q_0$ (quality factor of the cavity without presence of a sample) to the value $Q = 2/3Q_0$ [14].

Whereas cw-EPR can be performed without a resonant cavity [10, 11], in pulsed-EPR, the resonant cavity is an essential part of the spectrometer as the available MW power is often not sufficiently large to manipulated the magnetisation at reasonable time scales.

[2] The $TE_{01}$ mode in the standard rectangular waveguide WR-4 at 250 GHz has an attenuation higher than 12 dB/m (theoretical value) while the QO system, made by series of Teflon lenses, has the measured attenuation less than 1.5 dB/m [8].

[3] The quality factor $Q$ expresses a number of passages that the MW makes in the cavity before it is finally absorbed in the cavity walls and the filling factor $\eta$ expresses the ratio between the cavity and sample volume ($\eta \approx V_s/V_c$).

The fabrication of a single-mode cavity at high frequencies (about 200 GHz) is demanding; thus Fabry - Pérot (FP) resonators, in these cases, are more favourable, although they do not have such a good performance (conversion factor) as single-mode cavities. Nevertheless, they are often used due to their rather easy fabrication and manipulation with samples [8, 13, 21, 45, 48]. The group of J. Schmidt in Leiden has developed a single-mode cavity at a frequency of 275 GHz [49].

**4. cw-EPR Signal Detection:** A small varying (modulated) magnetic field at frequency $f_{mod}$ is applied to modulate the main magnetic field $B$ in order to increase the sensitivity of the measurement [14]. The detected phase sensitive signal is then the derivative of the absorption spectra. The modulation is performed by placing beside the sample a modulation coil.

The EPR signal can be detected either with a homodyne or a superheterodyne detector. Both detectors are based on the mixing of two frequencies. In the homodyne detection, the excitation MW is split in two arms, reference and irradiation, which afterwards are recombined (mixed) at the detector (homodyne detector), see Fig. 1.3. In the superheterodyne detection, the heterodyne principle[4] is employed, in which two sources with close frequencies are used. One frequency is used as the local oscillator $f_{LO}$ (reference) and the second one for the excitation $f_{ex}$ (irradiation); then these two frequencies are mixed at the detector, resulting in three high-frequency components ($f_{ex} + f_{LO}$, $2f_{ex}$, $2f_{LO}$) and one low-frequency component ($f_{ex} - f_{LO}$). The high-frequency components are filtered out and only the low-frequency component, called intermediate frequency $f_{IF}$, is used for further processing.

The homodyne detection is used with bolometers, which can cover broad range of MW frequencies and thus allow multi-frequency EPR to be performed with one detector. On the other hand, superheterodyne detection is used in pulsed EPR, for its fast response, and works only at one fixed frequency.

Special care should be given to phase noise in heterodyde systems, which is generally higher than in homodyne systems. The noise will be reduced if we phase-lock the excitation and local oscillator source to one stable oscillator (master reference), the phase and frequency noise characteristics of the heterodyne system are then strongly improved.

**5. Magnet and Cryostat:** In a standard X-band EPR spectrometer (Fig. 1.3), the magnetic field $B$ is supplied by an electromagnet (typically 1 T for X-band). However, for HF-EPR, magnetic fields of several Tesla are needed, therefore superconducting magnets (usually up to 16 T) are commonly used. When higher fields are necessary, high power resistive magnets are sometimes employed [12, 45].[5]

For measurements at low temperatures, samples are inserted into a cryostat. The simplest cryostat works only at helium (pumped) or nitrogen temperatures. However, cryostats, which enable measurements at several temperatures are very useful. The Vari-

[4] The heterodyne principle is a method invented by R. Fessenden. The method consists of mixing of two signals to obtain signals at the sum and at the difference of the frequencies. Whereas a superheterodyne detector is a device first realized by Edwin H. Armstrong during the First World War that uses the heterodyne method to translate a signal frequency to intermediate frequency $f_{IF}$.

[5] Curiosity: H. Soltner and B. Blümler showed that permanent magnets in Halbach geometry can be used for X-band experiment (EUROMAR2007 - Tarragona).

able Temperature Inserts (VTIs) allow measurements in the 1.5-300 K temperature range or even higher temperatures.

**6. Computer Control:** Commercially available EPR spectrometers are already equipped with appropriate software which allows the whole experiment to be driven. In our case of the home-built EPR spectrometer, the computer program had to be written and it is described in Appendix B. However, there are several EPR groups in the world which offer freewares (for example SpecMan[6]), which can be used to perform cw and pulsed EPR experiments, with standard features.

## 1.5 EPR Spectrometer Sensitivity

The absolute sensitivity of a cw-EPR spectrometer can be expressed in terms of the minimum detectable number of spins $N_{min}$ and is proportional to [14, 15, 16, 17]:

$$N_{min} \propto \frac{V_s T_s}{\eta Q} \left(\frac{\Delta f_{pp}}{f_{ex}}\right) \left(\frac{\Delta B_{pp}}{B_{mod}}\right) \left(\frac{F T_d \mathrm{BW}}{P_0}\right)^{1/2}, \tag{1.4}$$

where:

| | |
|---|---|
| $V_c, V_s, T_s$ | cavity volume, sample volume and temperature, |
| $\eta$ | filing factor, $\eta \approx V_s/V_c$ |
| $Q$ | quality factor, |
| $f_{ex}$ | spectrometer operating (excitation) frequency, |
| $\Delta f_{pp}, \Delta B_{pp}$ | peak to peak derivative linewidth, $\Delta f_{pp} = \gamma_e \Delta B_{pp}$, |
| $B_{mod}$ | modulation field amplitude, |
| $F$ | noise figure, |
| $T_d$ | detector temperature, |
| BW | bandwidth of the entire detecting system, |
| $P_0$ | incident MW power. |

As shown in Eq. (1.4), the theoretical EPR spectrometer sensitivity depends linearly on the excitation frequency $f_{ex}$ and on the modulation field $B_{mod}$, and this favours HF-EPR. However, this is not so straightforward. The linewidth in many cases increases with $f_{ex}$ and then a sufficient modulation field $B_{mod}$ can be difficult to obtain, which could lead to a decrease of the experimental sensitivity in the end [17]. The optimal modulation amplitude should be roughly $(1/8)^{th}$ of the peak to peak linewidth $\Delta B_{pp}$.[7] The strength of the modulation field depends on the modulation coil geometry and on the modulation frequency $f_{mod.}$. The choice of the frequency for the modulation is defined by the noise of the set-up (detector, frequency source, etc.). For low frequency spectrometers (X-band), it is about 100 kHz whereas for most HF-EPR spectrometers in can be decreased to a few hundred Hertz, which also allows higher modulation strength.

For a pulsed EPR spectrometer, the irradiation MW intensity is crucial for the sensitivity. To analyze samples with short relaxation times, the applied pulses have to be

[6] www.specman4epr.com

[7] Too big a modulation field leads to a distortion of the linewidth as well as to a reduction of sensitivity in the end, see Ref. [22].

short and intense enough ($B_1$) to flip the spins. The length of the pulse ($T_{Pulse}$) and the magnetic field $B_1$ at the sample are related by:

$$T_{Pulse}^{-1} \propto B_1 = c\sqrt{QP_0}, \tag{1.5}$$

where the power conversion factor $c$ [20, 50] is a function of the excitation MW $f_{ex}$ and of the cavity:

$$c \propto \sqrt{\frac{\mu_0}{V_c f_{ex}}} \approx \sqrt{\mu_0} f_{ex}. \tag{1.6}$$

Cylindrical single-mode cavities have the advantages of the maximum MW $B_1$ field for a given input power and of a large conversion factor $c$ due to a smaller cavity volume $V_c$. EPR spectrometers can have several hundred times better sensitivity with a single-mode cavity than with a Fabry - Pérot resonator [9, 16]. This makes them desirable especially for pulsed EPR experiments. The fabrication of a tiny cavity for a HF-EPR spectrometer, operating close to 300 GHz is not easy, but, it is possible [49]. On the other hand, the size and volume of the sample is even tinier, which makes the sample loading difficult. So, there is some trade-off between the use of a single-mode cavity and a Fabry - Pérot resonator.

The MW power $P_0$ at the sample, which appears in the sensitivity formula for cw-EPR and for the pulsed EPR, is given by the source power and by the losses on the pathway to the sample. This part can be largely improved if the QO propagation is employed. If QO implementation is for any reason difficult, for example inside a cryostat[8], then oversized (overmoded) waveguides can be utilized and the coupling to QO is easily made.

For the overall sensitivity of an EPR spectrometer, the above mentioned effects are not the only ones to take in account. One has to eliminate potential sources of additional noise as e.g. helium bubbles in the cryostat, microphonics vibration of the cavity induced by the modulation coil, frequency instability and phase noise of the MW source etc.

## 1.6 Conclusion

This chapter briefly introduced the EPR technique, a very powerful tool in the field of physics, chemistry and biology. The advantages of HF-EPR such as the high spectral resolution, the possibility to study systems with large ZFS, etc. were mentioned. The technique allows the study of SMMs, as discussed in the experimental part of the thesis (Chapter 5).

A HF-EPR spectrometer has been described referring to the components of a standard X-band EPR spectrometer (Fig. 1.3). The same structure is used in the description of our HF-EPR spectrometer (Chapter 3). The spectrometer relies on QO (free space) propagation which allows replacing all the MW components known from the standard EPR spectrometer, with QO components. The basis of QO is presented in Chapter 2 and used as a starting point for the design of the FP resonator discussed in Chapter 4.

[8] Some groups apply and use the QO optical propagation in a warm bore of the magnet [8, 51]. Such systems consist of series of Teflon lenses which refocus the MW inside the magnet bore. However, these systems usually operate at one temperature and a fixed frequency. The measurements at different temperatures are not possible or are limited due to the temperature effect on the system dimensions (dilatation). The broadband multi-frequency EPR is limited or not allowed due to lenses used in the system (dispersion).

# Résumé Chapitre 2

## Quasi-optique

Depuis la fin des années 80, plusieurs groupes ont commencé à remplacer dans leurs systèmes RPE-HF les guides d'ondes par des montages de propagation quasi-optique (QO) plus performants [6, 11]. Les avantages d'un montage QO pour la RPE-HF sont multiples : le premier (et le plus important) est de réduire les pertes lors de la propagation des micro-ondes ; le second est de permettre de réaliser l'ensemble des composants de base utilisés habituellement dans un spectromètre RPE classique (Fig. 3) en gardant les mêmes propriétés (fonctions). De plus, les éléments d'un montage QO sont conçus pour fonctionner sur une large bande de fréquences. Dans l'approche QO, la propagation de l'onde est décrite par un faisceau Gaussien.

**Faisceau Gaussien:** Le faisceau Gaussien (Fig. 2.1) est décrit par les équations suivantes:

$$\boxed{\mathcal{R} = z + \frac{1}{z}\left(\frac{\pi w_0^2}{\lambda}\right)^2}, \tag{1.7}$$

$$\boxed{w = w_0\left[1 + \left(\frac{\lambda z}{\pi w_0^2}\right)\right]^{1/2}}, \tag{1.8}$$

$$\boxed{\tan\phi_0 = \frac{\lambda z}{\pi w_0^2}}, \tag{1.9}$$

où $\mathcal{R}$ est le rayon du front de l'onde, $w$ le rayon pour lequel le champ électrique $E$ atteint la valeur $1/e$ par rapport à sa valeur axiale (maximale) pour la position $z$ (Fig. 2.1(b))). $w$ est le rayon du faisceau et $\phi_0$ le déphasage du faisceau Gaussien. Le paramètre $w_0$ qui apparait dans chaque équation est la taille du faisceau. Il définit aussi la position $z = 0$ et représente la valeur minimale du rayon $w$.

**Composants du montage QO:** Le faisceau Gaussien se propage entre les composants QO qui sont analogues à ceux utilisés pour l'optique classique, i.e. miroirs, lentilles, polariseurs, réseaux etc. Dans le cas de notre spectromètre RPE (Fig. 3.2), ces composants sont situés à l'extérieur du cryostat ce qui permet de remplacer le système de propagation d'onde au travers de guides surdimensionnés par un montage plus efficace, évitant les pertes grâce à une propagation dans l'espace (non confinée). Par contre, à l'intérieur du cryostat, un guide d'onde surdimensionné est nécessaire. Une attention toute particulière doit être portée à l'alignement et au couplage des composants. Tout mauvais alignement provoque des pertes de puissance significatives du faisceau propagé.

**Interféromètre Fabry - Pérot (Résonateur):** L'interféromètre Fabry -Pérot (FP) (souvent appelé résonateur) est un composant sélecteur de fréquence très utilisé en optique. En RPE, il sert à augmenter la puissance des micro-ondes sur l'échantillon. Le schéma général d'un résonateur FP est présenté sur la Fig. 2.6. Dans un résonateur FP, la résonance intervient quand le déphasage du chemin optique entre les miroirs est un multiple de $2\pi$.

Dans le cas des résonateurs FP, c'est la finesse $F$ et non le facteur de qualité $Q$ qui définit la valeur du résonateur. Cependant, ces quantités sont reliées par l'équation $Q = qF$. La valeur théorique de la finesse $F$ dépend seulement des coefficients de réfraction $r_1$ et $r_2$ des miroirs [52]. La finesse $F$ est déterminée expérimentalement selon:

$$F \approx \frac{\text{fenêtre spectrale “libre” (A)}}{\text{largeur de raie à mi-hauteur (B)}}. \tag{1.10}$$

Où la fenêtre spectrale libre A est la distance entre deux résonances successives et B est la largeur de raie à mi-hauteur du pic de résonnance. Ainsi, les résonateurs FP avec une valeur de $F$ élevée présentent des pics de résonance plus fins (Fig. 4.8). Les résonateurs FP peuvent être stables ou instables: dans le premier cas, le paquet d'ondes est refocalisé périodiquement par les miroirs lors de son trajet optique tandis que dans le second cas, le signal est dispersé au fur et à mesure de sa propagation. La stabilité des résonateurs FP dépend de leur géométrie comme illustré par le diagramme de stabilité associé (Fig. 2.7) où chaque point correspond à une géométrie particulière de résonateur.

**Conclusion:** Dans ce chapitre, nous avons donné une vue d'ensemble des bases de la Quasi-Optique et de son application aux spectromètres RPE-HF. Nous avons décrit la propagation du faisceau micro-onde Gaussien et l'utilisation de la QO en RPE-HF. La propagation des micro-ondes au travers du guide d'onde a été décrite de façon quantitative. Nous avons aussi introduit la théorie des résonateurs FP basée sur la propagation du faisceau gaussien. Cette théorie est discutée plus en détails dans les chapitres 3 et 4 dédiés respectivement au spectromètre RPE-HF et à la conception du résonateur FP.

# Chapter 2

# Quasioptics

Quasioptics (QO) covers the wavelength range in between ray optics ($\lambda \longrightarrow 0$) and diffraction optics ($\lambda \gtrsim$ system dimensions); it is a more realistic approximate solution to the equation of propagation of light than the ray optics description. QO is more complicated than ray optics but is easier than diffraction optics. In QO systems, the radiation is elegantly described by a theory of Gaussian beams [53].

The QO approach finds its origin in astronomy where radio and MW frequencies are under study. This approach became very important to radio astronomy since it allows low-loss propagation of the signal, with the possibility to work in a broad frequency range at least when non-dispersive optical components such as mirrors are concerned.

From the end of the 1980s several groups started to replace lossy waveguides by QO propagation in their HF-EPR systems [8, 13]. The advantages of using QO in HF-EPR are manifold. The first and the most important benefit is the low-loss propagation of the MW. Second, the QO allows building up of all the basic components which are used in a classical EPR spectrometer (Fig. 1.3) with the same properties. Also the QO elements can be designed for a broad frequency range and not a unique frequency, which allows building multi-frequency EPR spectrometers (Table 3.1). Nowadays, in the HF-EPR community the QO is already well established as being essential part of any HF-EPR spectrometer [8, 13, 26, 54, 55, 56, 57].

The goals of this chapter are to introduce the basis of the Gaussian beam propagation of millimetre and submillimetre waves and its application in HF-EPR as well as to give a brief introduction into the theory of Fabry - Pérot resonators. The theory presented here will help to understand our EPR system and its development described in Chapters 3 and 4. This short presentation is mostly inspired by a book from P. F. Goldsmith [53] where the QO is described in detail and by the work of G. M. Smith *et al.* [13]. The theory of the Fabry - Pérot Resonator is inspired from works of H. Kogelnik *et al.* and G. D. Boyd *et al.* [58, 59, 60].

## 2.1 Gaussian Beam

### 2.1.1 Fundamental Mode in Cylindrical Coordinates

An optical system can be described by Gaussian beams when the beam is well collimated during its propagation. This happens when the system dimensions (lenses, mirrors, prop-

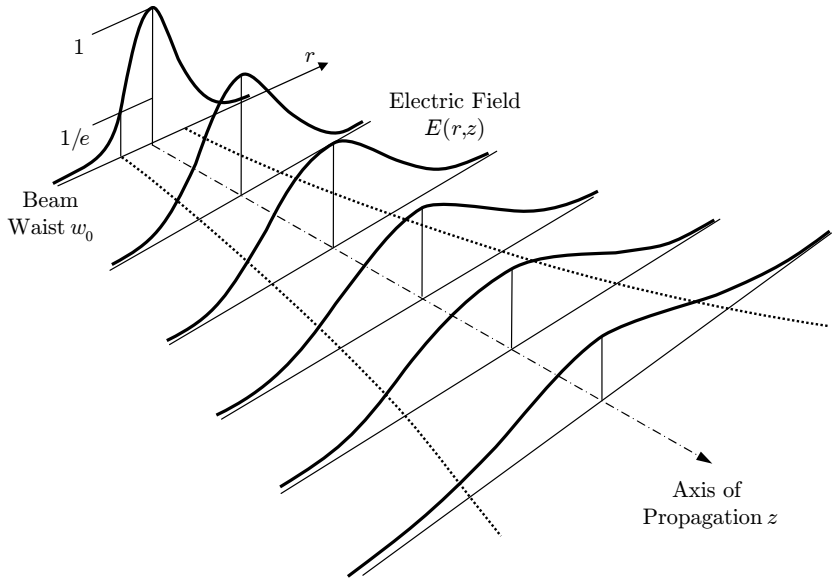


(a)

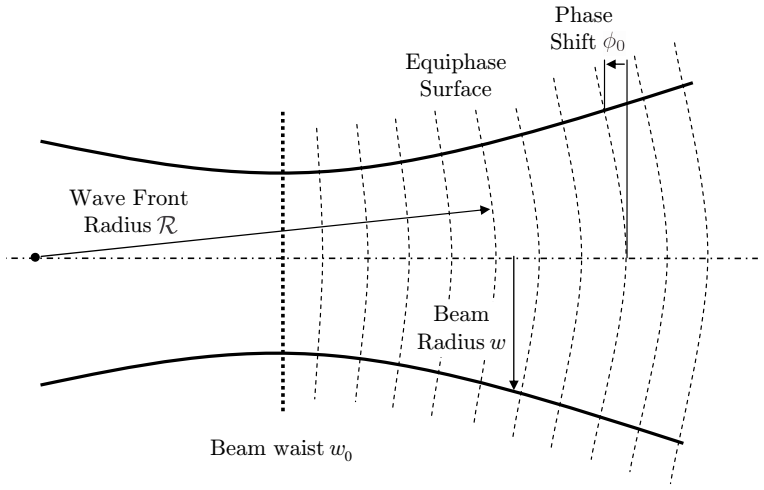


(b)

Figure 2.1: Schematic picture of the Gaussian beam propagation. (a) the electric field distribution *E(r,z)* along the propagation axis $z$, (b) the *E(r,z)* equiphase surface at a height of $1/e$ showing the parameters of Gaussian beam.

agation distance etc.) are larger than the beam wavelength (but not enough to apply ray optics). This is the case of QO systems, where the beam remains well collimated and the diffraction effects are thus limited during the propagation. To be still well described by a fundamental Gaussian beam, the system should work with an angular divergence which is smaller than 0.5 radians (about 30 degrees) from the propagation axis.

The above statement is nothing more than a paraxial approximation of the propagation equation for the collimated wave, for which the Gaussian beam is the solution. Mathematically speaking the paraxial approximation is based on two assumptions: *i*) the variation of the beam amplitude of the wavefront (of the beam) is small over a distance comparable to the wavelength $\lambda$; and *ii*) this variation should then be smaller than the variation perpendicular to the propagation axis[1].

The fundamental Gaussian beam (see Fig. 2.1) is described by the equations:

$$\boxed{\mathcal{R} = z + \frac{1}{z}\left(\frac{\pi w_0^2}{\lambda}\right)^2}, \tag{2.1}$$

$$\boxed{w = w_0\left[1 + \left(\frac{\lambda z}{\pi w_0^2}\right)\right]^{1/2}}, \tag{2.2}$$

$$\boxed{\tan\phi_0 = \frac{\lambda z}{\pi w_0^2}}, \tag{2.3}$$

where $\mathcal{R}$ is **the wave front radius**, $w$ represents the radius at which the electric field $E$ falls to $1/e$ relative to its axial (maximal) value for the $z$ position (see Fig. 2.1(b)). $w$ is called **the beam radius** and $\phi_0$ is **the Gaussian beam phase shift**. The parameter $w_0$ which appears in each equation is called **the beam waist radius** or simply **the beam waist**. The beam waist $w_0$ defines also the position $z = 0$ and represents the minimal size of the beam radius $w$.

The normalised[2] electric field distribution *E(r,z)*, shown in Fig. 2.1(b), is described by the expression:

$$\boxed{E(r,z) = \left(\frac{2}{\pi w^2}\right)^{1/2} \exp\left(\frac{-r^2}{w^2} - ikz - \frac{i\pi r^2}{\lambda\mathcal{R}} + i\phi_0\right)}. \tag{2.4}$$

Eqs. (2.1) to (2.4) completely describes the behaviour of the fundamental Gaussian beam mode in the paraxial region. The above expressions represent a good approximation as long as the apertures of the mirrors or lenses used are large enough and only a small amount of light power is being lost. To eliminate losses refocusing elements have to be implemented regularly.

The Gaussian beam described here is the simplest (fundamental) solution of the paraxial wave equation. It is the most important and the most widely used. However, in some cases, we have to deal with solutions that have a more complex variation of electric and

[1] The limiting case of the paraxial approximation is a plane wave. The wavefront is planar (unchanged) and the perpendicular variation does not exist (the wave amplitude is constant).

[2] The power carried by the wave is proportional to square of electric intensity $E$, thus the normalization is obtain by integration over the area of the beam $\int_0^\infty \mid E \mid^2 2\pi r dr = 1$.

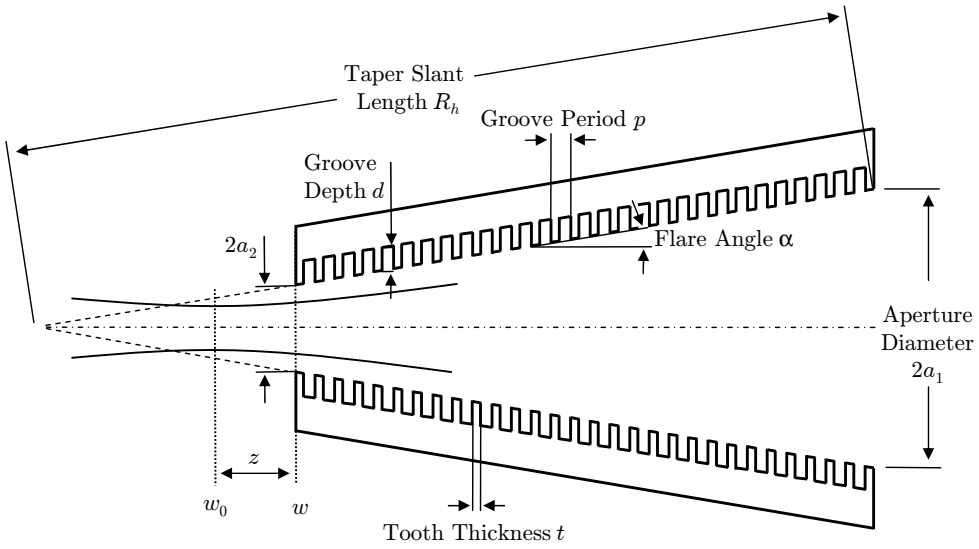


Figure 2.2: Cross section of a conical corrugated taper. In our set-up, we use a taper with the length of 136 mm with aperture diameters of $2a_1 = 18$ and $2a_2 = 6$ mm giving the flare angle $\alpha = 2.53°$. The location $z$ and the size of the beam waist $w_0$ after passing through such a corrugated taper for frequencies 190, 230, 283.2 and 285 GHz can be found in Table 4.5.

magnetic fields along the direction perpendicular to the propagation axis. These are **the higher order Gaussian modes**.

The higher order modes are characterized by a beam radius $w$ and a wave front radius $\mathcal{R}$ that have the same behaviour as the fundamental mode presented above. The differences are in the phase shifts $\phi_0$ and in the complex variation of the electric (magnetic) field along the direction perpendicular to the propagation axis.

Higher order modes in a QO system should be avoided as they take away energy from the fundamental mode and thus cause signal losses as they do not generally couple to the detection system. Moreover, they are not suited for the use of FP resonators (discussed later) as they result in a complex instead of a uniform irradiation over the sample. These modes can be suppressed by a proper design of the QO components and of their coupling, as discussed later.

More details on the Gaussian beam propagation theory are presented in Appendix A and a complete derivation can be found in the book of P. F. Goldsmith [53].

### 2.1.2 Inverse Formulas for the Gaussian Beam

In practice we may know only the size of the Gaussian beam $w$ from its measurement. Furthermore, that this beam is produced by a feed horn at a specific position $z$ (Fig. 2.2). In this case, we need to use "inverse" formulas, in the sense of working back to the beam waist $w_0$, to determine the unknown parameters of the beam. The inverse formulas for the beam waist $w_0$ and its location $z$ are:

$$w_0 = \frac{w}{[1 + (\pi w^2/\lambda\mathcal{R})^2]^{1/2}} \tag{2.5}$$

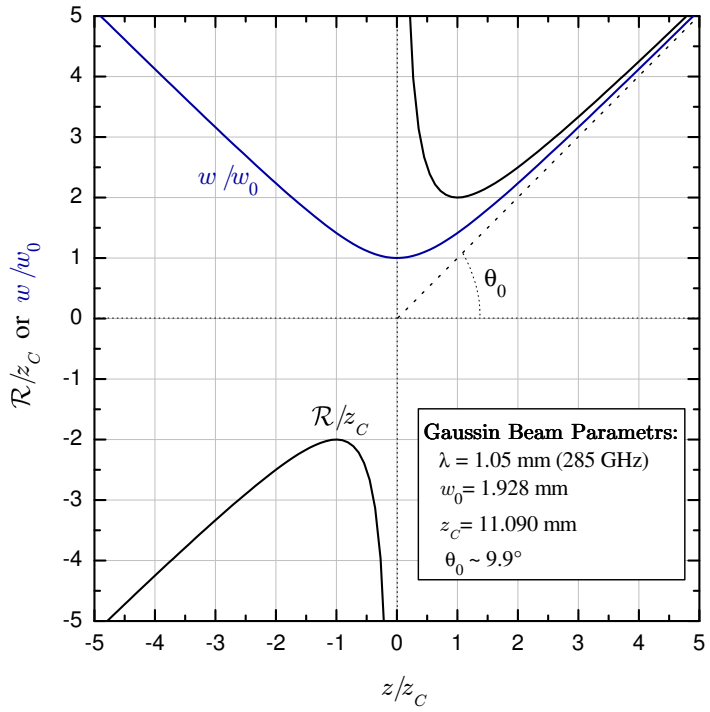


Figure 2.3: Variation of the normalized beam radius $w$ to beam waist $w_0$ and the normalized wave front radius $\mathcal{R}$ to confocal distance $z_c$ of Gaussian beam as a function of distance $z$ from the beam waist. The dotted line illustrates asymptotic growth of the Gaussian beam in far field region $z \gg z_c$ characterized by the divergence angle $\theta_0$.

and

$$z = \frac{\mathcal{R}}{1 + (\lambda\mathcal{R}/\pi w^2)^2}. \tag{2.6}$$

The use of the inverse formulas will be illustrated for the case of our system in Chapter 4.

Our EPR spectrometer (described in detail in Chapter 3) uses a circular corrugated waveguide, for the propagation of the MWs in the cryostat, with a focusing taper in the end (Fig. 2.2). The knowledge of the MW beam waist $w_0$ and its location $z$, produced by the corrugated taper, is important for the proper MW coupling into the Fabry - Pérot resonator attached to the taper.

A circular corrugated waveguide (taper) with an aperture $a$ (Fig. 2.2) will be optimally coupled (maximal power transfer of the fundamental mode) to the surrounding system when the Gaussian beam radius $w$ at the aperture $a$ is:

$$w = 0.644a. \tag{2.7}$$

Eq. (2.7) is only valid for circular corrugated waveguides supporting the $HE_{11}$ mode [61]. For other types of waveguides a proper equation can be found in [53].

### 2.1.3 Confocal distance: Near and Far Field

The terminology of the confocal distance comes from the resonator theory [58, 59, 60], where the **confocal distance** $z_c$ plays a major role in optimizing the system. Sometimes, the confocal distance is called the **confocal parameter** or the **Rayleigh range**. The confocal distance $z_c$ is defined as:

$$z_c = \frac{\pi w_0^2}{\lambda}, . \tag{2.8}$$

Using that definition, Eqs. (2.1), (2.2) and (2.3) for the Gaussian beam can be rewritten in more compact forms:

$$\mathcal{R} = z + \frac{z_c^2}{z} \tag{2.9}$$

$$w = w_0 \left[1 + \left(\frac{z}{z_c}\right)^2\right]^{1/2} \tag{2.10}$$

$$\tan \phi_0 = \frac{z}{z_c}. \tag{2.11}$$

If we look closely at the equations, we see that in the region from $z = 0$ to $z = z_c$ the Gaussian beam parameters are changing appreciably, as shown in Fig. 2.3 (see also Table 4.2 on page 52). The region $z \ll z_c$, close to the beam waist $w_0$, is called the **near field region** and the region where $z \gg z_c$ is called the **far field region**. The beam radius $w$ is essentially unchanged from the beam waist $w_0$ in the near field region. The beam radius $w$ is reaching the value $w = \sqrt{2}w_0$ at the confocal distance $z_c$. We can say that the Gaussian beam propagates to the confocal distance without any significant growth and remains essentially collimated. At the distance $z_c$ the wavefront radius $\mathcal{R}$ is reaching its minimal value $2z_c$ and the phase shift $\phi_0$ is equal to $\pi/4$. In the far field region the behaviour of the beam radius $w$ tends towards an asymptotic (linear) growth with the angle $\theta_0$:

$$\theta_0 = \lim_{z \gg z_c} \left[\arctan\left(\frac{w}{z}\right)\right] = \arctan\left(\frac{\lambda}{\pi w_0}\right). \tag{2.12}$$

In the far field region the wave front radius $\mathcal{R}$ increases also linearly with $z$. In this limit, the wave front radius is equal to $z$.

## 2.2 QO Components

We are going to describe briefly the QO components which are needed for a HF-EPR spectrometer. All these components have clear analogues in classical optics, i.e. mirrors, lenses, polarizers, beam splitters etc. In the case our EPR spectrometer (Fig. 3.3), the previous lossy propagation technique using oversized waveguides has been replaced by low-loss free-space propagation for the propagation outside of the cryostat. Only in the cryostat where the conditions for the free space QO propagation are not fulfilled, an oversized corrugated waveguide is used. The advantages of such waveguides will be discussed later.

The QO components, discussed in the text below, used in the EPR spectrometer (Fig. 3.3) are arranged in an off-axial manner. The free standing waves between the components are then strongly suppressed.

In QO systems, the use of **mirrors** (reflective surfaces) are more favourable than **lenses** for several reasons. One of them is their non-dispersive behaviour, which allows designing a QO system with a broader frequency range. Whereas metallic mirrors reflect and eventually refocus MWs with negligible losses, lenses need antireflection coatings to reach similar performances and these coatings are frequency dependent. Mirrors are also usually arranged in off-axial manner thus suppressing unwanted standing waves. However, in this case, the system should be carefully designed to minimize polarisation errors as well as beam distortion.

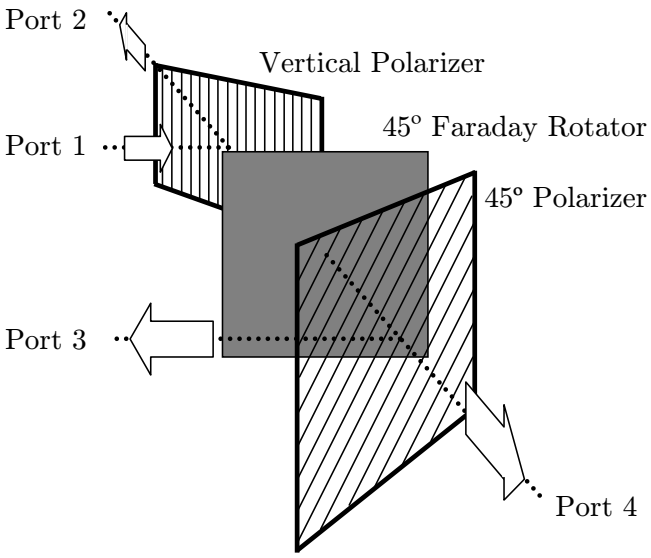


Figure 2.4: Function of a QO circulator based on a Faraday rotator and two wire polarizers is depicted in the figure. The QO circulator allows to propagate light (MW) only in one direction. A vertically polarised signal entering in Port 1 leaves $-45°$ polarised at Port 4. The signal reflected back to Port 4 leaves horizontally polarised at Port 2 and the backward reflected signal from Port 2 appears at Port 3 45° polarised. Thus the signal circulates between the ports 1-4-2-3-1 etc., hence the name circulator.

QO MW **polarizers** consist of grids of metallic wires with a defined diameter and spacing. If the incident MW has its electric field component perpendicular to the wires (copolar), it passes through the polarizer whereas the MW with parallel polarisation (crosspolar) cannot. By assembling two polarizers with mutually rotated polarisation axes a MW **QO attenuator** can be created.

A **Faraday rotator** is a plate of a certain thickness made from a ferrimagnetic material (ferrites) with its magnetisation parallel to the propagation of the light [62]. The magnetisation in the plate leads to a rotation of the light (MW) polarisation via Faraday (magneto-optic) effect. This particular geometrical configuration (light propagation $\parallel$ magnetisation) and the non-reciprocity of the Faraday effect induce that the MW polarisation is always rotated in a given direction, for incoming or outgoing MW. For example, a 45° Faraday rotator will rotate vertically polarised MW from a source of 45° and the backward reflected MW again of 45° but not back to vertical polarisation instead to horizontal polarisation. The angle over which the polarisation is rotated depends on the magnetic material used (Verdet constant), the thickness of the plate, and on the MW frequency. To keep a constant rotation, the Faraday rotator has to be used only for a certain frequency range, otherwise it has to be replaced by a more adapted one. Faraday rotators are used to build QO circulators or isolators.

A **QO circulator (isolator)** is obtained from the combination of one Faraday rotator with two wire polarizers (Fig. 2.4). Its role in the EPR spectrometer was already described in Chapter 1. The description and function of a QO circulator is depicted in Fig. 2.4.

**Phase shifts** in QO can be easily introduced by a movable mirror, which is often a roof mirror. The movement of the mirror introduces a path difference between the reference and irradiation (excitation) arms and causes thus a phase change between these arms.

A complete sketch of our QO bridge, involving all these components except lenses, is shown in Fig. 3.3 on page 34 and it will be described in detail in the following Chapter 3.

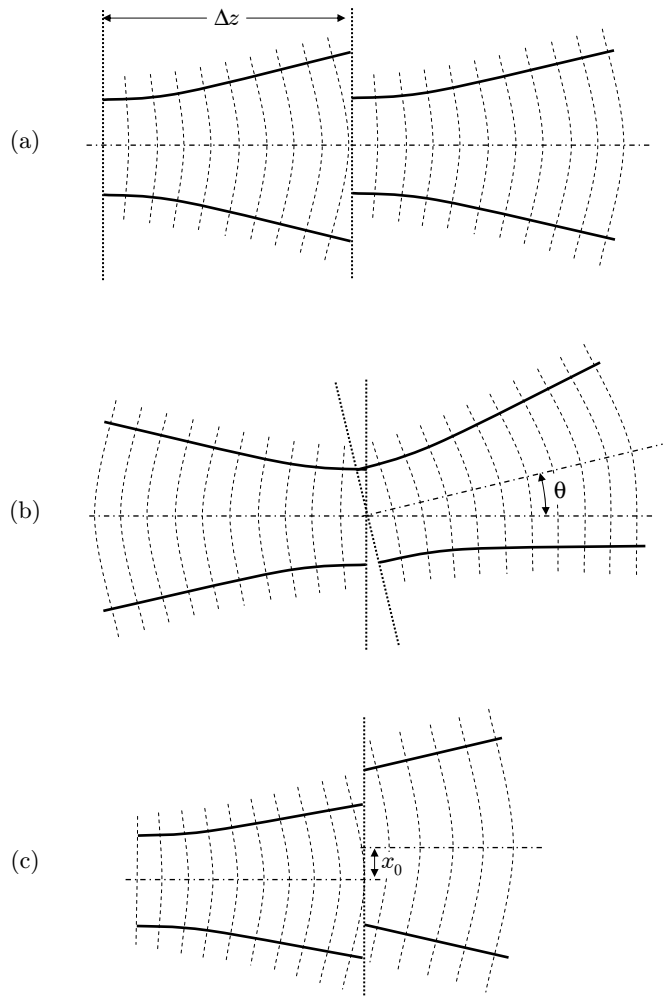


Figure 2.5: Three general cases of Gaussian beam misalignment, where the dotted lines mark reference planes. (a) Axially aligned beams with offset waists $\Delta z$, (b) tilted beams by an angle $\theta$, (c) radially offset beams of $x_0$.

### 2.2.1 Beam Coupling

Any misalignment of QO components causes power losses of the propagated beam. It can introduce higher order modes in the system which take energy from the more favourable fundamental mode. Thus the proper beam coupling of QO components is important for the performance of the whole QO system.

The power transfer is a function of the system parameters and is described by mode coupling and mode conversion coefficients [63]. We can simply define the coupling efficiency as the ratio of the power measured by the detector to the power emitted from the source. If the ratio is equal to 1, then alignment of QO components is perfect (loss-free coupling). In order to perfectly couple QO components the Gaussian beams generated by the components should be identical.

The three simplest misalignment cases are depicted in Fig. 2.5: (a) axially aligned beams with an offset $\Delta z$ in their waists, (b) tilted beams by an angle $\theta$ and (c) beams with radial offset $x_0$.

In HF-EPR, special attention has to be paid to tilted beams (Fig. 2.5b). The MW power loss caused by even a very small misalignment ($\sim 0.1°$) can be significant. On the other hand, the QO bridge is relatively robust with respect to lateral as well as to longitudinal misalignments, so that an alignment with a precision of the order of tenths of a millimetre is easy to obtain.

Whereas in our case the QO components are perfectly aligned and fixed on the movable QO bridge, the QO bridge and the corrugated waveguide used to propagate the light in the cryostat are mechanically independent. Thus one has to pay special attention to the proper coupling of the QO bridge with the corrugated waveguide, which means in practice that the QO bridge has to be from time to time realigned with respect to the corrugated waveguide.

The detailed description about the coupling can be found in Refs. [53, 63]. A quantitative analysis of the beam coupling of an EPR QO system which works at 360 GHz can be found in the thesis of M. Fuchs [48].

## 2.3 Fabry - Pérot Interferometer (Resonator)

The Fabry - Pérot (FP) interferometer (often called resonator) is a frequency selective component which has numerous applications. In optics, FP resonators can be used as frequency selective filters; they are also essential parts in the construction of optical lasers etc. In HF-EPR, the FP resonators can replace single mode cavities, which are rather difficult to build for high frequencies (above 200 GHz) due to their small sizes (less than 2 mm).

The general scheme of a FP resonator is shown in Fig. 2.6. The FP resonator consists of two mirrors. The two mirrors, with radii of curvature $R_1$ and $R_2$ with apertures $a_1$ and $a_2$, respectively, are separated by a distance $L$. The FP resonator geometry can be described by two **g-parameters**, $g_1$ and $g_2$, sometimes called **resonator confocal parameters** and defined as:

$$g_1 = 1 - \frac{L}{R_1} \qquad \text{and} \qquad g_2 = 1 - \frac{L}{R_2} \tag{2.13}$$

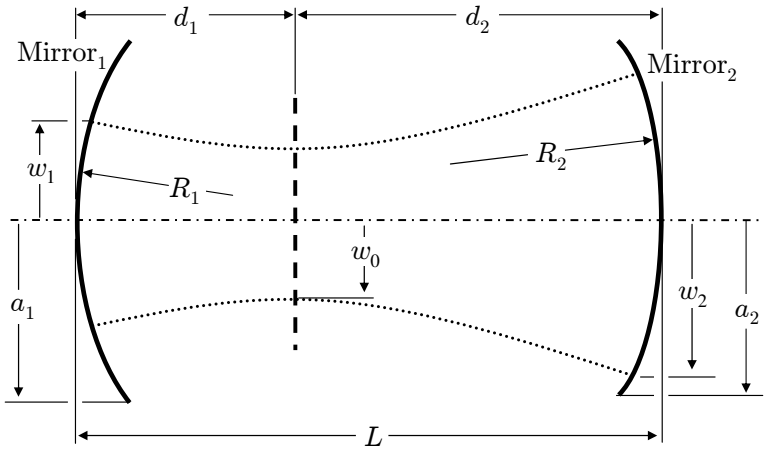


Figure 2.6: General non-symmetric configuration of the Fabry - Pérot resonator and the Gaussian beam that propagates in it. The two mirrors, with radii of curvature $R_1$ and $R_2$ with apertures $a_1$ and $a_2$, respectively, are separated by a distance $L$. The Gaussian beam has the beam waist $w_0$ shifted from Mirror$_1$ by a value $d_1$. The beam radius has a value $w_1$ on Mirror$_1$ and a value $w_2$ on Mirror$_2$.

in which only the distance between the mirrors and their curvatures appear. The apertures of the mirrors are hidden in the Fresnel number $N$:

$$N = \frac{a_2 a_1}{\lambda L} \tag{2.14}$$

and in $G_1$ and $G_2$, named stability factors:

$$G_1 = g_1 \frac{a_1}{a_2} \qquad \text{and} \qquad G_2 = g_2 \frac{a_2}{a_1}. \tag{2.15}$$

The resonance frequency depends on the geometrical configuration only (g-parameters), whereas the optical losses depend on the geometry as well as on the mirror sizes (Fresnel number $N$). The geometrical configuration of FP resonators will be discussed later.

In a FP resonator the resonance occurs when the phase shift of the total round-trip is a multiple of $2\pi$. In our case (cylindrical coordinates), the resonance is found for:

$$2\pi q = 2\left[\frac{2\pi L}{\lambda} - (2p + m + 1)\arccos\sqrt{g_1 g_2}\right], \tag{2.16}$$

where $p, m$ and $q$ are positive integers; $q$ is the **axial mode number** whereas $p$ and $m$ are **transverse mode numbers**. This can be rewritten into the equation for the resonance frequencies:

$$f_{res} = \left[q + \frac{1}{\pi}(2p + m + 1)\arccos\sqrt{g_1 g_2}\right]\frac{c}{2L}. \tag{2.17}$$

The last term $c/2L$, where $c$ is the speed of light, is the frequency of the fundamental mode in the FP resonator. The higher order modes are shifted from the fundamental mode by a value that depends on the resonator geometry (g-parameters) and on the mode order; this shift goes towards lower frequencies (higher wavelengths).

### 2.3.1 Finesse $F$

When dealing with FP resonators, the figure of merit is the finesse $F$ and not the quality factor $Q$. However, these quantities are related by $Q = qF$. Thus $Q$ can reach very high (and meaningless) numbers depending on the resonator mode $q$.

The theoretical value of the finesse $F$, for the lossless case, depends only on the reflection coefficients $r_1$ and $r_2$ of the mirrors [52]

$$F = \frac{\pi\sqrt{r_1 r_2}}{1 - r_1 r_2}. \tag{2.18}$$

Using the approximate formula for $r$ [53]:

$$r = \sqrt{1 - 1.67 \times 10^{-5}\sqrt{(f\rho)}} \tag{2.19}$$

the theoretical finesse at $f$=300 GHz for gold coated mirrors ($\rho$=2.2) is found to be $F \approx$1800. However, in practice, the finesse $F$ strongly depends on the tuning precision as well as on the quality of the mirrors (surface, metal coating). Thus any imperfection in mirrors and in tuning leads to an actual finesse well below the theoretical value.

Experimentally, the finesse $F$ is determined by

$$F \approx \frac{\text{free spectral range (A)}}{\text{FWHM of resonance peak (B)}}. \tag{2.20}$$

where the free spectral range A is the distance between successive resonances and B is the Full Width at Half of Maximum (FWHM) of a resonance peak. Thus FP resonators with a high finesse $F$ show sharper resonance peaks, see Figs. 3.6 and 4.8.

The life time of the photon in the FP resonator is given by:

$$\tau_c \approx \frac{\mathrm{Q}}{2\pi f}. \tag{2.21}$$

The life time of a 300 GHz photon in a FP resonator with finesse 200 and $5^{th}$ mode is then $\tau_c \sim 0.5$ ns. This means that the cavity ringing is almost undetectable in pulsed HF-EPR systems, which allows implementing cavities with very high $Q$. However excitation bandwidth of such a cavity is then narrow.

### 2.3.2 Resonator Stability

FP resonators can be divided into stable or unstable resonators. Stable resonators are the ones fulfilling the condition:

$$0 < G_1 G_2 < 1 \tag{2.22}$$

This condition means that, for a stable FP resonator, a bundle of light is periodically refocused by mirrors as it travels back and forth between them, for an unstable resonator it is getting dispersed more and more.

From the above condition, we can draw a stability diagram (Fig. 2.7). Every point in the diagram represents a FP resonator geometry. In the following, we will discuss the main geometries.

#### Confocal and Half-Confocal Resonators

The confocal resonator ($R_1 = R_2 = L$) is represented by the middle point ($g_1 = g_2 = 0$) of the stability diagram (Fig. 2.7). Such a resonator is very close to be unstable. To prevent instability, the mirror spacing $L$ should be slightly larger or smaller than the

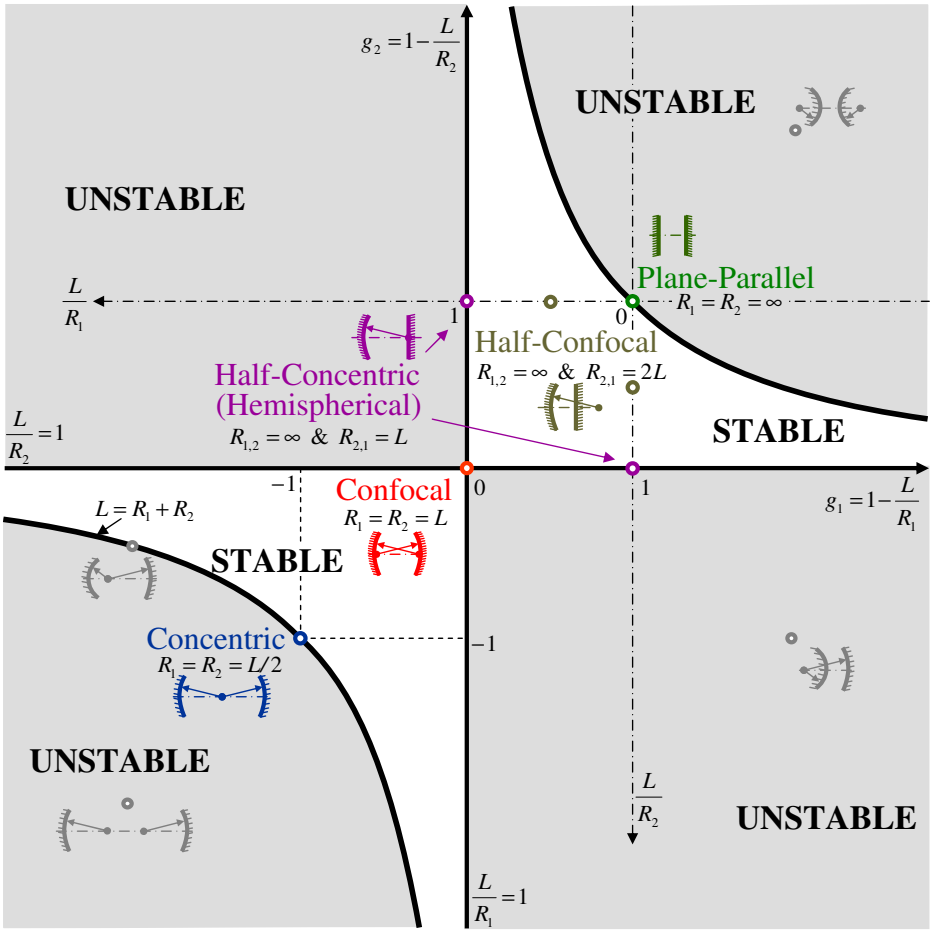


Figure 2.7: The stability diagram, where each point represents a FP resonator geometry. Unstable FP resonators lie in the gray part while stable FP resonators lie in the white part of the diagram.

exact confocal distance. The characteristics of the resulting "near-confocal" resonator are almost the same as the characteristics of an ideal confocal resonator.

The confocal FP resonator is characterized by the lowest diffraction losses of all resonator geometries. The energy stored in the fundamental mode is more concentrated near the optical axis. The confocal geometry, compared to other systems, is less sensitive to angular misalignment.

The half-confocal (or semi-confocal) resonator, based on one curved mirror ($R_1 = 2L$) and the other flat ($R_2 = \infty$), has properties equivalent to the ideal confocal resonator avoiding the stability problems.

### Plane-Parallel and Concentric Resonators

As given by the symmetry of the stability diagram (Fig. 2.7), the plane-parallel resonator ($R_1 = R_2 = \infty$) and the concentric resonator ($R_1 = R_2 = 2L$) can be treated as equivalent systems having the same characteristics [58, 59, 60].

These resonators are characterized by relatively high diffraction losses and difficult

alignments. Alignments within seconds of arc are necessary. The fundamental mode in the resonator occupies a larger volume than in the comparable confocal resonator. Thus, the beam radius $w$ of the fundamental mode is bigger and the irradiation energy is spread over a larger volume.

The half-concentric (or "hemispherical") resonator ($R_1 = \infty$, $R_2 = L$) has the same characteristics as the concentric resonator if the flat mirror is large enough. The half-concentric configuration is much easier to align with respect to plane-parallel configuration. The alignment difficulties are comparable to the confocal resonator. Here, it is of course also better to slightly shift the resonator from the boundary to prevent instability.

## 2.4 Conclusion

In this chapter an overview of QO and its applications to HF-EPR spectrometers has been given. We describe the Gaussian beam propagation of the MW and how QO can be used in HF-EPR. The propagation of the MW through the corrugated guide (taper) was quantitatively described. This chapter has also introduced the theory of FP resonators which is based on the Gaussian beam propagation. This theory will be further used in Chapters 3 and 4 devoted to the HF-EPR spectrometer and the FP resonator design, respectively.

The Gaussian beams play an important role not only in millimetre and submillimetre wavelength QO systems, but in laser optics as well. Therefore, almost every text dealing with optical systems discusses Gaussian beam propagation in detail. This short introduction was mostly inspired by a book from P. F. Goldsmith [53] where QO is described in detail and by the work of G. M. Smith *et al.* [13]. The theory of the FP resonator was based on works of H. Kogelnik *et al.* and G. D. Boyd *et al.* [58, 59, 60].

# Résumé Chapitre 3

## Spectromètre RPE-HF

Dans ce chapitre, le spectromètre de RPE-HF du LNCMI est décrit de façon générale, en insistant plus particulièrement les modifications apportées afin de permettre un fonctionnement en mode impulsionnel (Fig. 3.1).

**Sources Microondes:** Jusqu'à présent, le spectromètre RPE-HF a été conçu pour permettre une approche multifréquence et le spectromètre fonctionne en configuration homodyne. Pour ce faire, deux diodes à effet Gunn avec régulation de phase sont disponibles ainsi que leurs multiplicateurs respectifs (Radiometer Physics GmbH).

Par contre, le développement d'un spectromètre impulsionnel a été réalisé pour une fréquence unique, 283.2 GHz, et implique aussi un fonctionnement superhétérodyne (Fig. 3.1). Cette fréquence de 283.2 GHz est fournie par un résonateur à oscillateur diélectrique avec multiplication active (DRO) fournissant une fréquence de 94.4 GHz.

**Propagation des Microondes:** Le spectromètre RPE (Fig. 3.3) combine des composants QO et un guide d'onde cannelé surdimensionné. Le guide d'onde sert à la propagation dans le cryostat et est couplé au pont QO placé au-dessus de l'aimant. Le système QO, optimisé pour une fréquence $f = 257.5\,\mathrm{GHz}$ ($\lambda = 1.17\,\mathrm{mm}$), a été conçu et fabriqué par Thomas Keating Ltd. Il est décrit dans la Réf. [64].

Le spectromètre RPE fonctionnen mode induction qui repose sur la rotation de la polarisation (de la lumière excitatrice) lors de la résonance. Cela résulte de l'absorption d'une seule composante circulaire de la polarisation linéaire ($\Delta$M=+1 par exemple), comme illustré dans l'encart de la Fig. 3.3.

**Porte-Echantillons (Cavités):** Jusqu'à présent, le spectromètre RPE-HF n'utilisait que des cavités non résonantes [64]. Dans le cas du fonctionnement QO du spectromètre, cela correspond à un double passage des ondes MW à travers l'échantillon.

Au cours de ce travail, nous avons conçu et utilisé deux types de porte-échantillons: un résonateur FP et un support tournant de type non-résonant (Fig. 3.5). Le support tournant permet d'étendre l'utilisation de la RPE multi-fréquence aux études de monocristaux orientés. Le résonateur FP a été conçu essentiellement pour la construction d'un spectromètre RPE pulsé fonctionnant à 283.2 GHz. Cependant, il peut aussi être utilisé pour d'autres fréquences. Les trois porte-échantillons sont représentés schématiquement dans la Fig. 3.5.

**Détection du Signal RPE:** Pour la détection on utilise soit un bolomètre InSb à électrons chauds (QMC Instruments Ltd) soit une détection hétérodyne (Radiometer Physics GmbH). Alors que le bolomètre couvre une très grande plage de fréquences et sert pour la RPE multi-fréquence, la détection hétérodyne rapide n'est adaptée qu'à une seule fréquence, 283.2 GHz, et a été mise au point durant ce travail (Fig. 3.1).

**Aimant et Cryostat:** L'échantillon est placé au centre de l'aimant supraconducteur (Cryogenics Ltd.) avec un champ maximum de 12 T. L'aimant est équipé d'un cryostat à température variable (VTI) qui permet de mesurer de 1.5 K jusqu'à la température ambiante.

**Contrôle de l'expérience et Acquisition de Données:** Au cours de ce travail, un programme LabView a été écrit pour le contrôle du spectromètre RPE-HF et l'acquisition de données. Il permet un contrôle aisé et pratique de l'électronique du spectromètre RPE pour les expériences en onde continue.

**Sensibilité du Spectromètre RPE-HF:** La sensibilité absolue mesurée pour le spectrometer RPE fonctionnant en mode continu et en configuration superhétérodyne est de $3 \times 10^8$ spins/G/s à température ambiante. Cette valeur a été déterminée pour un film du radical BDPA comme échantillon de référence. Le résonateur FP fonctionnait alors avec un réseau de 75 lignes/inch, lignes de 200 $\mu$m de large; le miroir sphérique a un rayon de courbure de 50 mm. Cette configuration correspond à une Finesse $F \sim 400$.

**Conclusion:** Ce chapitre décrit le spectromètre RPE-HF avec toutes ses spécifications. La description du résonateur FP est présentée au Chapitre 4. Le spectromètre décrit ci-dessus ainsi que les porte-échantillons (le résonateur FP et le support tournant) ont été utilisés pour obtenir les résultats expérimentaux de cette thèse (Chapitres 5 et 6). Alors que la mise au point de la détection superhétérodyne, nécessaire pour le fonctionnement en mode pulsé, a réussi, les problèmes avec la source de fréquence à 283.2 GHz et la destruction de la diode à effet Gunn ont nécessité le changement complet de la source de fréquence. Les délais induits par la fabrication de la nouvelle source à 283.2 GHz et son adaptation au montage n'ont pas permis de réaliser d'expérience d'écho de spin avant la soumission de ce manuscrit.

# Chapter 3

# HF-EPR Spectrometer

EPR spectroscopy has been the object of many technical changes and improvements within the last decades. The improvements went hand in hand with developments in different fields of physics, e.g. physics of semiconductors (detectors and sources of MWs), physics of superconducting materials (magnets), astronomy (QO propagation) etc. Thanks to these developments, the EPR spectrometers could move to higher frequencies and pulsed operation could also be implemented. The developement of high frequency and HF-EPR spectrometers allowed resolving many phenomena difficult or even impossible to observe before. Especially, it allowed determining small $g$ differences and accessing integer spin systems with large ZFSs (which were so-called "EPR silent" before).

In this chapter, a general overview of the HF-EPR spectrometer at GHMFL will be given, focusing on our attempt to extend the existing continuous HF-EPR spectrometer into a pulsed regime (Fig. 3.1).

## 3.1 Microwave Sources

Up to now, the HF-EPR spectrometer has been developed to take advantage of the multi-frequency approach and the spectrometer is operated in homodyne configuration. For that purpose, two phase-locked Gunn diodes and associated sets of multipliers have been used as frequency sources (Table 3.1, Radiometer Physics GmbH). The block scheme of the phase-locked Gunn diode sources is shown in Fig. 3.2. The phase-lock is obtained from a phase-lock loop (PLL) module which maintains the Gunn diode frequency stable by correcting its bias $V_{DC}$. To achieve the phase-locking, a synthesizer and two very stable quartz oscillators with frequencies of 100 MHz and 10 MHz respectively are used to drive the PLL module. Multipliers inserted after the phase-locked Gunn diode allow obtaining multiples of the Gunn diode frequency $f_{GD}$ (Table 3.1). As the multiplication is not perfectly efficient, the output MW power decreases with the rate of the multiplication. Typically, the output power goes from $\sim 40$ mW for the base frequency of the Gunn diode $f_{GD}$ to one order of magnitude lower for the tripled frequency.

Conversely, the development of a pulsed spectrometer was performed for a unique frequency, at 283.2 GHz, and relied on superheterodyne operation (Figs. 3.1 and 3.10). This frequency is supplied by an actively multiplied dielectric resonator oscillator (DRO) delivering a frequency of 94.4 GHz. The progress in active multipliers results in sources which can reach much higher powers (with respect to the $\sim 40$ mW of our phase-locked

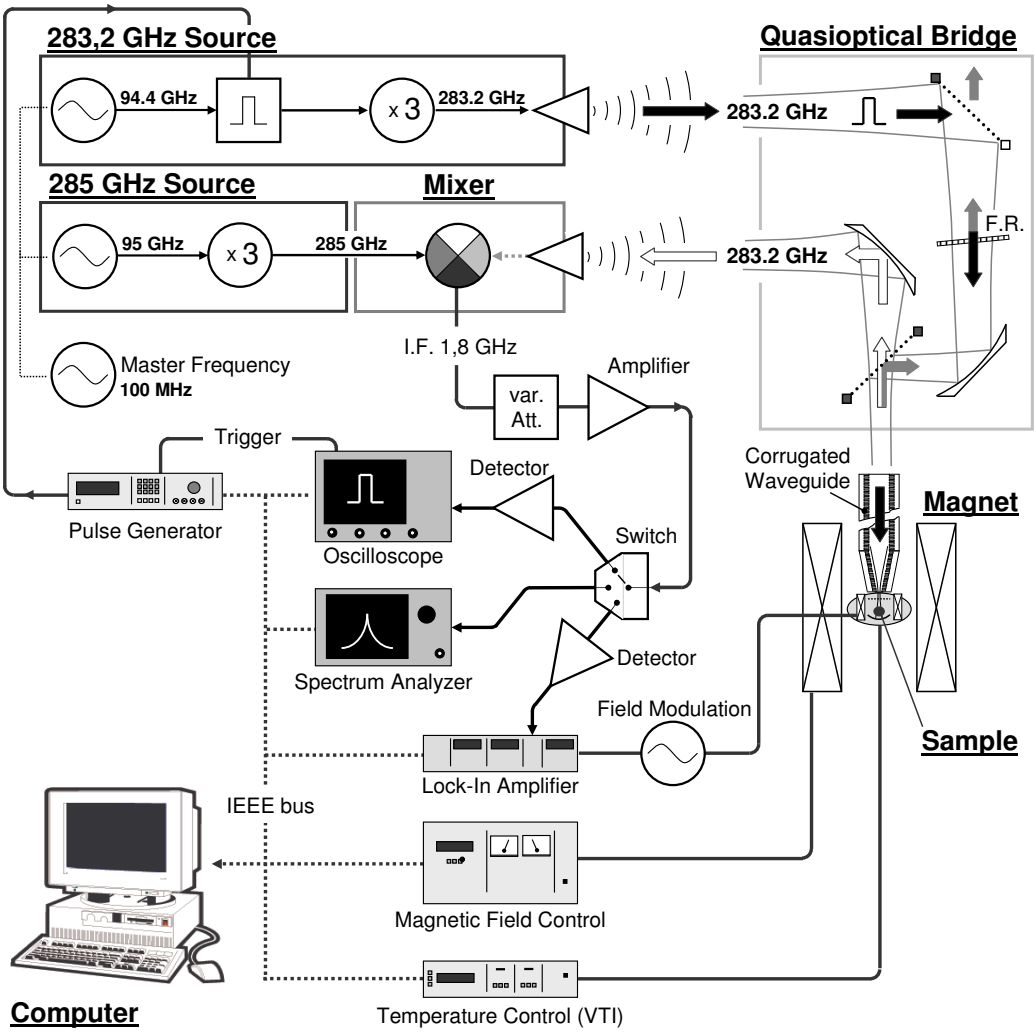


Figure 3.1: Scheme of the HF-EPR spectrometer operating at 283.2 GHz. The spectrometer uses a superheterodyne detection (Radiometer Physics GmbH, Fig. 3.10) based on a mixing of the excitation frequency $f_{ex}$=283.2 GHz with a local oscillator frequency $f_{LO}$=285 GHz in a harmonic mixer. The product of the mixing is an intermediate frequency $f_{IF}$=1.8 GHz which is then further proceeded and directed by a switch (ACC Inc.) controlled by a computer either to an oscilloscope (LeCroy WaveRunner 500 MHz) for pulsed EPR, to a spectrum analyzer (Rohde & Schwartz FSP13) for the tuning of the FP resonator or to a lock-in amplifier (Stanford SR830) in case of cw-EPR. For the propagation of MWs a QO bridge (Fig. 3.3) with conjunction of corrugated waveguide (Fig. 3.4)(both Thomas Keating Ltd.) is used. A sample is placed either in the FP resonator to enhance the 283.2 GHz $B_1$ field at the sample, in a rotating holder (orientation study of crystals) or in a non-resonant cavity, see Fig. 3.5. The MW excitation pulses (283.2 GHz) are performed at 94.4 GHz by a PIN switch (Elva-1) which are then frequency tripled to 283.2 GHz. To drive the PIN switch a pulse generator (Agilent 81110A Pulse-/Pattern Generator 165 MHz) is used. For a cw-EPR experiment the PIN switch is kept open. The whole experiment is controlled by a computer.

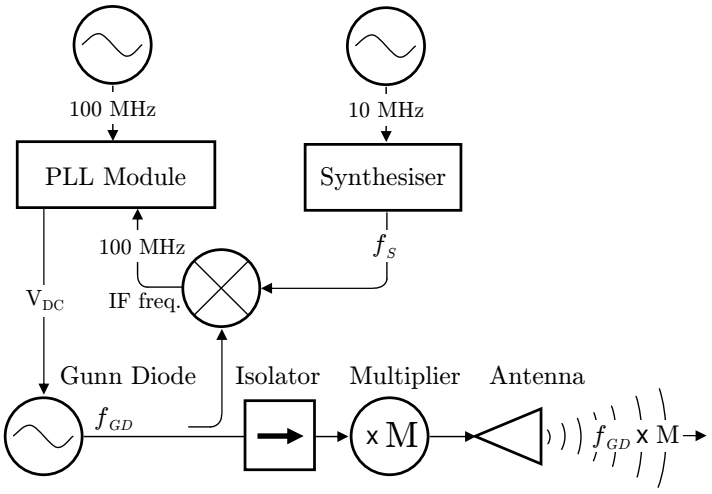


Figure 3.2: Block scheme of the MW source based on the phase-locked Gunn diode of a frequency $f_{GD}$. The phase-lock loop (PLL) module maintains the Gunn diode frequency stable by correcting its bias $V_{DC}$. Using multipliers a multiple of $f_{GD}$ can be achieved, Table 3.1.

Gunn diode). The source consists of a 7.8655 GHz DRO (synthesiser) which is stabilized by a 100 MHz quartz oscillator (master frequency). The 7.8655 GHz frequency is first doubled by a (passive) doubler and then further multiplied by a factor of 6 by an active multiplier to get 94.4 GHz. A final frequency tripler allows the 283.2 GHz exciting frequency to be obtained. For pulsed operation, an isolator followed by a fast PIN switch (ELVA-1) is inserted before the frequency tripler.

In a previous stage, the 283.2 GHz frequency was supplied by a phase-locked Gunn diode with a base frequency of 141.6 GHz followed by a doubler (Fig. 3.9). The failure of the emitting semiconductor element led to the replacement of the Gunn diode source (141.6 GHz) by a more powerful multiplied DRO source (94.4 GHz), resulting also in the change of the detection scheme as illustrated in Figs. 3.9 and 3.10. With the DRO source, the output power at 283.2 GHz is $\sim 10$ mW with respect to $\sim 1$ mW with the Gunn diode (in both cases the values are with isolators and PIN switches included).

## 3.2 Microwave Propagation

The EPR spectrometer (Fig. 3.3) combines QO components and an oversized corrugated waveguide. The waveguide is used for the MW propagation in the cryostat and is coupled to the QO bridge placed above the magnet. The QO system, optimized for a frequency of $f = 257.5$ GHz ($\lambda = 1.17$ mm), was designed and produced by Thomas Keating Ltd. It is described in Ref. [64]. The corrugated waveguide and the QO bridge are discussed in the following text.

### 3.2.1 Quasioptical Bridge

The QO bridge (optical table), as shown in Fig. 3.3, is made of series of QO components: elliptical mirrors, wire polarizers, absorbers, Faraday rotator etc.

The Gaussian beam propagates on the optical table (Fig. 3.3), composed of an UPPER and a LOWER part. The source of the millimetre wavelength radiation is located on the UPPER part together with a detector and most of the QO components. The remaining components are located in the LOWER part of the table. The UPPER and LOWER

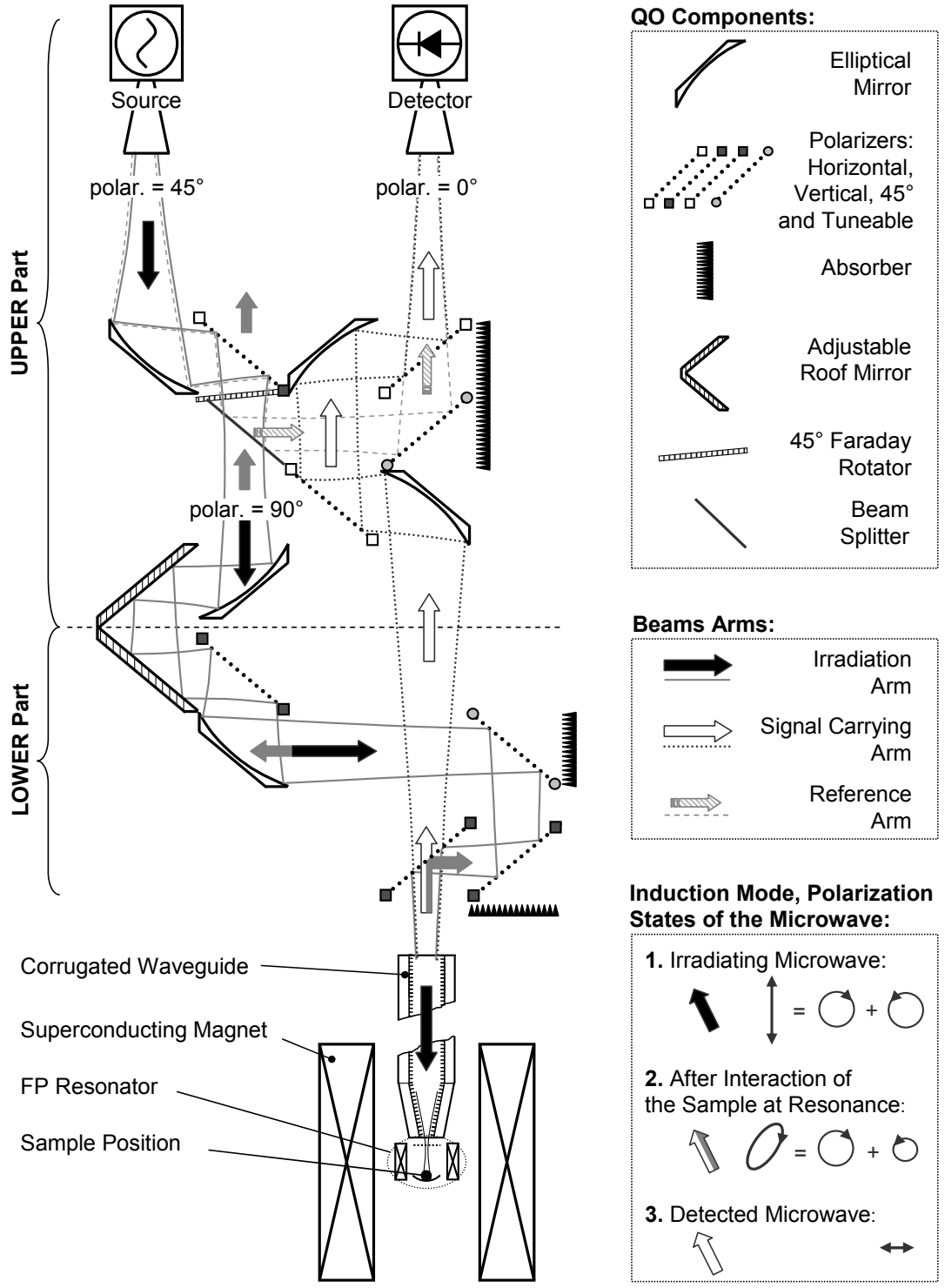


Figure 3.3: Schema of the QO bridge (Thomas Keating Ltd.) of the HF-EPR spectrometer at GHMFL. The Gaussian beam propagates between off-axial QO components on the optical table which are optimized for $f = 257.5\,\mathrm{GHz}$. The table consists of UPPER and LOWER parts. The propagation of the MW over the bridge is shown as well as the induction mode is explained in the figure inset. Note: For the simplicity of the figure the position of the QO components do not correspond to reality. In practice the refocusing (elliptical) mirrors are equidistantly spaced.

Table 3.1: List of MW sources used at GHMFL for multi - frequency and pulsed HF-EPR experiments (in bold). All sources, except the 94.4 GHz source (actively multiplied DRO) are based on a phase-locked Gunn diode (Fig. 3.2).

| **MW Source** | **Frequency $f$ (GHz)** | **Wavelength $\lambda$ (mm)** | **Magnetic Field $B_{g_e=2}$ (T)** | **Note** |
|---|---|---|---|---|
| 95 GHz | 95 | 3.158 | 3.394 | - |
| | 190 | 1.579 | 6.788 | doubler |
| | 285* | 1.053 | 10.181 | tripler |
| | 380 | 0.789 | 13.575 | doubler of 190 GHz |
| | 475 | 0.632 | 16.969 | quintupler |
| 115 GHz | 115 | 2.609 | 4.108 | - |
| | 230 | 1.304 | 8.216 | doubler |
| | 345 | 0.870 | 12.3251 | tripler |
| | 460 | 0.652 | 16.433 | quadrupler |
| **141.6 GHz*** | 141.6 | 2.119 | 5.059 | - |
| | 283.2 | 1.059 | 10.117 | doubler |
| **94.4 GHz** | 94.4 | 3.178 | 3.372 | - |
| | 283.2 | 1.059 | 10.117 | tripler |

* The 141.6 GHz Gunn diode planned as a source for pulsed-EPR experiments was irreparable damaged and is no more available. The source was replaced by a 94.4 GHz source (actively multiplied 7.8655 GHz DRO source).

parts of the table are bridged by a movable roof mirror (two flat mirrors) Fig. 3.3. Moving the roof mirror allows us to adjust the phase between the reference and the irradiation arms when a homodyne configuration is used. The QO components used in the bridge are arranged in an off-axial manner. Standing waves between the components are then strongly suppressed. The optical table is placed on a rigid aluminium frame and adjusted with respect to the coupling window of the corrugated waveguide. The optical table is on rails and can be moved and fixed in work position above the magnet. In this way, a proper focusing of the Gaussian beam into the corrugated waveguide and a safe insertion of the probe (corrugated waveguide) into the cryostat is easily achieved.

The EPR spectrometer works in the induction mode, which was used for the first time in EPR by A. M. Portis and D. Teaney [65] and in HF-EPR utilizing QO by G. M. Smith *et al.* [13]. The induction mode is based on the rotation of polarisation (of the exciting MW) at the resonance. It corresponds to the absorption of only one circular component of the linear polarisation ($\Delta$M=+1 for instance), see inset in Fig. 3.3.

The induction mode increases significantly the sensitivity of the EPR spectrometer because the MW radiation (copolar) which did not interact with the sample, is reflected back and is filtered out (gray arrow in Fig. 3.3). In this way, the noise floor on the detector is strongly reduced of factor 30 dB and more). The filtering is achieved by a polarizer which separates (isolates) the large backward reflected MW from the fractional part of the crosspolar MW carrying the signal. The resulting MW isolation on the polarizer is over 40 dB. In our case (Fig. 3.3), the last polarizer (LOWER part), before the MW propagate into the corrugated waveguide, is responsible for the induction mode operation. The MW reflected backwards from the resonator goes through the polarizer to the detector

(UPPER part) only if the MW has changed its polarisation to the orthogonal crosspolar polarisation.

### 3.2.2 Oversized (Corrugated) Waveguides

The corrugated waveguide is an oversized waveguide with a corrugation instead of a smooth surface inside the guide (Fig. 2.2). The corrugation has a groove depth of $d = \lambda/4$ and a typical period of $p < \lambda/3$ with $\lambda = 1.17\,\text{mm}$ (257.5 GHz). If the used wavelength is such that $\lambda = 4d$, the MW propagates with negligible losses (balanced condition). In this situation, the reactance of the waveguide walls tends to infinity, there no MW losses [53]. Out of the balance condition, lower MW losses are achieved than in a corresponding smooth waveguide if the corrugation depth $d$ is in the range of $0.35\lambda/4 - 1.75\lambda/4$ [13]. The MW losses in the oversized corrugated waveguide are also proportional to the ratio $\lambda^2/a^3$, where $2a$ is the inner diameter of the waveguide, which means that the MW losses become even lower for higher frequencies.

In the circular corrugated waveguide, a hybrid $HE_{11}$ mode is propagated, which is approximately a superposition of $TM_{11}$ and $TE_{11}$ modes that propagate at the same rate. Very good polarisation properties are obtained in circular corrugated waveguides, if the $2a$ diameter is sufficiently large and $d \approx \lambda/4$. The $HE_{11}$ polarisation can be then propagated with extremely good purity[1]. The two orthogonal polarisations (crosspolar and copolar) have thus the same propagation conditions [13, 16], which is very important for the induction mode already discussed. All these properties make circular corrugated waveguides very well suited for the propagation in the cryostat. Nowadays, corrugated waveguides are used in all modern HF-EPR systems [13, 26, 27, 49, 50, 54, 55, 66].

A probe, the corrugated waveguide and the taper optimized for 257.5 GHz ($\lambda = 1.17\,\text{mm}$) together with the FP resonator, is shown in Fig. 3.4. The corrugated waveguide has a 18 mm inner diameter. The total length of the probe is 1.3 m, see Fig. 3.4. On top of the probe, a high density polyethylene (HDPE) window (n=1.525 at 300 GHz [67]) of 1 mm thickness is used. The MW losses in the corrugated waveguide are well below 1 dB/m for our MW sources (Table 3.1).

## 3.3 Sample Holders (Cavities)

Up to now, the HF-EPR spectrometer was only operated with non-resonant cavities [64]. For the QO configuration of the spectrometer, it corresponds to a MW double pass through the sample.

During this work, we designed and used two types of sample holders: a Fabry - Pérot resonator and a non-resonant type rotating holder (Fig. 3.5). The rotating holder extends the multi-frequency operation to orientation studies on single crystals. The Fabry - Pérot resonator was mainly designed for the development of a pulsed EPR spectrometer operating on the frequency 283.2 GHz. Nevertheless, it can also be employed at other frequencies. The three holders are separately discussed in the following paragraphs.

**Non-resonant (double pass) cavity:** It consists of a smooth tube made of German silver (6 mm inner diameter) with a brass mirror (plug) at the bottom (Fig. 3.5a). The brass

[1] low polarisation rotation with respect to smooth waveguides and low scattering to higher order modes

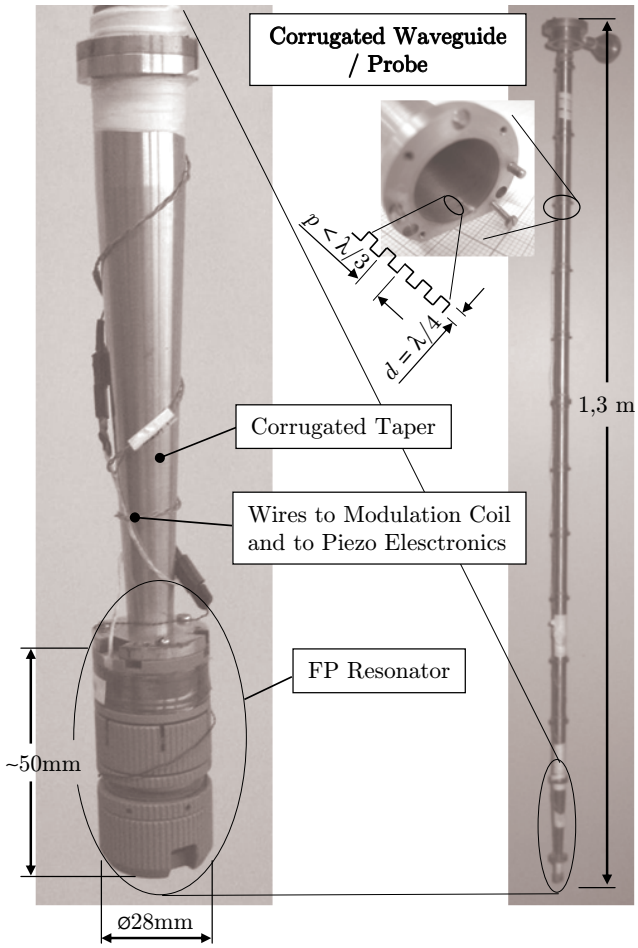


Figure 3.4: Photograph of the corrugated waveguide and taper with attached FP resonator (probe). The probe is inserted into the cryostat. The MWs are focused into the probe by HDPE window in the flange on top of the probe. The cross-section of the conical corrugated taper and the FP resonator can be seen in Fig. 2.2 and in Fig. 4.4, respectively.

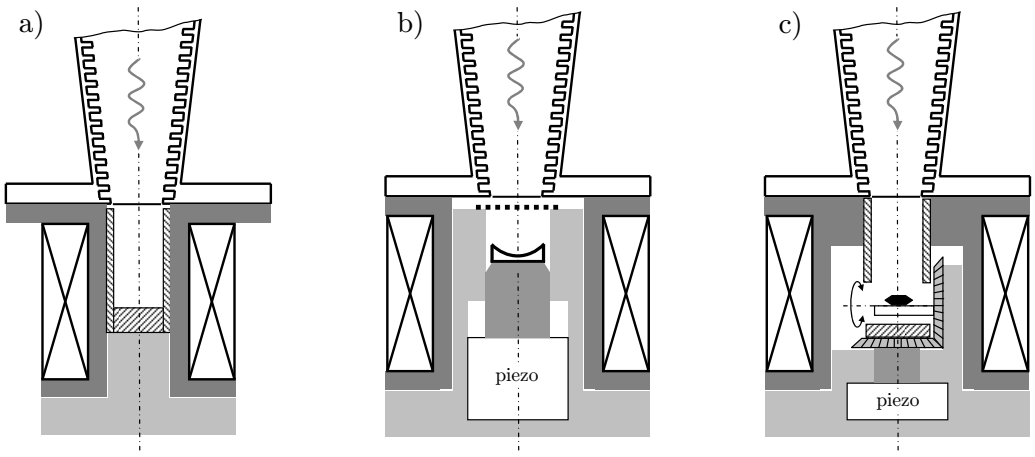


Figure 3.5: Schemas of commonly used sample holders attached to the corrugated waveguide a) double pass cavity (non-resonant cavity) is a simple metallic cap (dashed area) which can be filled by liquid samples. b) Fabry - Pérot resonator with the housing supporting the partially reflective mirror (dashed line). The piezoelectric nanopositioner moves the bottom spherical mirror allowing the tuning of the resonator (Fig. 4.4). c) rotating holder showing the gears and the piezoelectric rotator. The sample (black point) is placed on a Teflon support. The modulation coils are represented by the crossed area. The loading of a sample in all three cases is simple and is made from the bottom of the probe.

mirror is gold plated. The cavity is surrounded by a modulation coil wound on an epoxy structure to maximise the modulation field penetration. A (maximal) modulation field of 50 Gauss at 1 kHz is obtained for a 65 mA current.

Teflon cups are used for liquid samples or free powders whereas pellets (pressed powder in order to avoid orientation effects) are directly placed on the mirror.

**Fabry - Pérot Resonator:** In the FP resonator, multiple reflections through the sample and thus long appreciable MW absorption (photon life time in the cavity) is achieved. The FP resonator is designed in the half-symmetric configuration, i.e. with one flat semitransparent and one curved spherical mirror. The MW is coupled into the FP resonator via the semitransparent mirror, a squared metallic mesh. This mesh is obtained by deposition of gold on a cover slip by UV-lithography (for details see Appendix C). Among the meshes prepared by UV-lithography (Table 4.4), the one with a pattern of 75 lines/inch (200 $\mu$m) is mostly used. For the bottom mirror, we use commercially available concave spherical mirrors from Edmund Optics or Thorlabs (Table 4.3). Among the spherical mirrors available, mirrors with 25 and 50 mm radii of curvature are mainly used. The tuning of the FP resonator is performed by moving the bottom mirror via a piezoelectric nanopositioner ANPz50 (Attocube systems AG) which enables a displacement of 2.5 mm with a precision of tenths of a nanometre. For cw-EPR operations, the FP resonator is surrounded by a modulation coil directly wound onto the Torlon housing. The modulation coil has a maximum field amplitude of about 10 G at frequencies below 1 kHz.

The sample has to be located at the maximum of the magnetic field component $B_1$ of the excitation MW (node of $E_1$ field). In principle, there are three choices: either the sample is placed on one of the mirrors, or it is localized at one of the $B_1$ maxima between the FP resonator mirrors. Placing the sample on the mesh could appear optimal,

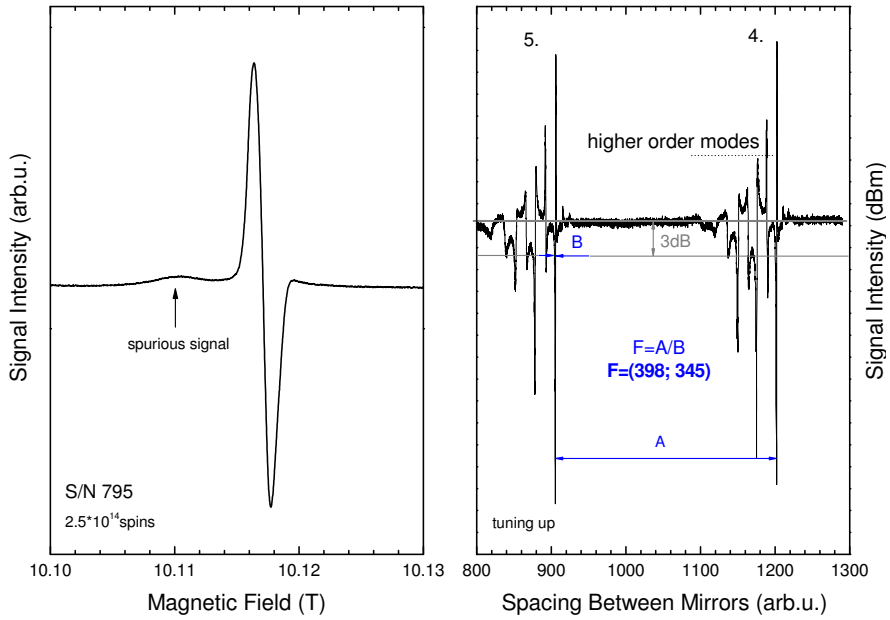


Figure 3.6: Left: EPR spectrum of a thin film of BDPA, containing $2 \times 10^{14}$ spins, recorded with the Fabry-Pérot resonator at 283.2 GHz (250 K), with a modulation amplitude of 0.9 G. The spectrometer was operated in heterodyne configuration with 141.6 GHz Gunn diode (Fig. 3.9). The S/N is higher than 795. Right: resonance fringes for this measurement ($F_{exp}$=400).

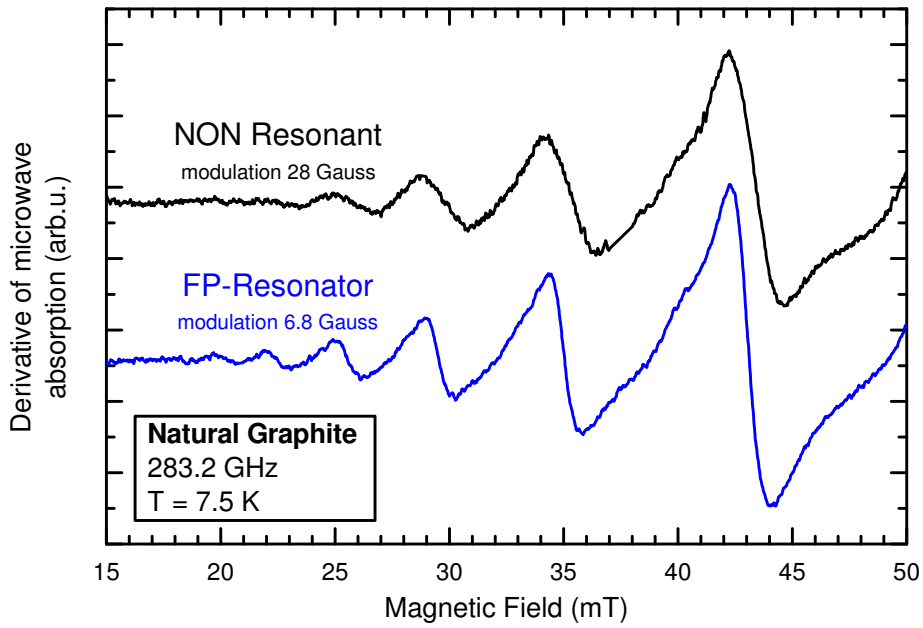


Figure 3.7: Single crystal cyclotron resonance of natural graphite at 283.2 GHz and 7.5 K for the magnetic field applied perpendicular to the carbon sheets. Upper spectrum recorded with the QO transmission set-up (modulation amplitude: 28 G); lower spectrum recorded with the Fabry-Pérot resonator (modulation amplitude: 6.8 G).

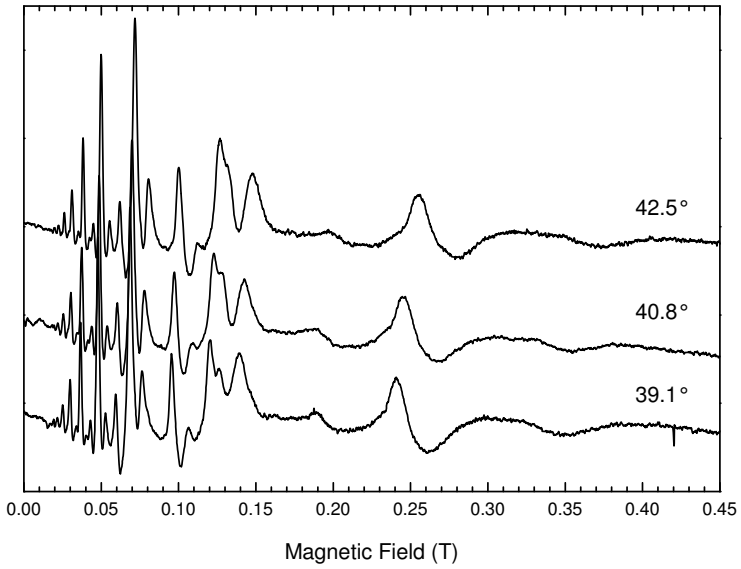


Figure 3.8: . Zoom of single crystal cyclotron resonances of natural graphite at 190 GHz (0.8 meV) and 5 K in the 40° region. The angles were varied in small steps (1.7°) due to the pronounced orientation effect, illustrating the high anisotropy of the system. The measurements was performed with the rotating sample holder (Fig. 3.5c).

as this is the beam waist where the magnetic field is most concentrated. However, the most convenient is to place the sample on the spherical mirror, which is easy to clean and where the beam remains well collimated (Table 4.2). We tried several times to place the sample (a single crystal) on the mesh but the observed performance of the FP resonator was worse than with the sample on the spherical mirror. We suppose that the sample on the mesh largely affects the coupling of the MW into the FP resonator. Hence, the bottom spherical mirror is used to load the sample (Fig. 4.4).

Powdered and liquid samples are deposited in a thin layer on the bottom spherical mirror. If possible, a film is prepared diluting the sample in toluene (or other solvent) together with polystyrene. The solution is placed on the mirror, and after evaporation of the solvent, a thin homogeneous film is formed on the mirror. Single crystals are placed directly at the mirror centre. For an optimal performance of the FP resonator, the size of the measured crystal should not exceed $\lambda/4$.

The performance of a FP resonator is best described by its finesse $F$ rather than by its quality factor Q. The finesse is defined by $F = Q/q$ where $q$ is the order of the longitudinal mode. In our FP resonator, at 283.2 GHz, the measured finesse $F_{exp}$ can reach values up to $\sim 400$ depending on the mode considered and on the sample. For example, in the case of a graphite grain, $F_{exp}$ varies from 140 to 200 whereas it reaches 400 for a thin polystyrene film containing BDPA ($\alpha,\gamma$-bisdiphenylene-$\beta$-phenylallyl) radical deposited on the mirror (Fig. 3.6). This is a good result as the theoretical value is about $\approx$1800.

Further information about the mirrors and the FP resonator construction will be given in the following Chapter 4.

**Rotating sample holder:** The rotating holder (Figs. 3.5c and 4.10) is used for orientation studies of single crystals. The system relies on a rotating piezoelectric nanopositioner

ANRv50 (Attocube systems AG) with a resistive encoder allowing an absolute measurement of the angle. The calibrated encoder enables the direct measurement of the position in the range $0° - 337°$. Due to the lack of space in the cryostat, it is not possible to use directly the piezoelectric element to rotate the sample holder. Thus, a gear mechanism had to be introduced, with one gear driven by the rotating piezoelectric device. The driven gear bears the Teflon holder for the sample. The mechanical gear is responsible for the main uncertainty on the rotation position, which is however less than 1°. A direct use of the rotating piezoelectric nanopositioner should decrease this uncertainty by one order of magnitude. A flat brass gold plated mirror is placed below the sample for the reflection of the MW. A smooth guide having 6 mm inner diameter is used to propagate the MW from the corrugated taper to the top of the gear mechanism, a few millimetres apart from the sample. Similarly to the FP resonator, a modulation coil is wound directly onto the Torlon housing of the rotating sample holder. It has a maximum field amplitude of 25 G (with respect to only 10 G for the Fabry-Pérot system), as a consequence of the smaller dimensions of the rotating holder assembly.

## 3.4 EPR Signal Detection

For the detection either an InSb hot electron bolometer (QMC Instruments Ltd) or heterodyne detection (Radiometer Physics GmbH.) is used. Whereas the bolometer covers broad frequency range and is used for multi-frequency EPR, the fast heterodyne detection is available only for one particular frequency of 283.2 GHz. Both types of detection are discussed in the following.

### 3.4.1 Homodyne Detection - Bolometer

The Indium Antimonide (InSb) hot electron bolometer, working at liquid helium temperature, has an excellent detection sensitivity over a large frequency range and covers completely our set of available irradiation sources (Table 3.1). However, this bolometer, due to its slow time response ($\sim 1\,\mu$s), is only suitable for cw-EPR experiments. A lock-in technique is employed for the detection of the cw-EPR signal. After a first amplification stage, the signal from the detector is fed into a Lock-In amplifier (Stanford SR830) which is used to decode the EPR signal at the frequency of the modulation field.

### 3.4.2 Superheterodyne Detection

The superheterodyne detection has a sensitivity comparable to the bolometer, but without the cryogenic of the bolometer requirements. However, it is applicable only for one particular frequency. The superheterodyne detection has a very fast response of the order of a few nanoseconds, which in principle enables pulsed-HF-EPR.

A first heterodyne detection scheme was developed for the work with the 141.6 GHz Gunn diode. However, as the 141.6 GHz Gunn diode was irreparably damaged, a new detection scheme has been implemented recently to work with the new DRO source. We will describe here both systems.

**Old: Superheterodyne detection with 141.6 GHz Gunn diode source:** The superheterodyne detection (Fig. 3.9) uses two phase-locked Gunn diodes, 141.6 GHz and 95 GHz (both Radiometer Physics GmbH.), which are locked to the same 100 MHz stable Quartz oscillator (master reference). The frequencies of the Gunn diodes are multiplied to 283.2 GHz (excitation $f_{ex}$) and 285 GHz (local oscillator $f_{LO}$) frequencies by a doubler and a tripler, respectively. These frequencies are then mixed in the tuned harmonic mixer (GaAs Shottky diode). The mixing product 1.8 GHz intermediate frequency $f_{IF}$ is amplified, filtered and rectified using a cascade of amplifiers (Mini-Circuits), a band pass filter (BPF) (Mini-Circuits) and a detector (Huber+Suhner AG). The rectified signal is then processed by a Lock-In Amplifier for cw-EPR (Stanford SR830) or by an Oscilloscope for pulsed-EPR (LeCroy waveRunner 6050A); the configuration shown in Fig. 3.9 is complete for cw-EPR. In the pulsed mode, a 141 GHz PIN switch (Elva-1) is inserted between the isolator and doubler to create the MW pulses.

All the results presented in this manuscript have been obtained with this set-up.

**New: Superheterodyne detection with actively multiplied DRO source:** The new superheterodyne detection uses two sources locked to the same 100 MHz master reference frequency (Radiometer Physics AG.). The irradiation (excitation) source consists now of a phase-locked 7.8655 GHz synthetiser (DRO) multiplied to 94.4 GHz and tripled to 283.2 GHz. For the harmonic mixer the same 285 GHz local oscillator (Fig. 3.9) is used. The final detection of the intermediate frequency $f_{IF}$=1.8 GHz was modified, see Fig. 3.10.

The $f_{IF}$ signal goes through a variable attenuator with 30 dB maximum attenuation (MCLI Inc.) before it is sent to a 68 dB amplifier (Miteq Inc.). Afterwards it is directed by a computer controlled non-reflective switch (ACC Inc.) either to the cw-EPR arm or to the pulsed-EPR arm, or to the spectrum analyzer arm. In the cw-EPR arm, the signal passes through a 15 MHz BPF (Micro-Tronics Inc.) and a tunnel detector (ACC Inc.) to be fed into the lock-in amplifier (Stanford SR830). In the pulsed EPR arm, the $f_{IF}$ signal is additionally amplified with a 48 dB amplifier (Miteq Inc.) in order to detect a weak echo signal, filtered with a 100 MHz BPF (Micro-Tronics Inc.) and detected by a tunnel detector (ACC Inc.) before it is read on the Oscilloscope (LeCroy). For the tuning of the FP resonator, the $f_{IF}$ signal is sent to a spectrum analyzer (Rohde & Schwartz FSP13), see Fig. 3.10.

## 3.5 Magnet and Cryostat

The sample is placed in the center of the superconducting magnet (Cryogenics Ltd.) which has a maximum field of 12 T. The bipolar power supply ($IPS^{120-10}$, Oxford Instruments) allows sweeping the magnetic field from -12 to +12 T with maximal resolution of 17 $\mu$T. The field of 12 T corresponds to the maximum frequency of 335 GHz for $g = 2$. The magnet is equipped with a variable temperature insert (VTI), with an inner diameter of 30 mm, which enables measurements from 1.5 K up to room temperature. The temperature at the sample is regulated by a liquid helium flow (adjusted manually) which is taken from the magnet reservoir. The liquid helium is pumped through a needle valve into the sample space, where it is warmed by a heater controlled by an $ITC^{503}$ (Oxford Instruments).

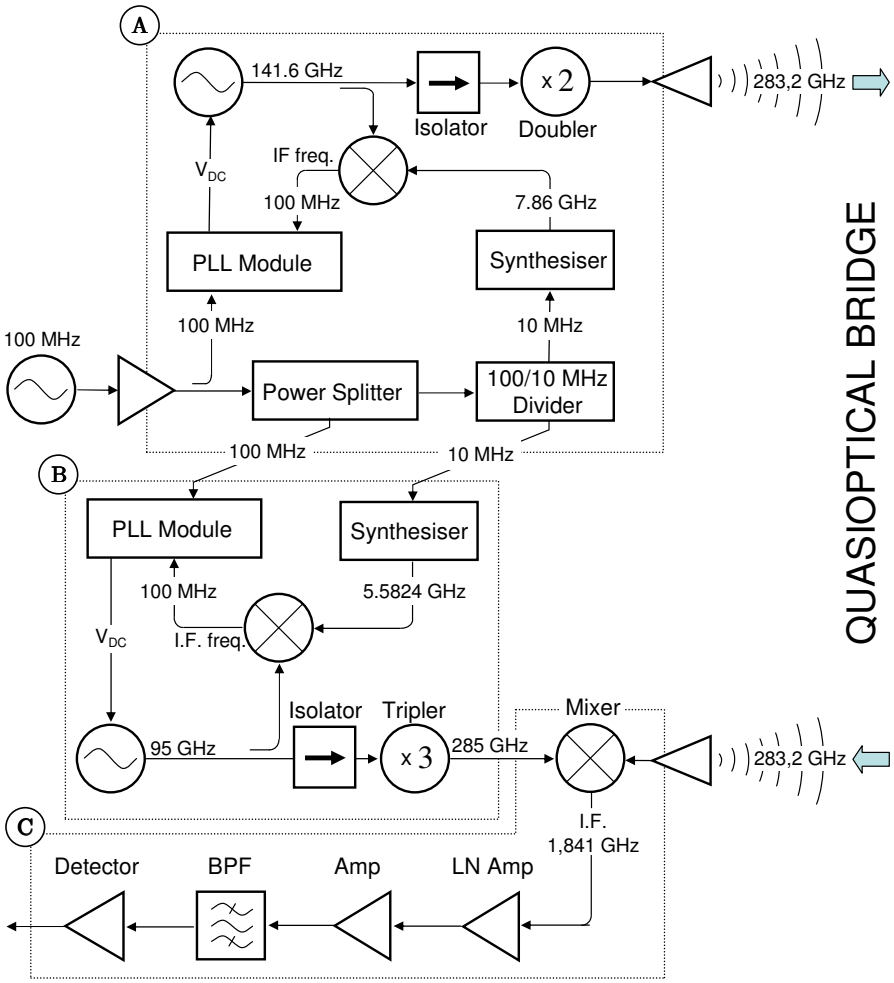


Figure 3.9: The superheterodyne detection (Radiometer Physics AG.) uses two phase-locked Gunn diodes 141.6 Ghz (A) and 95 GHz (B) which are locked to the same 100 MHz master reference frequency. The frequencies of the Gunn diodes are multiplied to 283.2 GHz (excitation $f_{ex}$) and 285 GHz (local oscillator $f_{LO}$) frequencies by a doubler and a tripler, respectively. These frequencies are then mixed in the tuned harmonic mixer (C). The mixing product 1.8 GHz intermediate frequency $f_{IF}$ is amplified, filtered and rectified on a cascade of amplifiers (Mini-Circuits), a band pass filter (BPF) (Mini-Circuits) and a detector (Huber+Suhner AG), respectively (C). The rectified signal is then processed by a Lock-In Amplifier for cw-EPR (Stanford SR830) or by an Oscilloscope for pulsed-EPR (LeCroy waveRunner 6050A); the configuration is complete for the cw-EPR. In the pulsed mode, a 141 GHz PIN switch (Elva-1) is inserted between the isolator and the doubler to create the MW pulses.

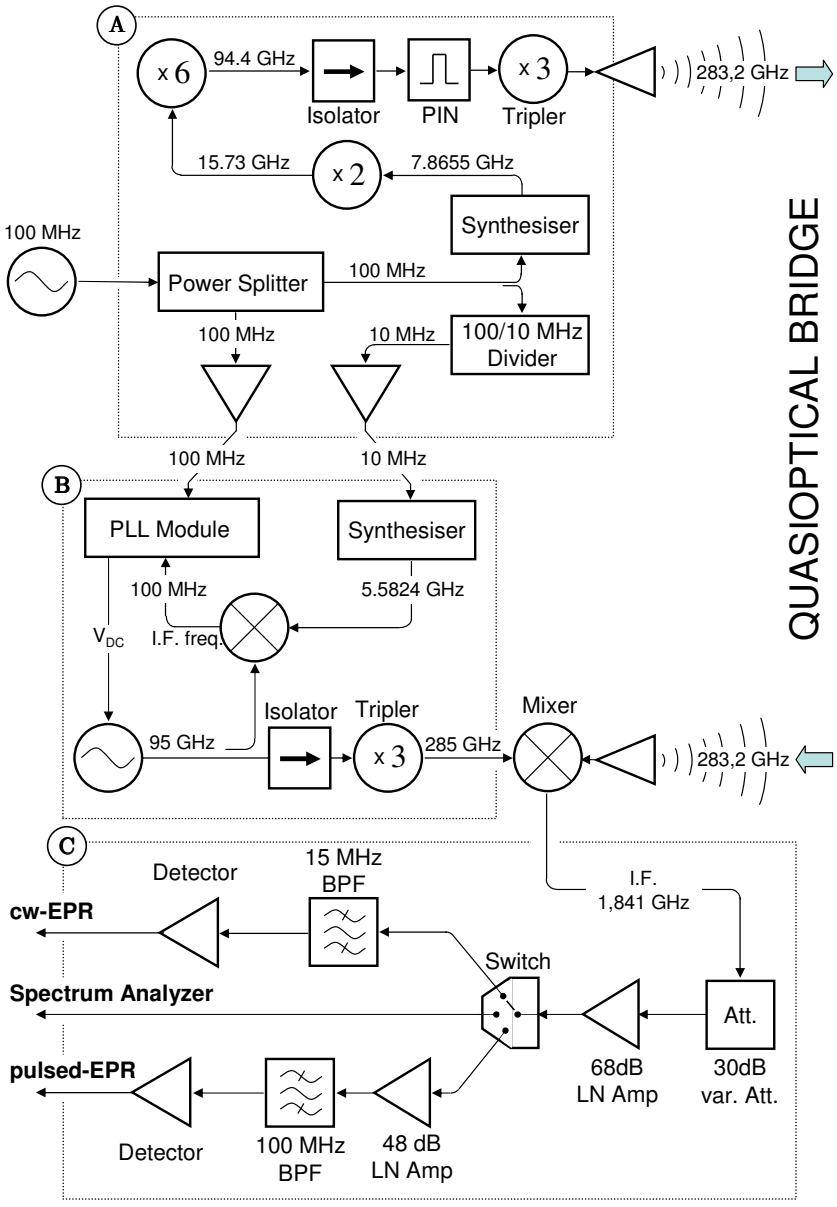


Figure 3.10: The second superheterodyne detection uses two sources locked to 100 MHz master reference frequency (Radiometer Physics AG.). (A) The irradiation (excitation) source consists of phase-locked 7.8655 GHz synthetsiser (DRO) multiplied to 94.4 GHz and tripled to 283.2 GHz. (B) For the harmonic mixer the same 285 GHz local oscillator is used Fig. 3.9. (C) Detection, the $f_{IF}$=1.8 GHz signal goes through a variable attenuator with 30 dB maximum attenuation (MCLI Inc.) before it is sent to a 68 dB amplifier (Miteq Inc.). Afterwards it is directed by a computer controlled non-reflective switch (ACC Inc.) either to the cw-EPR arm or the pulsed-EPR arm, or to the spectrum analyzer arm. In the cw-EPR arm, the signal passes through a 15 MHz BPF (Micro-Tronics Inc.) and a tunnel detector (ACC Inc.) to be fed into the lock-in amplifier (Stanford SR830). In the pulsed EPR arm, the $f_{IF}$ signal is additionally amplified with a 48 dB amplifier (Miteq Inc.), filtered with a 100 MHz BPF (Micro-Tronics Inc.) and detected by a tunnel detector (ACC Inc.) before it is read on the Oscilloscope (LeCroy). For the necessary tuning of the FP resonator, the $f_{IF}$ signal is sent to a spectrum analyzer (Rohde & Schwartz FSP13).

## 3.6 Experiment Control and Data Acquisition

During this work, a LabView program for the control of the HF-EPR spectrometer and the data acquisition has been written. It allows a simple and flexible control of the electronics of the EPR spectrometer for cw-EPR experiments. It is structured in blocks allowing extensions of the program for pulsed operation for instance. The LabView program is described in Appendix B.

## 3.7 HF-EPR Spectrometer Sensitivity

The measured absolute sensitivity of the EPR spectrometer operating in the continuous mode with the FP resonator and in the superheterodyne configuration is $3 \times 10^8$ spins/G $\cdot$ $\sqrt{\text{Hz}}$ at room temperature. This value has been determined with a thin film of $\alpha,\gamma$-bisdiphenylene-$\beta$-phenylallyl (BDPA) radical as reference sample. BDPA was diluted in polystyrene and dissolved in toluene; the solution was placed on the bottom mirror of the FP resonator. The FP resonator was working with a mesh of 75 lines/inch (2.95 lines/mm) and lines of 200 $\mu$m width; the spherical mirror had a 50 mm radius of curvature. This configuration resulted in finesse $F \sim 400$ (Fig. 3.6).

## 3.8 Conclusion

The chapter describes the whole HF-EPR spectrometer with all its specifications. The performance of the FP resonator and the rotating holder, developed during this work, have been demonstrated in Figs. 3.7, 3.6 and 3.8 (see also Ref. [68]). The description of the resonator design is given in Chapter 4. The spectrometer together with the developed holders (the FP resonator and the rotating holder) were used in the experimental part of this thesis (Chapters 5 and 6).

While the implementation of the superheterodyne detection, necessary for the pulsed operation, was successful, problems with the 283.2 GHz excitation source resulted in the failure of the Gunn diode and led to the replacement of the whole excitation source by a new one. The delay in the fabrication of the new 283.2 GHz source and its adaptation to the existing setup did not allow us to perform the basic spin-echo experiment before the submission of this manuscript.

# Résumé Chapitre 4

## Conception du Résonateur Fabry-Pérot

Alors que les spectromètres RPE en mode continu (cw-RPE) ne nécessitent pas de résonateurs (cavités), ces composants sont indispensables en mode pulsé, particulièrement pour les appareils fonctionnant à hautes fréquences, 100 GHz et plus. A partir de l'approche d'autres groupes [8, 9, 12, 13, 21, 23, 27, 28, 45, 48, 55, 66, 69, 70], nous avons décidé de concevoir un résonateur FP plus facile d'accès qu'une cavité à monomode [57]. Nous avons développé des résonateurs FP en configuration semi-symétrique (Fig. 4.1). Nous avons dû faire face à plusieurs restrictions dans la conception de notre résonateur FP: en particulier le diamètre extérieur total ne devait pas excéder 30 mm (imposé par les dimensions du cryostat) et le résonateur devait pouvoir travailler à des températures cryogéniques, avec de nombreux cycles thermiques.

**Miroirs sphériques:** Le résonateur FP est conçu pour utiliser des miroirs concaves commerciaux. Les miroirs sont préparés à partir de verre poli recouvert d'or. Parmi les modèles disponibles, seuls les miroirs avec des rayons de 9 mm (Edmund Optics Ltd.), 25 et 50 mm (Thorlabs Gmbh) se sont révélés compatibles avec notre dispositif.

**Miroirs semi-transparents - Réseau:** Les micro-ondes sont couplées à l'intérieur du résonateur FP au travers d'un miroir semi-transparent plan (réseau inductif carré). Les réseaux commerciaux disponibles sont le plus souvent préparés par galvanoplastie. De tels réseaux se présentent comme de fins feuillets souples difficiles à manipuler. Aussi nous avons principalement utilisé des réseaux que nous avons fabriqués par lithographie UV en utilisant des lamelles de microscopie en verre ou en quartz comme substrat. Dans ce cas, les réseaux obtenus possèdent les propriétés requises et sont en plus facilement manipulables. Parmi la liste de réseaux préparés selon cette méthode, le plus utilisé a été celui présentant une périodicité de 75 lignes/inch ce qui correspond à un espacement entre lignes $g$ de 0.34 mm. La largeur des fils conducteurs vaut $2a = 200\,\mu$m.

**Ajustement des miroirs du résonateur FP:** Afin d'obtenir la meilleure performance possible du résonateur FP, les miroirs doivent être ajustés le plus précisément possible l'un par rapport à l'autre, parfaitement alignés par rapport à l'axe optique et positionnés correctement à l'extrémité du cône QO. L'espacement entre les miroirs dans notre résonateur FP peut être ajusté sur une plage de 2.5 mm à l'aide du nanopositionneur piezoélectrique ANPz50 (Attocube systems AG) avec une haute précision ($< 100$ nm).

**Choix du matériau:** La partie principale du résonateur FP doit être réalisée à partir d'un matériau non magnétique et isolant (diélectrique). Ceci permet d'éviter les effets de vibrations microphoniques à l'intérieur du résonateur FP dus à la bobine de modulation (courants de Foucault). Nous avons étudié plusieurs matériaux disponibles et généralement utilisés en RPE (Fig. 4.6), qui pourraient convenir à la fabrication du résonateur. Le Torlon a été choisi car il est communément utilisé au laboratoire et a l'avantage d'être résistant aux cycles thermiques. Les groupes RPE de Berlin et St. Andrews utilisent un matériau similaire, appelé Tufnol (Tufnol Ltd.) [13, 18].

**Bobine de modulation:** Pour la RPE en mode continu, un champ magnétique oscillant $B_{mod}$ avec une fréquence associée $f_{mod.}$ est superposé au champ magnétique principal $B$ qui varie lentement. La bobine de modulation du résonateur FP est un solénoïde fabriqué à partir de fil de cuivre : son support est centré sur l'axe du cône QO et fixé sur celui-ci pour assurer un bon alignement optique (Fig. 4.4). Un champ d'environ 8 G (pour un courant de 70 mA à 0.7 kHz) est obtenu comme modulation maximale avec ce système.

**Chargement de l'échantillon:** Cette opération est un point crucial lors de l'utilisation des résonateurs. Aussi, nous avons mis au point un assemblage des éléments du résonateur qui permet de placer l'échantillon de façon commode et facile, comme illustré Fig. 4.4.

**Conclusion:** Le résonateur FP décrit ci-dessus peut être utilisé sur une très large bande de fréquence. Néanmoins, l'objectif principal a été de construire un résonateur FP en améliorant l'appareil RPE en mode continu et multi-fréquences, pour parvenir à un spectromètre RPE-HF travaillant en mode pulsé à 283.2 GHz. La finesse mesurée expérimentalement $F_{exp}$ à 283.2 GHz atteint des valeurs proches de 400 selon le mode du résonateur considéré et l'échantillon (Fig. 4.8). Il s'agit d'un bon résultat, en comparaison avec la valeur théorique de 1800 pour la finesse. La finesse obtenue indique que le résonateur FP peut être utilisé pour des mesures RPE en mode pulsé. Ce résultat est en bonne partie dû à l'utilisation du nanopositionneur piézoélectrique. A notre connaissance, tous les résonateurs FP utilisés jusqu'à présent dans des expériences de RPE sont ajustés mécaniquement.

# Chapter 4

# Fabry - Pérot Resonator Design

Whereas continuous wave EPR (cw-EPR) can be performed even without resonators (cavities), in the pulsed EPR, resonators are still an essential part of all spectrometers, especially those which operate at high frequencies (100 GHz and higher). MW sources often do not provide enough power to provide short $\pi/2$ pulses; hence efficient resonators or cavities are needed. Having in mind the wavelength of 1 mm of MW at 300 GHz and the precision with which the cavity has to be created with respect to the wavelength, it is then obvious that a single-mode cavity is extremely difficult to fabricate by conventional methods. However, the group of Prof. J. Schmidt in Leiden [57] have demonstrated a mechanically tuned single-mode cavity at 275 GHz. Following the approach of other groups [8, 9, 12, 13, 21, 23, 27, 28, 45, 48, 55, 66, 69, 70], we decided to design a more feasible Fabry - Pérot (FP) resonator which would allow us to perform pulsed HF-EPR experiments around 285 GHz. FP resonators do not enable such large conversion factors (Eq. (1.6)) as single-mode cavities but on the other hand they allow multi-frequency EPR which is part of our main interest and are also much easier to handle.

There are several restrictions in the design of our FP resonator. The most important one is that the outer diameter of the FP resonator is limited by the inner dimensions of our variable temperature insert (only 30 mm). Furthermore, the FP resonator must permit work at cryogenic temperatures as well as at room temperature. These restrictions are rather difficult to satisfy. Nevertheless, choosing a careful construction of the FP resonator can lead to success.

## 4.1 Half-Symmetric Fabry - Pérot Resonators

FP resonators in a half-symmetric configuration are commonly used [12, 13, 27, 54, 55, 69, 70]. They are created by one flat semitransparent mirror (mesh) and one spherical mirror with radius $R$, spaced by a distance $L$, see Fig. 4.1. The coupling of the MW into the FP resonator is made through a mesh which is at a distance $z$ from the corrugated taper. Such a FP resonator works in reflection mode and can be considered to have 4 times higher sensitivity than those which operate in transmission mode [16]. To perform cw-EPR experiments the FP resonator is surrounded by a modulation coil.

In Chapter 2, it was mentioned that the performance of the FP resonators depends on the reflection coefficients only (Eq. (2.19)). Nevertheless, this statement is valid for ideal FP resonators only. In general, the mirrors' sizes, their coatings and the tuning precision

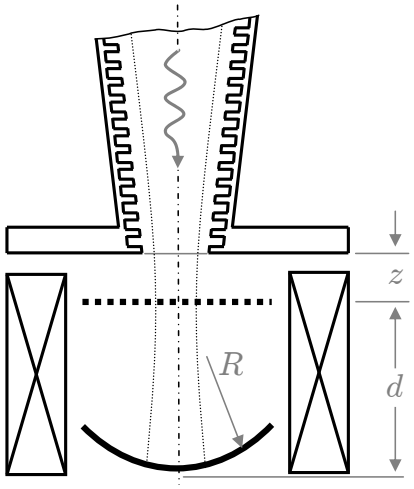


Figure 4.1: A FP resonator in the half-symmetric configuration is created by one flat semitransparent (mesh) and one spherical mirror with radius $R$, spaced by a distance $L$. The coupling of the MW into the FP resonator is made through the mesh which is at a distance $z$ from the corrugated taper. For the continuous wave EPR (cw-EPR) experiments the FP resonator is surrounded by a modulation coil.

of the mirrors define the performances of the FP resonators. The sizes of the mirrors affect diffraction losses in the FP resonator, whereas the reflection coefficients are directly governed by the quality of the metal coatings and the surface roughness of the mirrors. The aperture radius of the mirrors has to be at least 2.5 times the size of the beam radius $w$ on the mirror (Fig. 2.6) to minimize diffraction losses [53].

The skin (penetration) depth $\delta$ is important to define the thickness of the metallic coating of the mirrors:

$$\delta = \sqrt{\frac{\rho}{\pi \mu_0 f}} = \sqrt{\frac{2}{\sigma \mu_0 \omega}}, \tag{4.1}$$

where $\rho$ is the bulk resistivity of the metal that is used, $f$ is the MW frequency, $\sigma$ is the conductivity and $\omega$ is the angular frequency. The thickness of the metal coating of the mirrors has to be several times bigger than the skin depth of the MW (see Table 4.1). Nevertheless, the thickness has to be smaller than the skin depth of the modulation frequency[1] in order to avoid mirrors (cavity) vibrations (microphonics) [15].

The properties of the mirrors also depend on the coating technology, which affects the bulk resistivity of the metal. This is valid especially for meshes prepared by electroforming, sputtering or evaporation of a metal. The bulk resistivity of the metal approaches the theoretical value when sputtering or evaporation are used [53]. For instance, meshes prepared by UV-lithography (described in Appendix C) generally have a better resistivity than those prepared by electroforming.

### 4.1.1 Spherical Mirror

The radius of the spherical mirror $R$ and the spacing of the mirrors $L$ define the type of the half-symmetric FP resonator in the stability diagram. The properties of the FP resonator can be estimated from its position in the stability diagram (Fig. 2.7). The spherical mirror determines the coupling efficiency between the corrugated taper and the FP resonator. The optimally coupled FP resonator has a mirror radius $R$ corresponding to the wave front radius $\mathcal{R}$ of the MW (Table 4.3).

[1] The skin depth is $\delta \approx 7\,\text{mm}$, for gold coated mirror at 293 K and for 1 kHz modulation frequency.

Table 4.1: The bulk resistivity $\rho$ ($10^{-8}\,\Omega$m) for selected materials [71] and calculated corresponding skin depth $\delta$ (nm) for frequency 285 GHz and given temperatures.

| **Temp.** | **Au** | | **Ag** | | **Cu** | | **Al** | |
|---|---|---|---|---|---|---|---|---|
| **(K)** | $\rho$ | $\delta$ | $\rho$ | $\delta$ | $\rho$ | $\delta$ | $\rho$ | $\delta$ |
| 10 | 0.0226 | 14.2 | 0.00115 | 3.2 | 0.00202 | 4.3 | 0.000193 | 1.3 |
| 60 | 0.308 | 52.6 | 0.162 | 38.1 | 0.0971 | 29.5 | 0.0959 | 29.3 |
| 100 | 0.650 | 76.4 | 0.418 | 61.3 | 0.348 | 55.9 | 0.442 | 63.0 |
| 293 | 2.214 | 141.0 | 1.587 | 119.4 | 1.712 | 124.0 | 2.65 | 154.3 |

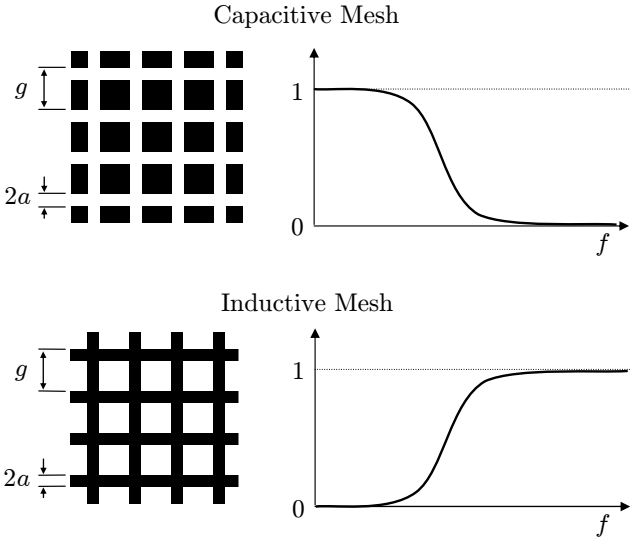


Figure 4.2: The two types of two dimensional non polarising meshes, capacitive (up) and complementary inductive mesh (down). The mesh is characterized by the parameters $g$ and $2a$. The metallic part of the mesh is represented by the black region. On the right hand side, the frequency transmission function of the corresponding mesh is shown.

The FP resonator is designed to use commercial concave mirrors from Edmund Optics or Thorlabs (Table 4.3). The mirrors are made from polished glass coated by aluminum or gold. The coating is about 1 $\mu$m thick. The aluminum coated mirrors are overcoated by gold after delivery. From the available set of mirrors, only the mirrors with a 9 mm radius (Edmund Optics Ltd.) and mirrors with 25 and 50 mm radii (Thorlabs GmbH) were found suitable. The mirror with a 9 mm radius is suitable due to its smaller effective cavity volume [9]. On the other hand, the mirrors with 25 and 50 mm radii offer much better MW coupling and are mostly used.

### 4.1.2 Semitransparent Mirror - Mesh

The MW is coupled into the FP resonator through the planar semitransparent mirror. Metallic meshes, in which the metal is arranged in a defined repetitive pattern, are used as semitransparent mirrors. The properties of the mirror thus depends on the type of the repetitive pattern (square, cross, Jerusalem cross, etc.) as well as on its size and periodicity [53, 72, 73]. Hence, the variety is very large. However, mostly meshes with square symmetry (Fig. 4.2) are used for simplicity and also because they do not affect the polarisation state of the MW for the normal angle of incidence.

There are two general types of squared meshes referred to as inductive and capacitive.

**285 GHz**
$\lambda$ = 1.052 mm, $z_c$=11.097 mm

| $q$ | $\mathcal{R}$ (mm) | $L$ (mm) | $2\omega$ (mm) | $\mathbf{g}_1$ |
|---|---|---|---|---|
| 1. | 234.68 | 0.526 | 3.86 | 0.998 |
| 2. | 118.13 | 1.052 | 3.87 | 0.991 |
| 3. | 79.63 | 1.578 | 3.89 | 0.980 |
| 4. | 60.64 | 2.104 | 3.92 | 0.965 |
| 5. | 49.46 | 2.630 | 3.96 | 0.947 |
| 6. | 42.18 | 3.156 | 4.01 | 0.925 |
| 7. | 37.13 | 3.682 | 4.06 | 0.901 |
| 8. | 33.48 | 4.208 | 4.12 | 0.874 |
| 9. | 30.75 | 4.734 | 4.19 | 0.846 |
| 10. | 28.68 | 5.260 | 4.27 | 0.817 |
| 11. | 27.07 | 5.785 | 4.35 | 0.786 |
| 12. | 25.82 | 6.311 | 4.44 | 0.755 |

**283.2 GHz**
$\lambda$=1.0592 mm, $z_c$=11.028 mm

| $q$ | $\mathcal{R}$ (mm) | $L$ (mm) | $2\omega$ (mm) | $\mathbf{g}_1$ |
|---|---|---|---|---|
| 1. | 230.29 | 0.529 | 3.86 | 0.998 |
| 2. | 115.94 | 1.059 | 3.87 | 0.991 |
| 3. | 78.18 | 1.588 | 3.90 | 0.980 |
| 4. | 59.56 | 2.117 | 3.93 | 0.965 |
| 5. | 48.60 | 2.646 | 3.96 | 0.946 |
| 6. | 41.47 | 3.176 | 4.01 | 0.923 |
| 7. | 36.53 | 3.705 | 4.07 | 0.899 |
| 8. | 32.95 | 4.234 | 4.13 | 0.872 |
| 9. | 30.29 | 4.764 | 4.20 | 0.843 |
| 10. | 28.27 | 5.293 | 4.28 | 0.813 |
| 11. | 26.71 | 5.822 | 4.36 | 0.782 |
| 12. | 25.50 | 6.352 | 4.45 | 0.751 |

**230 GHz**
$\lambda$=1.304 mm, $z_c$=8.965 mm

| $q$ | $\mathcal{R}$ (mm) | $L$ (mm) | $2\omega$ (mm) | $\mathbf{g}_1$ |
|---|---|---|---|---|
| 1. | 123.98 | 0.658 | 3.87 | 0.995 |
| 2. | 62.97 | 1.304 | 3.90 | 0.979 |
| 3. | 43.06 | 1.955 | 3.95 | 0.955 |
| 4. | 33.44 | 2.606 | 4.02 | 0.922 |
| 5. | 27.92 | 3.259 | 4.10 | 0.883 |
| 6. | 24.46 | 3.910 | 4.21 | 0.840 |
| 7. | 22.18 | 4.562 | 4.33 | 0.794 |
| 8. | 20.63 | 5.213 | 4.46 | 0.747 |
| 9. | 19.57 | 5.866 | 4.61 | 0.700 |
| 10. | 18.85 | 6.517 | 4.77 | 0.654 |
| 11. | 18.38 | 7.169 | 4.94 | 0.610 |
| 12. | 18.10 | 7.821 | 5.12 | 0.568 |

**190 GHz**
$\lambda$=1.579 mm, $z_c$=7.411 mm

| $q$ | $\mathcal{R}$ (mm) | $L$ (mm) | $2\omega$ (mm) | $\mathbf{g}_1$ |
|---|---|---|---|---|
| 1. | 70.40 | 0.789 | 3.88 | 0.989 |
| 2. | 36.38 | 1.579 | 3.94 | 0.957 |
| 3. | 25.57 | 2.367 | 4.05 | 0.907 |
| 4. | 20.56 | 3.156 | 4.19 | 0.846 |
| 5. | 17.87 | 3.945 | 4.37 | 0.779 |
| 6. | 16.33 | 4.734 | 4.58 | 0.710 |
| 7. | 15.47 | 5.522 | 4.81 | 0.643 |
| 8. | 15.01 | 6.311 | 5.07 | 0.579 |
| 9. | 14.83 | 7.100 | 5.34 | 0.521 |
| 10. | 14.85 | 7.889 | 5.64 | 0.469 |
| 11. | 15.01 | 8.678 | 5.94 | 0.422 |
| 12. | 15.27 | 9.467 | 6.26 | 0.379 |

Table 4.2: Calculation of the Gaussian beam evolution, from the waist (Table 4.5), of the first 12 modes after passing the corrugated taper for frequencies 285, 283.2, 230 and 190 GHz. Note: $q$ - mode number, $\mathcal{R}$ - wavefront radius, $L$ - spacing between mirrors, $2\omega$ - beam diameter, $g_1$ - $g$ parameter are calculated from $\mathcal{R}$ and $L$, and $z_c$ - is the confocal distance.

Table 4.3: The list of the commercially available concave mirrors tested in the FP resonator from Edmund Optics Ltd. (EO) and Thorlabs GmbH (Thor.) with the metallic coating of roughly 1 $\mu$m thick. Those mirrors with aluminum coatings were overcoated by gold after delivery. However, only mirrors with asterisk were found optimal and are used for the FP resonator now.

| **Mirror Curvature** $R$ **(mm)** | **Coating** |
|---|---|
| **9 (ø10 mm, EO)*** | **Gold** |
| 20 (ø10 mm, EO) | Aluminium |
| **25 (ø12.7 mm, Thor.)*** | **Gold** |
| 40 (ø10 mm, EO) | Aluminium |
| **50 (ø12.7 mm, Thor.)*** | **Gold** |
| 80 (ø10 mm, EO) | Aluminium |
| 100 (ø12.7 mm, Thor.) | Gold |

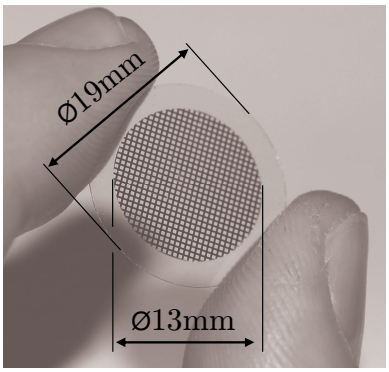


| lines/inch | lines/mm | $g$ ($\mu$m) | $2a$ ($\mu$m) | $A$ (%) |
|---|---|---|---|---|
| 50 | 1.97 | 508 | 200 | 36.76 |
| **75** | 2.95 | 338 | 200 | 16.67 |
| 75 | 2.95 | 338 | 100 | 42.58 |
| 100 | 3.94 | 254 | 70 | 52.48 |
| 150 | 5.91 | 169 | 70 | 34.32 |
| 175 | 6.89 | 145 | 70 | 26.75 |
| 200 | 7.87 | 127 | 70 | 20.14 |
| 275 | 10.83 | 92 | 35 | 38.38 |
| 350 | 13.78 | 72 | 28 | 37.34 |

Table 4.4: The table shows the inductive meshes home made by the UV-lithography, where $g$, $2a$ and $A$ represent the period, the thickness of the metallic wire and the open area of the mesh, respectively. The image shows an inductive mesh (ø13 mm) prepared on a ø19 mm × 0.17 mm fused silica cover glass (GOLD SEAL®). From the list of prepared meshes, the most often used mesh has 75 lines/inch (in bold).

The properties of inductive and capacitive meshes are complementary (Babinet principle) [72], see Fig. 4.2. The definition, inductive and capacitive, comes from the analogy with RLC circuits, where capacitors and inductors have similar frequency responses if they are connected in series and work as a high-pass or a low-pass frequency filters, respectively. A squared inductive mesh is made of a set of crossed flat conducting (metallic) wires of thickness $2a$ with period $g$. The corresponding complementary capacitive mesh is then a matrix of metallic squares of the edge $(g - 2a)$ with the same periodicity $g$ (Fig. 4.2).

The transmission and reflection properties of meshes, shown in Fig. 4.2, depend on the $2a$ and $g$ parameters with respect to the used MW. In HF-EPR spectroscopy, only inductive meshes are used. In the non-diffractive region ($g/\lambda < 1$), they act as high-pass filters (giving large reflection coefficients). Ideally, the transmission through the mesh is equal to the dissipated MW in the FP resonator together with the losses[2] in the mesh itself (critically coupled resonator).

The commercially available meshes are often prepared by electroforming. These electroformed meshes are thin freestanding sheets which make them difficult to manipulate.[3] The fine mesh has to be carefully stretched on a suitable dielectric substrate. The different temperature expansion coefficients of metallic meshes and dielectric substrates can lead to serious distortions of the meshes at cryogenic temperatures. These difficulties together with size limitations of commercially available meshes mean that these meshes are not suitable for EPR applications.

Photolithography [27, 72] applied on a suitable substrate allows creating metallic meshes of arbitrary shapes and parameters. The mesh created on a substrate is easy to manipulate, and its geometry is maintained by the substrate even at cryogenics temperatures. For our work, we took advantage of an in-house facility to realize our own meshes. We mainly concentrated on inductive meshes prepared by UV-lithography us-

[2]The resistive losses in wires of the mesh are proportional to $(g/2a)/\sqrt{\lambda}$ [72]. To minimize dielectric losses in the substrate, the substrate has to be as thin as possible.

[3]The commercially available meshes can be bought from Buckbee-Mears or any suppliers for the electron microscopy.

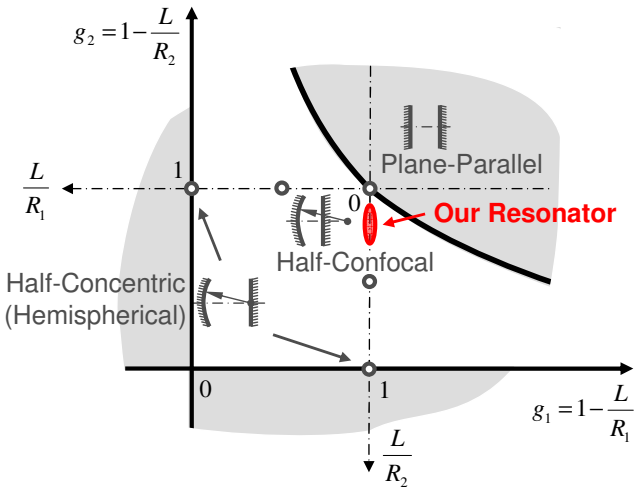


Figure 4.3: Localization of the FP resonator in the stability diagram, the FP resonator operates between half-confocal and plane-parallel configuration. Operation closer to plane parallel or half-confocal type depends on used spherical mirror (Table 4.3) and chosen FP resonator mode (Table 4.2).

ing either glass or quartz microscopy cover slips as substrates. The meshes prepared by this technique are shown in Table 4.4 and the UV-lithographical process is described in Appendix C.

Among the list of meshes, the most used one has the repetitive pattern of periodicity 75 lines/inch, which corresponds to a grid spacing $g = 0.34\,\text{mm}$. The width of the conducting wires is $2a = 200\,\mu\text{m}$. The $g/(2a)$ ratio reaches a value of 1.7 and describes the frequency dependence of the mesh reflectivity [16]. For $g/(2a) = 1.7$, the reflectivity is essentially constant for a reduced wavelength $g/\lambda$ ranging from 0 to 0.5 [16]. As our frequency range of interest corresponds to $g/\lambda$ varying between 0.2 and 0.32, the mesh has nearly constant reflectivity for the all available MW sources.

## 4.2 Adjusting the FP Resonator Mirrors

To obtain a high performance FP resonator, the mirrors have to be precisely adjusted with respect to each other as well as perfectly aligned with the optical axis and correctly positioned at the end of the corrugated taper. The chosen spherical mirror and operating mode define the location of the FP resonator in the stability diagram (Fig. 4.3) and thus the requirements on the alignment of mirrors as already discussed in Chapter 2.

The spacing of the mirrors can be adjusted (tuned) over a 2.5 mm range by the piezoelectric nanopositioner ANPz50 (Attocube systems AG) with high precision. The ANPz50 has small dimensions, 15 mm × 15 mm × 18 mm, and offers precise and comfortable tuning. In this way, we avoid the construction of a mechanism for precise tuning ($\ll 1\,\mu\text{m}$) of the FP resonator in the limited space given by the cryostat. To control the nanopositioner, we only need a simple twisted pair of wires to connect it electrically. The spacing between the mirrors is tuned in the whole 2.5 mm range with an extreme precision using a so-called slip-stick mechanism of piezoelectric-ceramic steps ($< 100\,\text{nm}$).

The tuning is made by moving the spherical mirror with respect to the static mesh (semitransparent mirror), where the metallic part of the mesh is facing the spherical mirror. The spherical mirror is centered on a piston to which it is attached (Fig. 4.4). The attachment can be either made by Stycast®(glue) or by Apiezon®(grease), when the

| **Frequency** $f$ **(GHz)** | **Beam Waist** $w_0$ **(mm)** | **Location** $z$ **(mm)** |
|---|---|---|
| 190 | 1.929 | 0.269 |
| 230 | 1.928 | 0.394 |
| 283.2 | 1.928 | 0.597 |
| 285 | 1.928 | 0.605 |

Table 4.5: The size of the beam waist $w_0$ and its location $z$ from the corrugated taper (Fig. 2.2) calculated for the frequencies 190, 230, 283.2 and 285 GHz by using Eqs. (2.5), (2.6) and (2.7). Further information about the Gaussian beam evolution can be found in Table 4.2.

attachment is permanent or nonpermanent, respectively. The piston with the mirror is mounted on the piezoelectric nanopositioner, covered by the housing and precisely moved in the housing by the nanopositioner with respect to the mesh on the top (Fig. 4.4). The 2.5 mm range of the nanopositioner allows tuning of the FP resonator over 5 modes at 283.2 GHz. The modes over which it is tuned is defined by the length of the piston. In our case, the tuning is performed from the $4^{th}$ to the $8^{th}$ mode of the FP resonator.

In order to optimally couple the MW into the cavity, the flat mirror (mesh) has to be adjusted with respect to the corrugated taper so that the mesh is in the waist location (planar beam front). In our case, the distance of the mesh to the end of the taper was calculated (see Table 4.5) using the inverse formulas described in Chapter 2. The position of the mesh is adjusted by a "tuning nut" at the bottom of the FP resonator (Fig. 4.5). The distance between the end of the taper and the mesh is controlled visually through the windows on the top of the resonator. When adjusting the mesh, the influence of the dielectric substrate of the mesh on the Gaussian beam has to be taken into account [74]. The waist is shifted by a value which depends on the thickness and the refractive index of the dielectric substrate. The refractive indices of the materials can be found in detail in Refs. [53, 67, 75] whereas the cover slips are discussed in Refs. [67, 76]. The refractive indexes of the commonly used materials HDPE[4] and quartz (glass) are about 1.5 and 2.2, respectively.

## 4.3 Choice of Material

The main body of the FP resonator should be made from nonmagnetic as well as nonconducting (dielectric) material. This reduces the effects of microphonics on the FP resonator caused by the modulation coil via eddy current. For dielectrics, the mechanical strains caused by the presence of a strong magnetic field are minimized and the reduction of the shielding of the modulation field allows higher effective modulation fields on the samples.

We have to insure that at cryogenic temperatures no problem will arise due to different coefficients of thermal expansion between dielectric parts (body of the FP resonator) and metallic parts (mirrors, piezoelectric nanopositioner, modulation coil) of the FP resonator. Dielectrics have thermal expansion coefficients roughly three times larger than metals. Thus combinations of metals and dielectrics at cryogenic temperatures can be very problematic. Such problems are overcome when only one material is used for the fabrication of the main body of the FP resonator and when large expansion spaces are left between the metal and dielectrics parts.[5]

[4]High Density PolyEthylene, 1 mm thick disk of HDPE was used for support of electroformed meshes, when we deal with them.

[5]This is not valid for meshes prepared by UV-lithography, where the metallic mesh is created directly

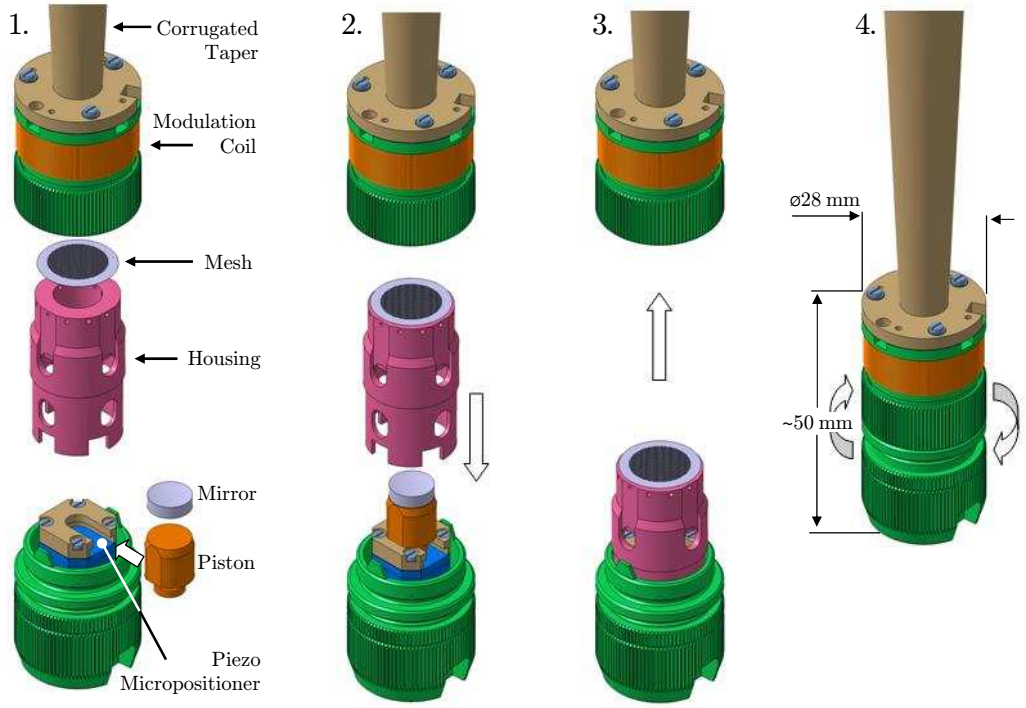


Figure 4.4: Sample loading: (1) The sample is placed on the spherical mirror which is attached to a piston. The attachment can be either made by Stycast®(glue) or by Apiezon®(grease), when the attachment is permanent or nonpermanent, respectively. (2) Then the piston with the mirror is mounted on the piezoelectric nanopositioner. The piston with the mirror is together with the piezoelectric nanopositioner covered by a housing. (3 and 4) Finally the resonator is screwed to the corrugated waveguide and surrounded by the modulation coil, see Fig. 4.5 for details.

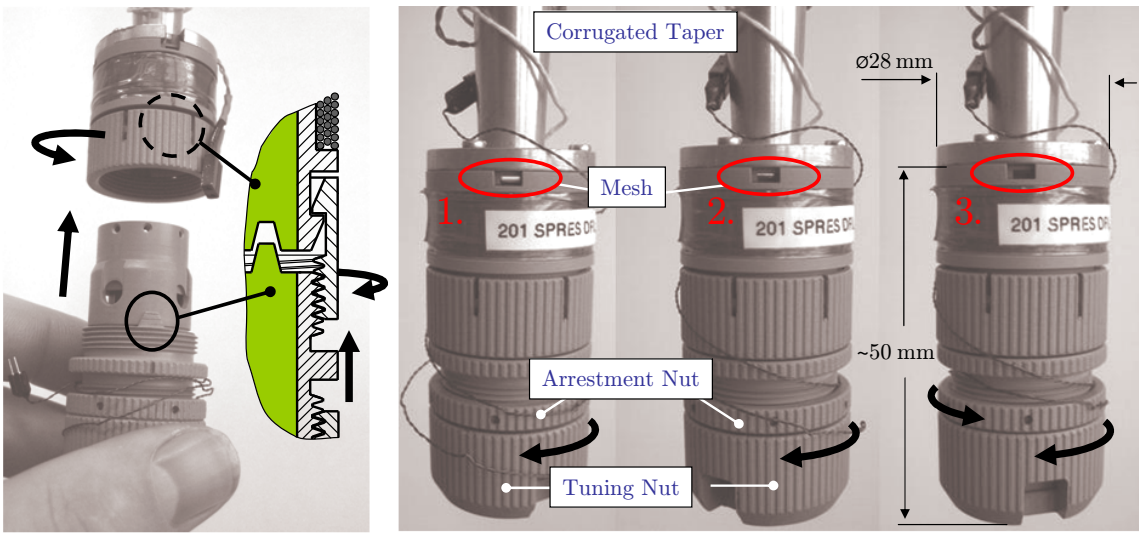


Figure 4.5: Details of the mounting of the FP resonator to the corrugated waveguide (left) and adjusting of the mesh with respect to the end of the corrugated taper (right). The MW is coupled into the FP resonator via the mesh, which position can be adjusted by a screw on the bottom of the resonator (Tuning Nut). The mesh position is controlled visually by windows above the modulation coil, when the position is found, the tuning screw is arrested (Arrestment Nut).

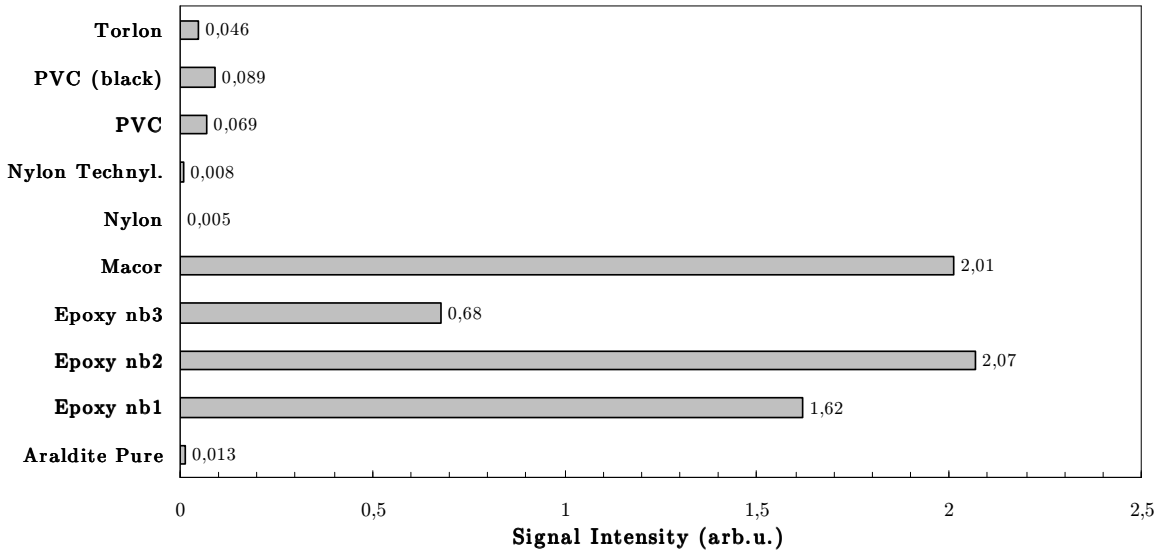


Figure 4.6: Intensity of the most intense spurious EPR signals ($g$=2) from different materials, which were all tested as potential candidates for the FP Resonator fabrication. EPR measurements were performed with the same modulation, on samples of normalized (same) sizes and at temperatures 5, 10 and 30 K.

We have studied several materials, available and commonly used in our workshop (Fig. 4.6), which could be suitable for the fabrication of the FP resonator. Our aim was to find a material giving a spurious EPR signal as small as possible, easy to machine as well as robust with respect to the temperature cycling.

The EPR study of the available materials (Fig. 4.6) was made for normalized sample sizes (ø8 mm × 10 mm). Before performing the experiment at 5, 10 and 30 K in the transmission EPR setup, the samples were washed in an ultrasound bath to remove traces remaining after the preparation. The results of this EPR study are presented in Fig. 4.6, where the line intensities are taken from peak to peak heights. This study eliminates the Macor and all types of epoxy which gave large spurious signal with respect to other materials.

The materials such as Torlon, PVC, Nylon are easy to machine into a required shape with a given precision. Nylon gives the smallest EPR signal but is not suitable for operation at cryogenic temperatures and the temperature cycling as it usually breaks after several cycles. Torlon is largely used in the laboratory and has proven to be robust to thermal cycling; therefore Torlon was selected. Groups from Berlin and St. Andrews use a similar material called Tufnol (Tufnol Ltd.) [13, 18].

## 4.4 Modulation Coil

For cw-EPR, an oscillating field $B_{mod}$ with frequency $f_{mod.}$ is superimposed to the slowly varying magnetic field $B$. The modulation coil of the FP resonator is a solenoid made of 200 turns of a 0.25 mm diameter copper wire, wound on a diameter of 24 mm over height

on the dielectric substrate. The thin mesh is thus deformed by the substrate at a cryogenic temperature. However, no damages of the meshes were observed under the microscope.

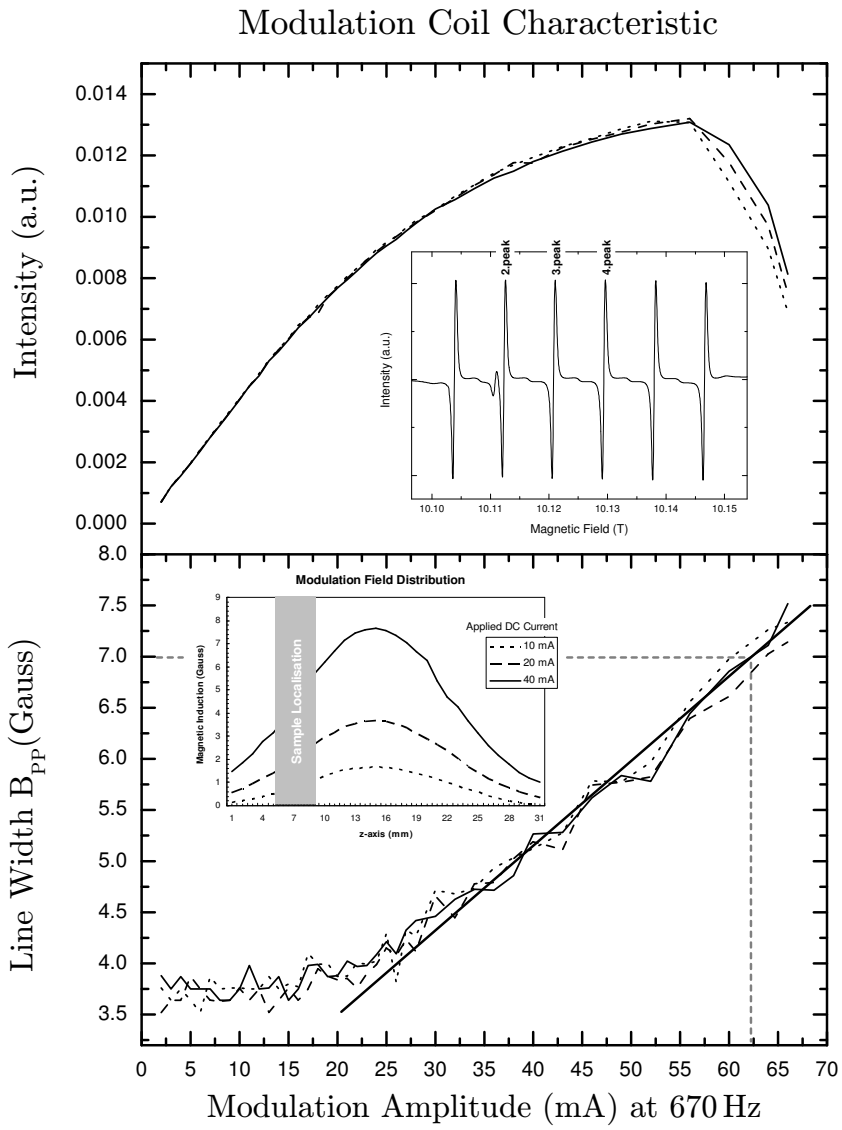


Figure 4.7: The calibration of the modulation coil was performed on a powdered sample containing $Mn^{2+}$ ($S = 5/2, I = 5/2$). For the calibration linewidths of the 2., 3. and 4. peak of the spectra were used (above inset). The powdered sample was spread on the curved mirror and attached by vacuum grease (Apiezon®).

of 10 mm. The modulation coil is centered and attached by three screws to the flange of the corrugated taper to ensure the optical alignment (Fig. 4.4). A maximal modulation field of about 8 G (for a 70 mA current at 0.7 kHz) on the sample can be reached with our power supply (Fig. 4.7).

As the oscillating field can cause vibration of the metallic parts of the resonator (microphonics), it would be preferable to physically separate the modulation coil from the resonator, but this was not possible in our case due to the lack of space available in the cryostat (Fig. 4.4). Nevertheless, the metallic parts of the FP resonator were reduced only to the mirrors and the piezoelectric nanopositioner.

## 4.5 Sample Loading

The practical loading of samples is a crucial issue in the use of resonators. Therefore, we tried to make this loading as easy as possible, see Fig. 4.4. The sample is placed on the spherical (bottom) mirror which is attached to the piston. In this way, the sample can be easily prepared outside the resonator, e.g. under the microscope. The mirror with the piston is afterwards gently slipped onto the piezoelectric nanopositioner and covered by a housing with the mesh on the top. This whole set is then screwed to the corrugated waveguide with the modulation coil. There are two pins which make the holding of the unit straightforward during this assembly, see Fig. 4.5. The whole system is designed to be well aligned along the propagation axis.

## 4.6 Conclusion

The FP resonator described above can be used over the whole frequency set (Table 3.1). However, the main aim to build a FP resonator was to upgrade the multi-frequency cw HF-EPR spectrometer to a pulsed HF-EPR spectrometer operating at 283.2 GHz. The measured finesse $F_{exp}$ at 283.2 GHz can reach values up to $\sim 400$ depending on the mode considered and on the sample (Figs. 3.6, 4.8 and 4.9). This is a good result as the theoretical value is about $\approx$1800. The obtained finesse indicated that the FP resonator can be successively used for the planned pulsed EPR.

To the best of our knowledge, all FP resonators used until now in EPR experiments were mechanically tuned. Taking advantage of the piezoelectric nanopositioner ANPz50 (Attocube systems AG) and implementing it in our FP resonator, allows flexible and very precise tuning of the FP resonator over all modes of interest. The knowledge gained during the work on the FP resonator construction was also used for the construction of the rotating holder for orientation studies of single crystals (Fig. 4.10). In Chapter 3 and in Ref. [68], the performance of both systems is presented (see Figs. 3.6, 3.7 and 3.8).

The FP resonator was designed using previous works on the matter. Among others, the theory of the Fabry - Pérot Resonator was inspired by works of H. Kogelnik *et al.* and G. D. Boyd *et al.* [58, 59, 60]. Different constructions and types of FP resonators can be found in Refs. [8, 9, 12, 13, 21, 23, 27, 28, 45, 48, 54, 55, 66, 69, 70], An overview of inductive meshes can be found in works of L. C. Botten *et al.* [73] and R. Ulrich [72] where the theory together with the measurements of the mesh reflectance and transmittance as a function of wavelengths are discussed. L. C. Botten also considers the effects of the

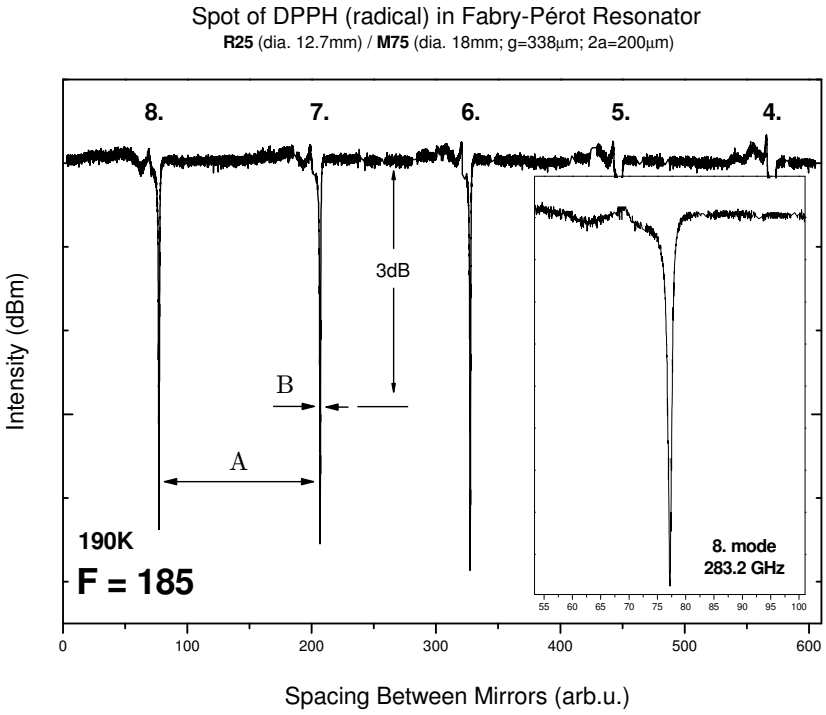


Figure 4.8: Resonance fringes observed at 283.2 GHz and 190 K in the FP resonator filled by powdered DPPH sample in form of spot in the center of the mirror. This particular configuration (R=50 mm, Table 4.3; 75 lines/inch, Table 4.4) of the FP resonator gives a finesse $F$=185, which is calculated from free spectral range (A) and full width at half of the maxima (FWHM) (B) by using Eq. (2.20). Similar value of finesse was found for grain of graphite as well.

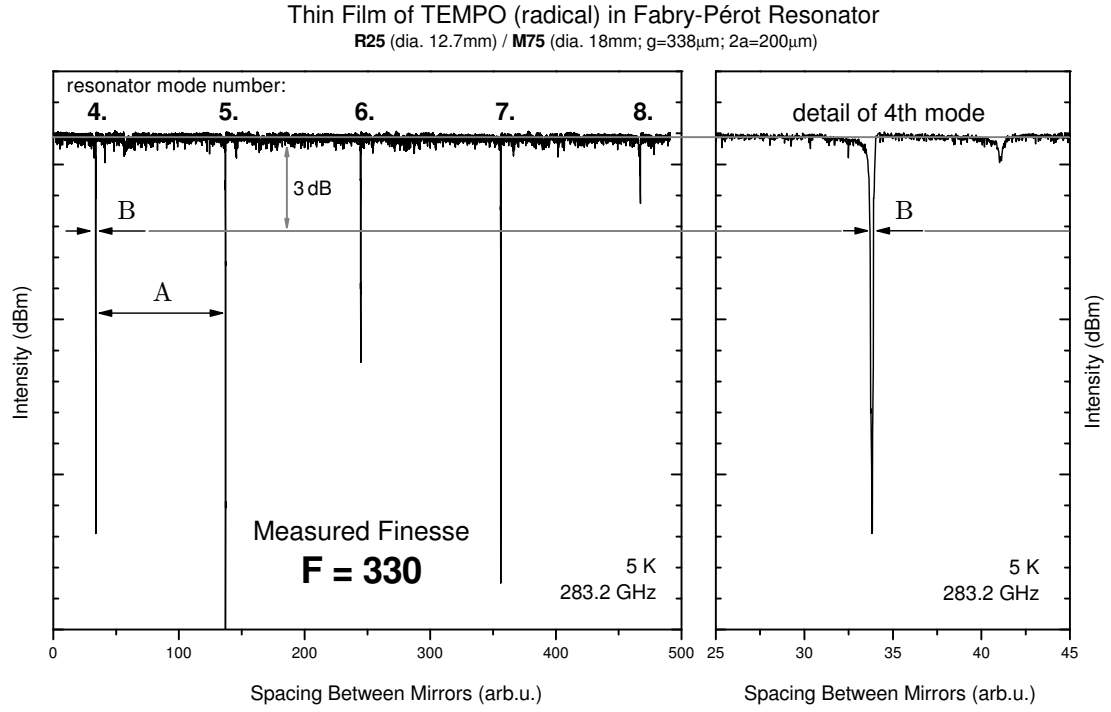


Figure 4.9: Resonance fringes observed at 283.2 GHz and 5 K in the FP resonator. The curved mirror was whole covered by a thin film of TEMPO diluted in polystyrene. This configuration of the FP resonator (R=50 mm, Table 4.3; 75 lines/inch, Table 4.4) gives a finesse $F$=330. For detail of the lowest $4^{th}$ mode see right part of the figure.

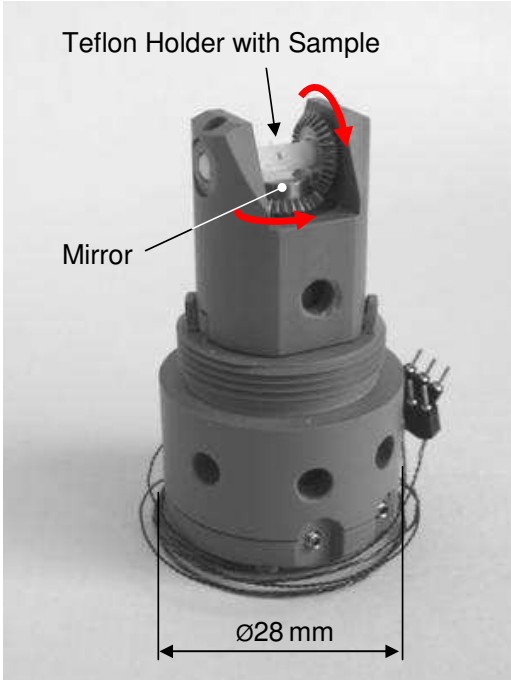


Figure 4.10: Photograph of the rotating holder used for orientation studies of single crystals. The system relies on a rotating piezoelectric nanopositioner ANRv50 (Attocube systems AG) with a resistive encoder allowing an absolute measurement of the angle, hidden in the Torlon housing. The calibrated encoder enables the direct measurement of the position in the range $0° - 337°$ with position reliability of less than $1°$, due to the used mechanical gear.

mesh parameters on the transmission properties. Miscellaneous data of various materials suitable for millimetre and submillimetre optics are collected by J. W. Lamb in Ref. [67].

## Résumé Chapitre 5

# Molécules-Aimants de Tétrafer(III)

Il est maintenant établi que la RPE-HF est l'une des méthodes les plus performantes pour mesurer précisément l'anisotropie magnétique des Molécules-Aimants (Single Molecule Magnets, SMMs) [40, 41].

**Introduction sur les Molécules-Aimants (SMM):** Les SMM possèdent un état de spin fondamental élevé $S$, résultat des interactions d'échange entre les centres magnétiques présents dans la molécule. Comme les SMM possèdent aussi un axe de facile aimantation, leur état de spin fondamental $S$ est décrit par un paramètre axial de l'écart d'énergie en champ nul (Zero-Field Splitting, ZFS) négatif, $D < 0$. A l'intérieur du multiplet fondamental, les niveaux $M_S = \pm S$ sont donc les plus bas en énergie et le niveau $M_S = 0$ est le plus élevé, la différence d'énergie étant de $\Delta \approx DS^2$. (Fig. 5.1). Si $\Delta$ est assez important, l'aimantation du système peut être maintenue longtemps (il est possible de stocker de l'information). Le premier exemple de SMM a été le complexe $Mn_{12}Ac$ [77]. Pour des applications telles que le stockage d'information, le calcul quantique [78, 79, 80] ou la spintronique moléculaire [81, 82], il faut d'abord pouvoir déposer les molécules sur des substrats adaptés. Il a été montré que les dérivés de $Fe_4$ (Fig. 5.3) gardaient leurs propriétés de SMM quand elles étaient greffées sur une surface. L'état de spin fondamental des SMM est en général décrit dans le cadre du Hamiltonien de spin géant [83, 84]. Pour les complexes de tétrafer(III), on va donc traiter un hamiltonien de spin $S = 5$.

**RPE- HF et SMM:** La grande anisotropie des SMM rend ces complexes inaccessibles pour les spectromètres de RPE classique fonctionnant à basse fréquence (bande X, $0.3\,cm^{-1}$), soit parce qu'ils sont complètement silencieux soit parce que seuls des spectres très incomplets sont obtenus. La RPE-HF permettra d'accéder aux paramètres de ZFS par une étude soit sur poudre microcristalline soit sur monocristal.

**RPE- HF Molécules-Aimants deTétrafer(III):** L'étude RPE-HF présentée ici concerne 4 dérivés de $Fe_4$ nouvellement synthétisés. Comme les complexes de $Fe_4$ déjà étudiés [85, 86, 87, 88, 89, 90], ils possèdent une structure de type hélice pour le noyau des fers avec un ion Fe(III) central couplé antiferromagnétiquement aux trois ions externes Fe(III) ce qui conduit à un état de spin $S = 5$ (Fig. 5.3). Ces dérivés, synthétisés dans le groupe du Prof. A. Cornia, diffèrent seulement par les substituants utilisés pour les ligands tripodes, ce qui affecte la structure en hélice.

**Etudes sur poudres:** Les spectres RPE-HF de poudre pour les échantillons **1**-**4** ont été obtenu avec le spectromètre dans sa configuration de transmission à passage unique (configuration la plus simple). Les spectres RPE-HF ont été enregistrés à 190 et 230 GHz pour trois températures. Dans la Fig. 5.8, sont présentés les spectres de poudre expérimentaux ainsi que leur simulations pour l'échantillon **2** à 230 GHz.

**Corrélations Magnétostructurales:** Les études réalisées sur des dérivés de $Fe_4$ précédemment synthétisés ont permis de monter l'existence d'une corrélation entre l'anisotropie magnétique axiale et la structure en hélice de ces complexes [85]. Cette nouvelle étude permet de confirmer la validité de cette corrélation pour les 4 nouveaux composés [90].

**Etude sur monocristal:** L'étude complète d'un monocristal de l'échantillon **2** a été réalisée pour obtenir une meilleure définition de son anisotropie magnétique (Fig. 5.14), en particulier pour les termes d'ordre 4de la description de Spin géant. L'étude en fonction de l'orientation dans le plan dur a été réalisée avec le support tournant construit au cours de ce travail (Figs. 3.5c et 4.10). Les paramètres obtenus (échantillon **2**) sont en bon accord avec ceux déduits de l'étude sur poudre avec un gain en précision, voir Table 5.2.

**Conclusion:** Les spectres de poudre microcristalline RPE-HF obtenus pour les échantillons **1**-**4** ont permis d'obtenir les paramètres du second ordre du Hamiltonien de spin ($D$ et $E$) et de donner une évaluation du terme axial d'ordre 4 ($B_4^0$). L'étude réalisée sur monocristal pour l'échantillon 2 a permis d'avoir une estimation plus fiable du terme axial d'ordre 4 $B_4^0$ ainsi que du terme rhombique d'ordre 2 $E$, mais surtout elle a permis de définir la contribution rhombique d'ordre 4, le terme $B_4^3$ qui était resté inaccessible à l'étude sur poudre. Une connaissance précise de l'anisotropie transverse est une étape essentielle pour la compréhension des processus de relaxation dans ces complexes.

# Chapter 5

# Tetrairon(III) Single Molecule Magnets

By the end of the 1980s, molecular magnetism had seen the emergence of a new research area: the study of high nuclearity spin clusters, which are complex molecules containing a large number of spins most often carried by transition metal ions. Among these molecules, the ones possessing a large spin ground state associated with an Ising type anisotropy have been under particular focus [77]. Indeed, the large spin together with a negative Zero-Field Splitting (ZFS) results in the presence of a barrier for the reversal of their magnetisation at low temperatures. The main consequence is a slow relaxation which, below a blocking temperature ($T_B$), leads to a behaviour quite similar to the one of superparamagnets [91]. Due to these properties, they have been named Single Molecule Magnets (SMMs). Especially, in the low temperature regime, they exhibit a hysteresis in their magnetisation curve with a step-like shape, a signature of the presence of Quantum Tunneling of the Magnetisation (QTM) [92, 93].

HF-EPR proved to be one of the most powerful methods to determine precisely the magnetic anisotropy of SMMs [40, 41], as will be shown in the following experiments and analysis. This chapter deals with the study of the magnetic parameters of tetrairon(III) SMMs by means of HF-EPR and the interplay of those magnetic parameters with the structural parameters of the complexes.

## 5.1 Introduction to Single Molecule Magnets (SMMs)

SMMs possess a large spin ground state $S$, resulting in exchange interactions between their magnetic centers. Often, it is possible to stabilize a large spin ground state even when only antiferromagnetic interactions are present, due to the competition between all the interaction pathways resulting from the structure of the molecule. As SMMs have an easy-axis magnetisation, their spin ground state $S$ is split by a negative axial ZFS term, $D$. Thus, inside the ground multiplet, the levels $M_S = \pm S$ are the lowest in energy and the level $M_S = 0$ is the highest, the energy difference being $\Delta \approx DS^2$. (Fig. 5.1): there is an energy barrier $\Delta$ for the reversal of the magnetisation. At low temperature, when only the ground spin state is thermally populated, the relaxation time of the magnetisation increases when the temperature decreases due to the presence of the barrier. In a first temperature regime, this relaxation will involve phonons (multiple Orbach process), whereas at the lowest temperatures relaxation will take place through quantum tunnelling of the lowest $M_S$ levels (Fig. 5.2) and will be temperature independent.

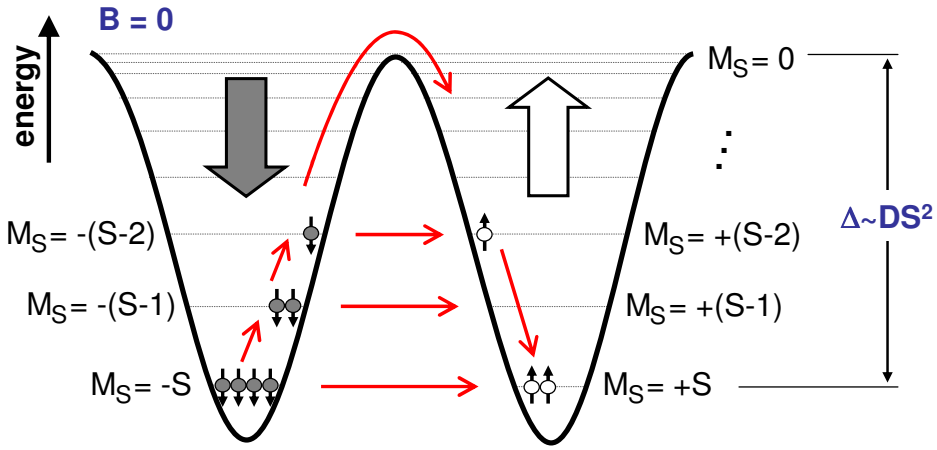


Figure 5.1: A SMM of a total spin $S$ with the Ising (easy-axis) type anisotropy at a finite temperature and at zero external magnetic field ($B = 0$), after a magnetisation into $-S$ state (gray arrow). The SMM can relax from the $-S$ polarised state (overcome the potential barrier $\Delta \approx DS^2$) either by QTM, multiple Orbach process or by combination of both as shows the figure.

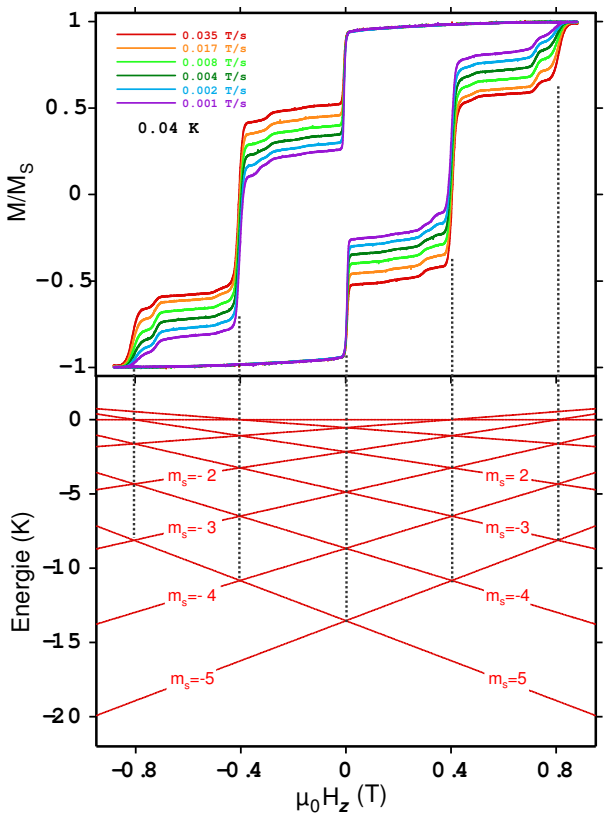


Figure 5.2: Magnetisation hysteresis curve of SMM with $S$=5 measured by micro-SQUIDs [94]. The steps in the magnetisation curve are typical features of SMM behaviour. The steps observed in the hysteresis loop correspond to increase in the rate of the magnetisation change when there is an energy coincidence between levels on both sides of the potential barrier (Fig. 5.1) which can be seen in the corresponding Zeeman diagram bellow. Picture reprinted with a kind permission of W. Wernsdorfer.

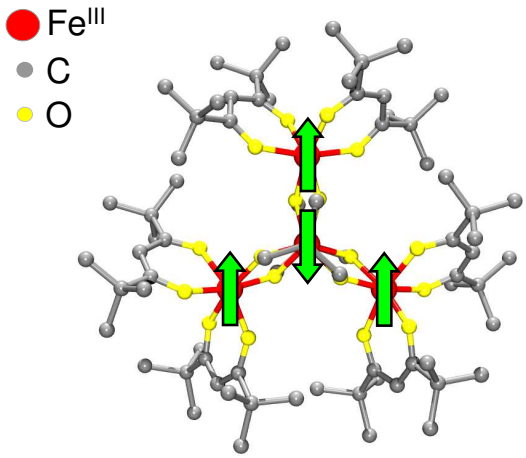


Figure 5.3: Molecular structure of tetra-iron(III) molecule. The four iron(III) are arranged in centered-triangular fashion and are connected by three bridging ligands which create a propeller-like structure. The four high spin iron(III) with $S = 5/2$ are antiferromagnetically coupled via middle ion into total spin $S = 5$.

In between, the dominant relaxation mechanism will involve phonon assisted QTM. The step-like shape of the magnetic hysteresis curve is the signature of a relaxation involving QTM: the steps in the magnetisation curve appear when tunnelling is made possible by energy levels degeneracy (Fig. 5.2).

If $\Delta$ is sufficiently high the magnetisation can be preserved for a long time. Therefore, it is in principle possible to store information in such a molecule. The first complex identified to behave as a SMM was the $Mn_{12}Ac$ complex [77], of formula [95]:

$$[Mn_{12}O_{12}(O_2CCH_3)_{16}(H_2O)_4]\cdot 4H_2O\cdot 2CH_3CO_2H.$$

Despite being the first SMM discovered, it was only recently that it lost the record of the highest temperature for which magnetic hysteresis is observed. This means that despite the enormous synthetic effort made during twenty years to increase the magnetic energy barrier $\Delta$, it has only been possible to do it recently and for a unique complex $Mn_6$ [96, 97]

$$[Mn_6O_2(Et\text{-}sao)_6(O_2CPh(Me)_2)_2(EtOH)_6].$$

Besides the increase of the magnetic anisotropy barrier $\Delta$, another important trend in SMM research nowadays is dealing with examining SMM behaviour when the complexes are organised on solid surfaces or anchored to them. Indeed, for applications such as information storage, quantum computing [78, 79, 80] or molecular spintronics [81, 82] it is necessary to find a way to deposit molecules on suitable substrates with these molecules maintaining their properties when deposited on the surface. $Mn_{12}Ac$ and its derivatives turned out to lose their SMM properties when isolated on surfaces [98], thus inciting the search for different complexes. Conversely, $Fe_4$ derivatives have been shown to maintain their SMM properties when grafted on a surface [99]. As a result, several functionalized derivatives have been synthesized and precisely characterized.

$Fe_4$ SMMs, also called ferric stars, present a propeller-like structure for the core of the molecule (Fig. 5.3). A central iron(III) ion ($s = 5/2$) is antiferromagnetically coupled by alkoxo bridges to three external iron(III) ions, stabilizing an $S = 5$ ground spin state. Whereas the first complex synthesized involved six methoxo bridges, the new derivatives present a more rigid structure induced by the use of tripodal ligands $H_3L = R\text{-}C(CH_2OH)_3$. The proper choice of the R substituent allows grafting on solid surfaces like gold, silicon

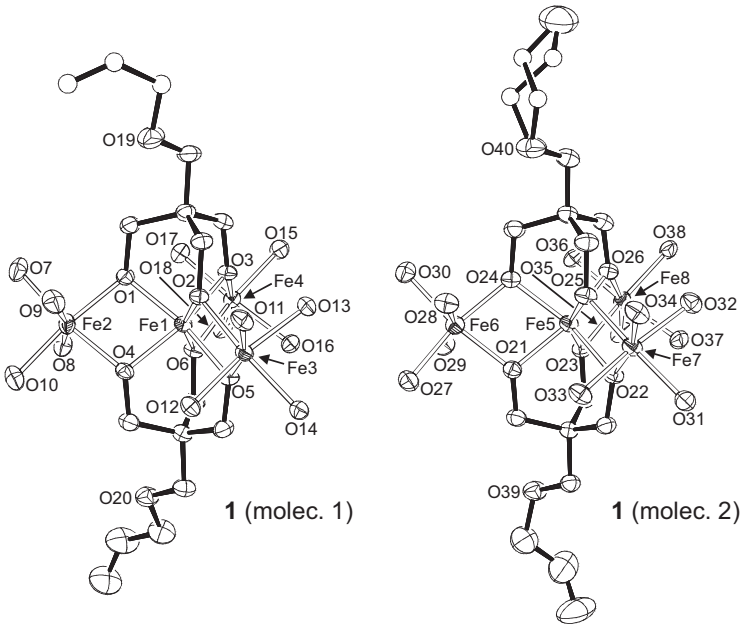


Figure 5.4: ORTEP of the two crystallographically-independent molecules in crystal **1** (Λ isomers). One alkyl chain in molecule 2 is distorted over two aproximately equally populated positions. Thermal ellipsoids are drawn at 50% probability. All hydrogen and carbon atoms of $dpm^-$ ligands have been omitted for clarity. The $dpm^-$ is the anion of dipivaloymethane. Picture taken from Ref. [90] and reprinted with kind permission of A. Cornia.

and more recently carbon nanotubes [86, 99, 100, 101, 89, 102]. The study of SMMs from the Fe4 family using HF-EPR spectroscopy will be treated in the following sections.

### 5.1.1 Spin Hamiltonian $\mathcal{H}$

For SMMs, the ground spin state is usually described in the frame of the Giant Spin Hamiltonian. This description is in principle valid in the strong exchange limit, which is not always the case. Indeed, the first excited spin states have been found quite close in energy to the top of the ground spin multiplet (for instance, in the case of $Mn_{12}Ac$, INS measurements have shown that the lowest $M_S$ levels of the first $S = 9$ excited state are only $2\,cm^{-1}$ higher than the highest $M_S$ level of the ground $S = 10$ state). However, the introduction of higher order terms (than second order $D$ and $E$ terms) in the description of the ZFS allows obtaining a more reliable description of the system, even if the strong exchange condition is not completely met. Here we will interpret the EPR spectra of our complexes with the Giant Spin Hamiltonian. Up to second order for the ZFS, the classical EPR Hamiltonian is obtained:

$$\mathcal{H} = \mathcal{H}_Z + \mathcal{H}_{LF} = \mu_B \mathbf{S} \cdot \mathbf{g} \cdot \mathbf{B} + D[\mathbf{S}_z^2 - \frac{1}{3}S(S+1)] + E(\mathbf{S}_x^2 - \mathbf{S}_y^2), \qquad (5.1)$$

where $\mu_B \mathbf{S} \cdot \mathbf{g} \cdot \mathbf{B}$ is the Zeeman Hamiltonian $\mathcal{H}_Z$ associated with the external magnetic field $\mathbf{B}$, and $D[\mathbf{S}_z^2 - \frac{1}{3}S(S+1)] + E(\mathbf{S}_x^2 - \mathbf{S}_y^2)$ is the ligand field Hamiltonian which describes the magnetic anisotropy (ZFS) of the system at second order. $\mathbf{S}_x$, $\mathbf{S}_y$, $\mathbf{S}_z$ are the three components of the spin operator $\mathbf{S}$.

The D and E terms are the axial and rhombic anisotropy parameters of the system. They are related by $-1/3 \leq E/D \leq +1/3$. When the ratio $|E/D| = 1/3$ the system is totally rhombic, whereas $E = 0$ when the system is axially symmetric. $D$ can be either negative or positive, corresponding to an easy-axis or an easy-plane anisotropy respectively. The ligand field Hamiltonian $\mathcal{H}_{LF}$, written above, is the simplest approximation for the

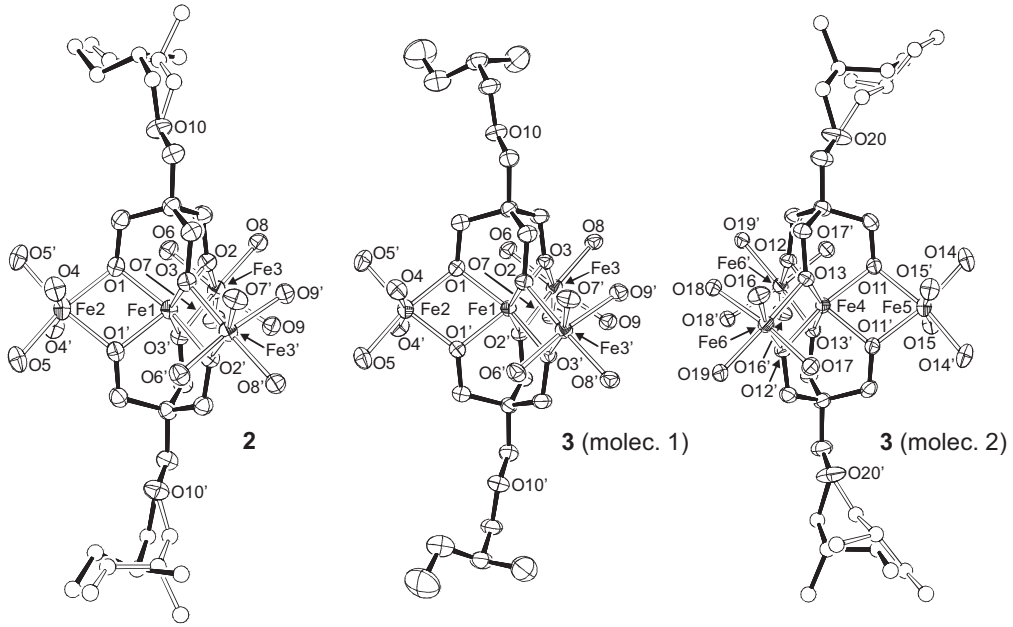


Figure 5.5: Left: ORTEP of crystal **2** ($\Lambda$ isomers), with bound tripodal ligands in $S$ form (solid bonds) and $R$ form (open bonds). Right: ORTEP plot of the two crystallographically-independent molecules in crystal **3** ($\Lambda$ and $\Delta$ isomers). All hydrogen and carbon atoms of $dpm^-$ ligands have been omitted for clarity. The $dpm^-$ is the anion of dipivaloymethane. Picture taken from Ref. [90] and reprinted with a kind permission of A. Cornia.

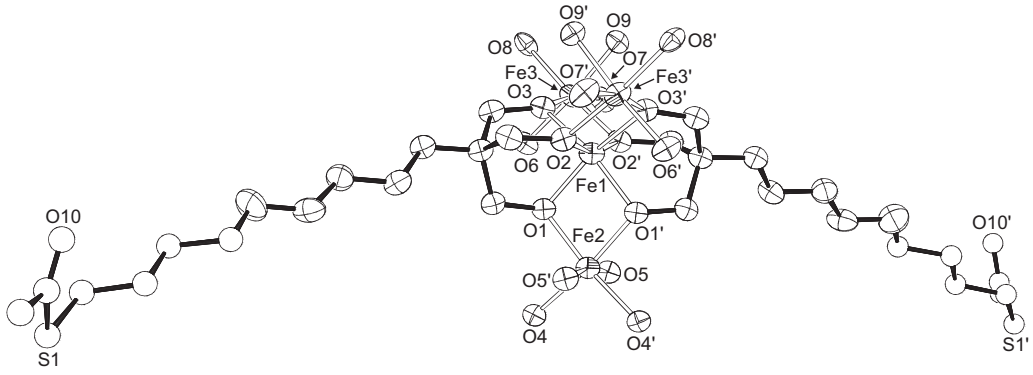


Figure 5.6: ORTEP of crystal **4** ($\Lambda$ isomers) with thermal ellipsoids drawn at 30% probability. All hydrogen and carbon atoms of $dpm^-$ ligands have been omitted for clarity. Only one component of the disordered SAc-terminated alkyl chain is shown. This molecule as first showed magnetic hysteresis at gold surface [86]. Picture taken from Ref. [90] and reprinted with a kind permission of A. Cornia.

magnetic anisotropy of the system. Dealing with large spin values $S$, higher order terms are expected, in principle up to $2S$ order. Whereas the parameters associated with these higher order terms are rarely measurable on mononuclear complexes (for instance on Mn(III) complexes with $S = 2$), they are easier to extract for large spin systems as they are amplified by $\sim S^k$ for the transitions issued from the levels with larger $|M_S|$ values. The complete Hamiltonian is then:

$$\mathcal{H} = \mathcal{H}_Z + \mathcal{H}_{LF} = \mu_B \mathbf{S} \cdot \mathbf{g} \cdot \mathbf{B} + D[\mathbf{S}_z^2 - \frac{1}{3}S(S+1)] + E(\mathbf{S}_x^2 - \mathbf{S}_y^2) + \sum_{k,q} B_k^q \mathcal{O}_k^q, \quad (5.2)$$

where $\mathcal{O}_k^q$ are Stevens operators and the $B_k^q$ are the corresponding parameters [83, 84]. The symmetry of the complex defines the $B_k^q$ different from zero, similarly to what happens for $D$ and $E$. For $Fe_4$ SMMs, only fourth order terms will be considered in addition to second order terms.

## 5.2 HF-EPR and SMMs

HF-EPR proved to be one of the most powerful methods to determine precisely the magnetic anisotropy of SMMs [40, 41]. Here, we highlight some of the most important features of HF-EPR for the study of SMMs, before moving to the particular case of tetrairon(III) molecules. Due to the large anisotropy of SMMs, these complexes are inaccessible to classical EPR spectrometers operating at low frequencies (X-band, $0.3\,cm^{-1}$), either being EPR silent or giving rise to very incomplete spectra. Going to higher frequencies to overcome the energy gaps of the ground spin multiplet is necessary, also because SMMs have integer spin values [77, 103]. To give an (extreme) example, the splitting between the lowest occupied states $M_S = -10$ and $M_S = -9$ in the $Mn_{12}Ac$ is $\sim 10\,cm^{-1}$ (300 GHz); hence EPR spectrometers operating at low frequencies cannot probe this transition. The first HF-EPR spectra of the $Mn_{12}Ac$ were reported in Refs. [77, 104]. Furthermore, HF-EPR spectra of SMMs are usually easy to analyze, as the ZFS terms are small with respect to the Zeeman one. Thus mostly only the so-called permitted transitions are observed and the ZFS values can be estimated at first sight. Another simplification results from the high spin polarisation obtained at liquid helium temperature in HF-EPR: when measuring a powder the contributions coming from different principle axes ($x$, $y$ and $z$) are well separated, the easy-axis ones being at low field (with respect to the centre of the spectrum) whereas the hard-plane ones are found at high field (Fig. 5.7). The ZFS parameters can be obtained from HF-EPR either on polycrystalline (powdered) or single crystal samples. The powdered samples are pressed into pellets in order to avoid orientation effects. The powder spectrum has to be recorded first as it gives a unique indication on the position of the extremes of the spectra. The knowledge of the extremes is the basis to determine the proper single crystal orientations corresponding to the easy ($z$) and hard ($x$) axes, the intermediate principal axis ($y$) being perpendicular to the other two. A complete study, performed on a polycrystalline powder and on single crystals, allows a precise determination of the ZFS parameters, often up to higher order terms, and the principal axes of the magnetic anisotropy as well.

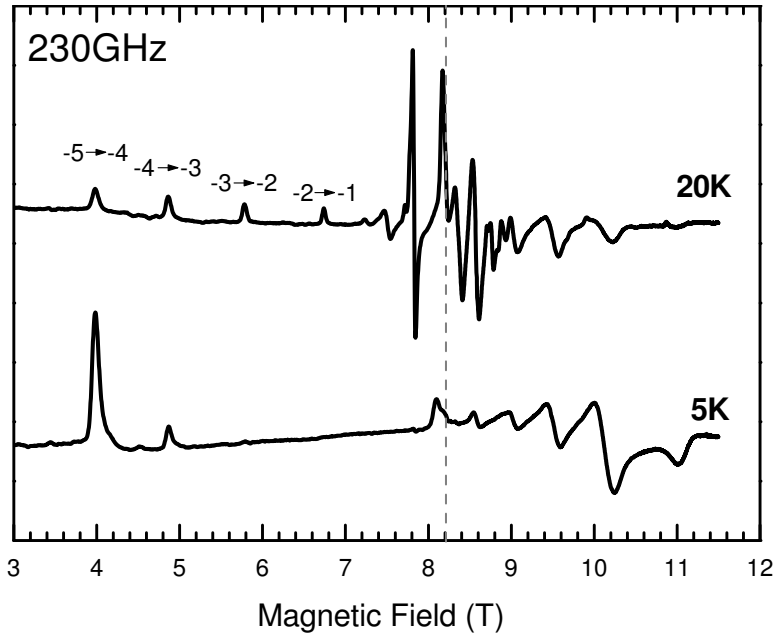


Figure 5.7: In the plot, pattern of four well resolved parallel transitions $M_S \rightarrow M_S + 1$ for the sample **2** are shown. The vertical dashed lines in the graph indicate the central resonance field at 8.21 T (230 GHz) and splits the spectra to parallel (bellow) and perpendicular (above) regions.

## 5.3 HF-EPR of Tetrairon(III) Single Molecule Magnets

The HF-EPR presented here deals with recently synthesized $Fe_4$ derivatives. Like the previously synthesized $Fe_4$ complexes [85, 86, 87, 88, 89, 90], they present a propeller-like structure for the iron core with a central iron(III) ion antiferromagnetically coupled to the three external iron(III) ions resulting in an $S = 5$ ground state. These derivatives from the group of Prof. A. Cornia, have the formula $[Fe_4(L)_2(dpm)_6]$ where H$dpm$=2,2,6,6-tetramethyl-heptan-3,5-dione and $H_3L$=R'-O-$CH_2C(CH_2OH)_3$ with R'=alkyl (sample **1**; R'=$(R,S)$-2-methyl-1-butyl (sample **2**) and R'=$(S)$-2-methyl-1-butyl (sample **3**). Sample **4** is a new crystal phase of the previously synthesized complex containing $H_3L$=11-(acetylthio)-2,2-bis(hydroximethyl)undecan-1-ol. The crystalographic structures of the molecules are depicted in Figs. 5.4, 5.5 and 5.6 for sample **1**, **2**, **3** and **4**, respectively. The molecules differ only in the substituents on the tripodal ligands used, which affect the propeller-like structure. The rigid tripodal ligands keep the Fe-O core in nearly perfect $D_3$ symmetry, with one threefold axis ($C_3$) perpendicular to the tetrairon plane and three twofold axes ($C_2$) which go through the central iron ion to each one of the three peripheral metal ions, see Fig. 5.10. All compounds are 1:1 mixture of $\Lambda$ and $\Delta$ propeller isomers (right- and left-hand helicity). The compounds **1-4** crystalize within monoclinic lattice in $P2_1/c$, $P2/n$, $P2$ and $C2/c$ space groups, respectively. Complete crystallographic data can be found in Ref. [90].

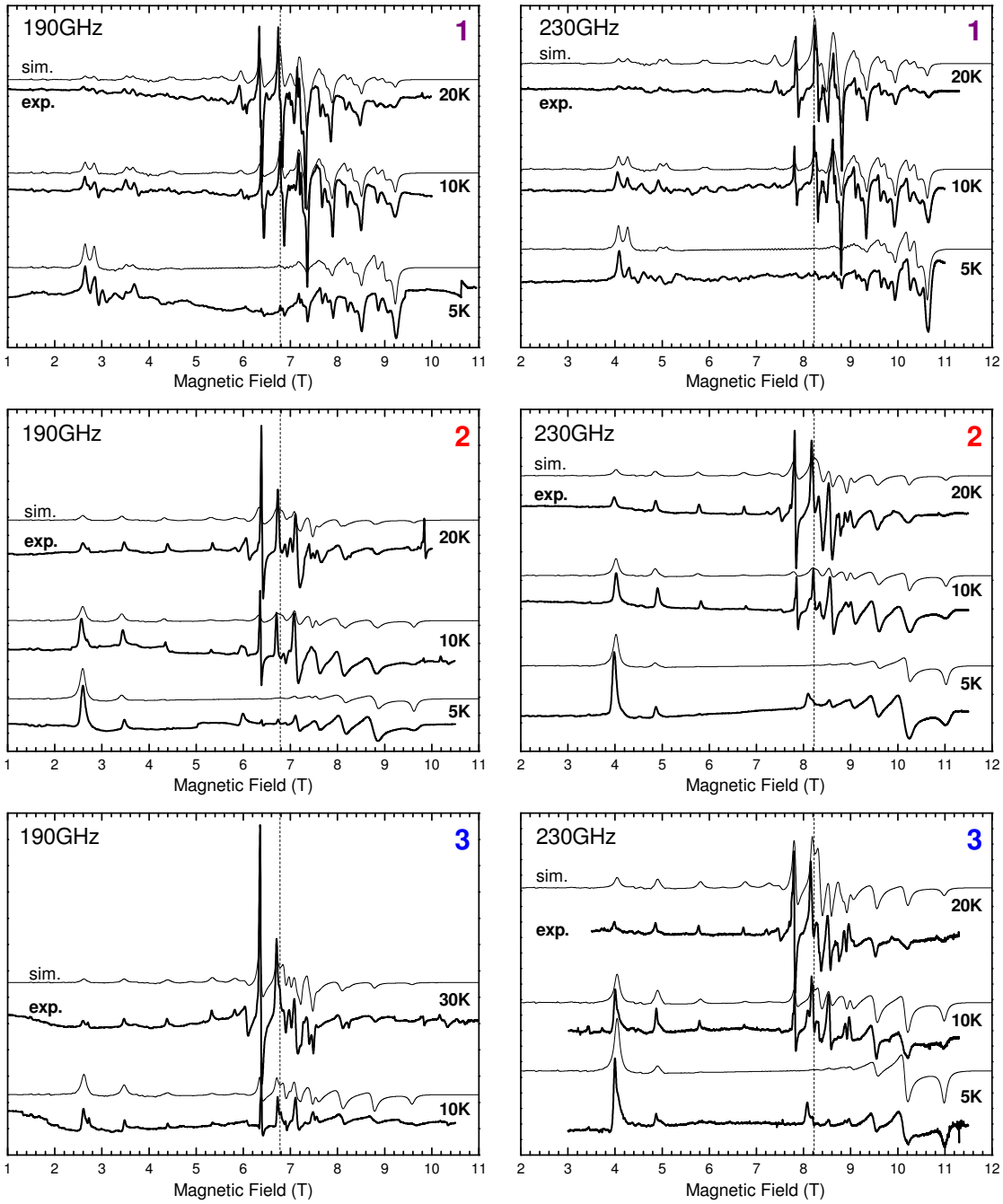


Figure 5.8: Experimental HF-EPR spectra of powdered samples **1-3** taken at 190 and 230 GHz at several temperatures (bold lines) superimposed by simulated spectra (narrow line). The parameters used for simulation are given in Table 5.1. The vertical dashed lines in the graphs indicate the central resonance field at 8.21 T (230 GHz) and 6.79 T (190 GHz) and splits the spectra to parallel (bellow) and perpendicular (above) regions.

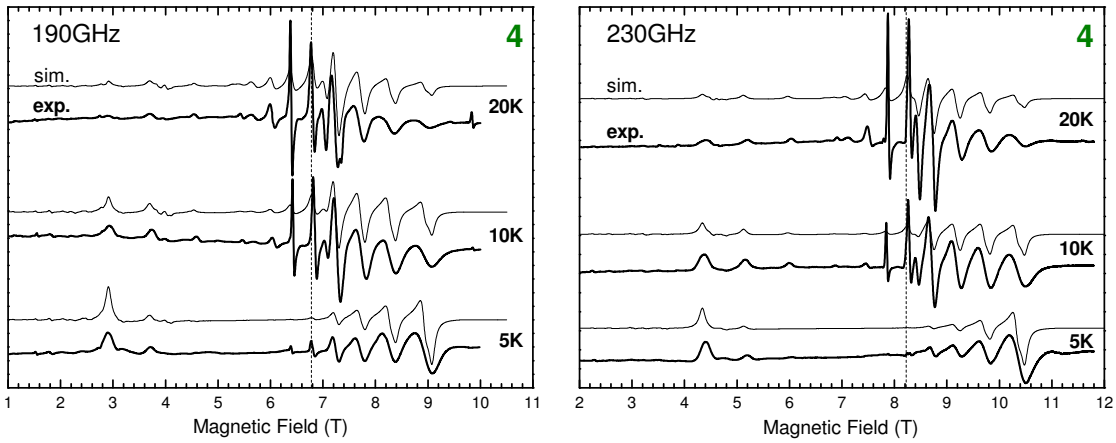


Figure 5.9: Experimental HF-EPR spectra of the powdered sample **4** taken at 190 and 230 GHz at three temperatures (bold lines) superimposed by simulated spectra (narrow line). The parameters used for simulation are given in Table 5.1. The vertical dashed lines in the graphs indicate the central resonance field at 8.21 T (230 GHz) and 6.79 T (190 GHz).

### 5.3.1 Powdered Samples

HF-EPR spectra of powdered samples **1**-**4** were obtained with the HF-EPR spectrometer in single-transmission configuration, already mentioned in Chapter 3. The samples in form of polycrystalline powders were pressed into pellets in order to avoid orientation effects. The HF-EPR spectra were recorded for 190 and 230 GHz excitation frequencies and at three temperatures 5, 10 and 20 K except for sample **3** where the 190 GHz spectra were recorded at 10 and 30 K only, see Figs. 5.8 and 5.9.

For the sake of simplicity we will first discuss the experimental spectrum obtained for the sample **2** at 230 GHz and 5 K (Fig. 5.7). At this temperature, the features belonging to the principal directions are well separated. One group is visible at low field with respect to the $g = 2$ (8.2 T), whereas the other group is found at higher field. The lowest field is the farthest from the $g = 2$ among all the signals. This is the signature that the low field transitions corresponds to the magnetic field applied parallel to the easy-axis of the molecule. Conversely, the signal in the high field part of the spectrum corresponds to the magnetic field in the hard-plane. At 5 K, the most intense signals are found at the extremes of the spectrum, as only the lowest $M_S$ levels are thermally populated. Increasing the temperature, more signals are visible with an intensity pattern which is a function of the thermal population and of the transition probability. At 20 K, four well resolved parallel transitions $M_S \rightarrow M_S + 1$ are visible in the low field part of the spectrum as labelled in Fig. 5.7. Furthermore, a careful inspection of the spacing of the parallel transitions reveals that the line-to-line separation slightly increases when moving to high magnetic field, thus pointing to presence of terms of order higher than 2. The same analysis applies to the other spectra (other frequency and other samples). However in the spectra of sample **1** an extra splitting for each transition is observed, which can be understood by the presence of two magnetically inequivalent molecules in the sample. Indeed considering two sets of parameters with a 1:1 ratio, the spectra can be well simulated, as discussed in the

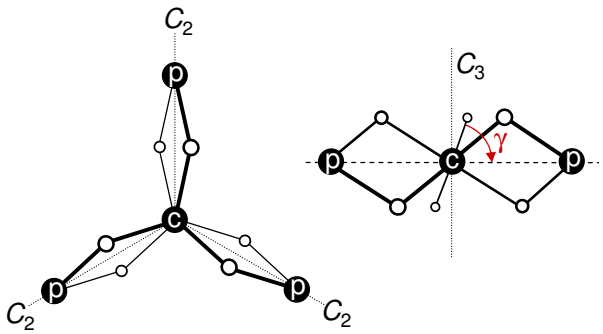


Figure 5.10: Definition of the pitch angle $\gamma$ used in the structural analysis of tetrairon(III) propeller-like complexes, assuming idealized $D_3$ symmetry. The $C_2$ axis lies in the plane defined by the four metal centers (dashed line), one in the center "c" and three on periphery "p" of the crystal. The $C_3$ axis is perpendicular to them and coincides with the easy-axis of the system.

following.

The recorded spectra were simulated by using the following spin Hamiltonian (Eq. (5.1)) where the axial fourth therm is included:

$$\mathcal{H} = \mu_B \vec{S} \cdot g \cdot \vec{B} + D[S_z^2 - \tfrac{1}{3}S(S+1)] + E(S_x^2 - S_y^2) + B_4^0 \mathcal{O}_4^0,$$

with the Stevens operator $\mathcal{O}_4^0$:

$$\mathcal{O}_4^0 = 35S_z^4 - [30S(S+1) - 25]S_z^2 + 3S^2(S+1)^2 - 6S(S+1).$$

The transverse four order term $B_4^3\mathcal{O}_4^3$ is not included as the broadness of the lines in the perpendicular region of the spectra preclude determining it. The $B_4^3$ parameter will be found latter on from a single crystal study. The simulation of the spectra was performed with the program "sim" written by Dr. H. Weihe from the University of Copenhagen. The best-fit parameters obtained by the simulation of the powdered spectra of samples **1-4** are listed in Table 5.1 and the corresponding simulated spectra are plotted in Figs. 5.8 and 5.9. All four samples could be fitted by one set of parameters except sample **1**, where two sets of parameters were needed. Sample **4** has a slightly lower axial anisotropy ($D = -0.412\,\mathrm{cm}^{-1}$) than samples **2** ($D = -0.449\,\mathrm{cm}^{-1}$) and **3** ($D = -0.442\,\mathrm{cm}^{-1}$), in agreement with the position of the lowest field transition ($-5 \longrightarrow -4$). The spectra of sample **1** could be well reproduced considering two species in the cell in agreement with crystallographic data. One species has a large axial anisotropy ($D = -0.435\,\mathrm{cm}^{-1}$) comparable with that of samples **2** and **3** whereas the second species present a smaller axial term ($D = -0.417\,\mathrm{cm}^{-1}$) comparable with the one of sample **4** ($D = -0.412\,\mathrm{cm}^{-1}$).

Table 5.1: The parameters of the spin Hamiltonian for isotropic g-tensor ($g = 2$) obtained by simulation of the HF-EPR spectra of the powdered samples **1-4** (Figs. 5.8 and 5.9).

| | **1** | **2** | **3** | **4** |
|---|---|---|---|---|
| $D$ ($\mathrm{cm}^{-1}$) | -0.417<br>-0.437 | -0.449 | -0.442 | -0.412 |
| $E$ ($\mathrm{cm}^{-1}$) | 0.015<br>0.009 | 0.030 | 0.031 | 0.006 |
| $10^5 B_4^0$ ($\mathrm{cm}^{-1}$) | 1.3<br>0.9 | 2.4 | 1.6 | 1.8 |

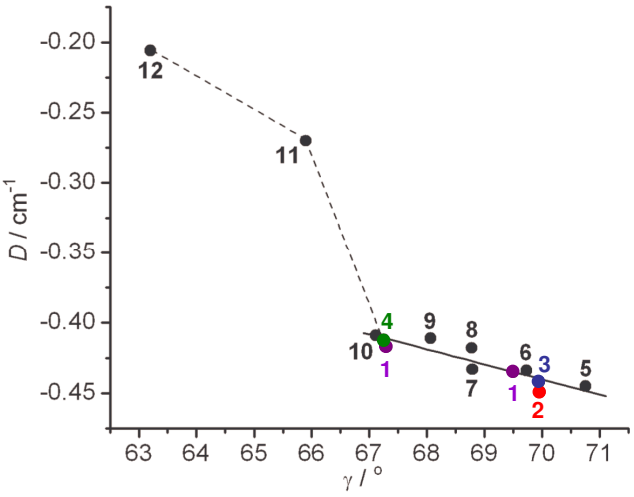


Figure 5.11: Magneto-structural correlation of the $Fe_4$ family. The structural and magnetic data of samples **5**, **8**, **11**, **12** are given in Ref. [85] and of samples **6** [86], 7 [87], **9** [88] **10** [89]. Graph taken from Ref. [90] and reprinted with kind permission of A. Cornia.

X-ray diffraction of sample **1**-**4** shows the presence of two crystallographically inequivalent molecules with also different propeller-pitches $\gamma$ (Fig. 5.10), see Fig. 5.4. This discovery supports the observation of a correlation between the magnetic and structural properties.

### 5.3.2 Magnetostructural Correlations

In previously studied $Fe_4$ derivatives, it has been shown that there exists a correlation between the axial magnetic anisotropy and the propeller structure of the complexes [85]. It allowed establishing that the $D$ term, in absolute value, is increasing when the helical pitch increases. The helical pitch $\gamma$ is the dihedral angle between the plane of the iron ions and the $Fe_cO_2Fe_p$ plane, where $Fe_c$ and $Fe_p$ stands for the central and one peripheral Fe ions; the two O are the ones involved in the alokoxo bridges connecting these iron ions (Fig. 5.10). This new study shows that the correlation still applies to the four new $Fe_4$ derivatives, as show in Fig. 5.11.

The numbers **1**-**4** in the plot correspond to our new derivatives, whereas the samples indexed from **5**-**12** are taken from previous works [85, 86, 87, 88, 89]. Indeed, for the **1**-**10** derivatives, a linear relation between the $D$ value and the pitch angle is found. These derivatives are the ones for which only tripodal ligands are employed, resulting in rather rigid structures for the iron core, which is also reflected in the small change of 4° in the $\gamma$ value over the series. When methoxo ligands are used (**12** in Fig. 5.11) or one tripodal ligand associated to three ethoxo ones (**11** in Fig. 5.11), the same trend is still observed but the linear dependence is not realized.

The origin of this correlation is attributed to the reorientation of the single ion ZFS tensors of the peripheral iron ions which leads to a change of the contribution of the these tensors to the total anisotropy of the ground spin $S = 5$, the reorientation being driven by the change of $\gamma$. In previous studies, not only a correlation for $D$ but also for $B_4^0$ was obtained. Here, the powder study does not allow precise enough $B_4^0$ parameters to be obtained to verify this relation. A single crystal study has thus been performed to increase the precision on $B_4^0$. The details of the magnetostructural correlation are in Ref. [90, 85].

Table 5.2: Comparison of the spin Hamiltonian parameters for isotropic g-tensor ($g = 2$) obtained by simulation of the HF-EPR spectra of the powder spectrum (Fig. 5.8) and fitting of single crystal spectra (Figs. 5.13 and 5.14) of sample **2**.

| | $D$ ($cm^{-1}$) | $E$ ($cm^{-1}$) | $B_4^0$ ($cm^{-1}$) | $B_4^3$ ($cm^{-1}$) |
|---|---|---|---|---|
| powder | -0.449 | 0.030 | $2.4 \cdot 10^{-5}$ | – |
| crystal | -0.4472 | 0.0354 | $1.4 \cdot 10^{-5}$ | $-7.5 \cdot 10^{-4}$ |

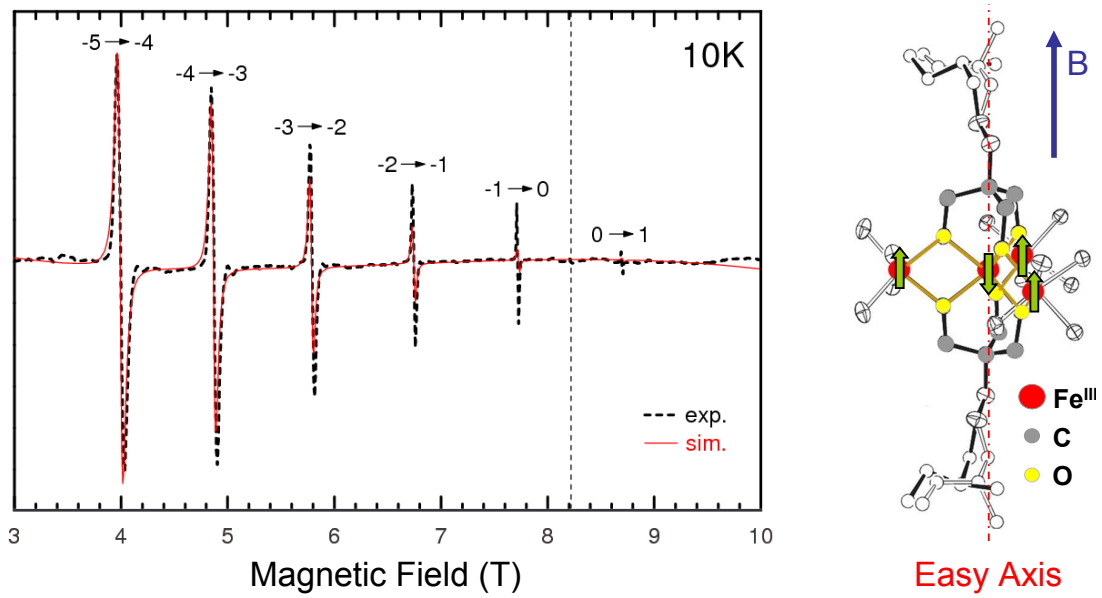


Figure 5.12: HF-EPR spectra of the single crystal of sample **2** with the easy-axis aligned in the direction of the applied magnetic field $B$ (dash line). The red line represent the results of the simulation. The experimental spectrum was simulated with the values $D = -0.4472\,cm^{-1}$, $E = 0.0354\,cm^{-1}$, $B_4^0 = 1.4 \cdot 10^{-5}\,cm^{-1}$ and $B_4^3 = -2.20 \cdot 10^{-3}\,cm^{-1}$ of the spin Hamiltonian found by the simulation of the single crystal study (Fig. 5.14). The paramagnetic transitions $M_S \longrightarrow M_S + 1$ are indicated in the picture and the dashed line indicates the central resonance field (8.21 T). The spectrum was taken with a non-resonant cavity of the HF-EPR spectrometer in QO configuration at 230 GHz and 10 K.

### 5.3.3 Single Crystal Study

Single crystal studies were performed in order to obtain a better knowledge of the magnetic anisotropy of the $Fe_4$ complexes, especially of the higher order terms in the Giant Spin description. In the approximation of $D_3$ symmetry, a complete single crystal study is obtained with the recording of spectra along the easy-axis and for the complete rotation in the hard plane (rotation around $C_3$ axis, see Fig. 5.10). This will allow the transverse fourth order term $B_4^3$ to be obtained and increase the precision on $B_4^0$ as well.

For a single crystal study sample **2** has been chosen due to its originality among the series (together with sample **3**). It has a high $E/D$ ratio as well as a small effective energy barrier $\Delta$ notwithstanding its large $D$ value. The study of this sample is also a first step for comparison with sample **3**, with the aim to explain the origin of the two measured relaxation times in sample **3**. Also sample **2** exhibits very clean powder spectra. The orientation study in the hard plane was performed with the newly developed rotating holder (Fig. 3.5c and 4.10). First, the single crystal was oriented on a Teflon holder using the indexing of the faces found by X-ray diffraction. The magnetic field $B$ was applied parallel to the easy-axis of sample **2**, on a trial and error basis, until the resulting spectrum reproduced the low field signals of the powder spectrum. The spectrum along the easy-axis at 230 GHz and 10 K is shown in Fig. 5.12. Then the Teflon holder with the correctly oriented sample was rotated by 90° and inserted into the rotating holder (Fig. 4.10), ensuring that the magnetic field $B$ was lying in the hard anisotropy plane. The uncertainty on the orientation was less than 1°. Spectra were recorded in this plane over $\sim 340°$, in steps of 6.74° at 230 GHz and 10 K (see Fig. 5.13, where spectra obtained over $\sim 200°$ are displayed).

If we first look on the easy-axis spectra (Fig. 5.12) the spacing between the transitions ($M_S \longrightarrow M_S + 1$) at lower magnetic fields is smaller than the spacing between transitions located at higher fields. This confirms our previous conclusion that the $D$ and $B_4^0$ terms have opposite sign. Now looking at the spectra obtained by the rotation of the single crystal in the hard-plane (Fig. 5.13 and Fig. 5.14) the presence of these transverse terms is obvious. The effect of the transverse terms is most pronounced on transition $-5 \rightarrow -4$, where the position of the line during rotation goes, almost over 1 T, from 10.10 T to 11.05 T. Going towards lower fields, the transverse terms have lower and lower effect on the line position up to the $0 \rightarrow 1$ transition. The $0 \rightarrow 1$ transition appears nearly at constant magnetic field but a small reverse tendency of the line position with respect to the previous lines can be seen, which is then clearly visible on the transition $1 \rightarrow 2$ (Fig. 5.14).

In contrast to the powder spectra discussed in the previous paragraph, these spectra were fitted (and not simulated) to the spin Hamiltonian:

$$\mathcal{H} = \mu_B \vec{S} \cdot g \cdot \vec{B} + D[S_z^2 - \tfrac{1}{3}S(S+1)] + E(S_x^2 - S_y^2) + B_4^0 \mathcal{O}_4^0 + B_4^3 \mathcal{O}_4^3,$$

with the corresponding Stevens operator:

$$\mathcal{O}_4^3 = \tfrac{1}{4}S_z(S_+^3 + S_-^3) + \tfrac{1}{4}(S_+^3 + S_-^3)S_z.$$

A transverse fourth order term $B_4^3$ is added as the single crystal spectra allow a much better precision than the powdered spectra on the behaviour in the hard-plane.

The best-fit of experimental data was found for the values: $D = -0.4472\,\mathrm{cm}^{-1}$, $E = 0.0354\,\mathrm{cm}^{-1}$, $B_4^0 = 1.4 \cdot 10^{-5}\,\mathrm{cm}^{-1}$ and $B_4^3 = -2.20 \cdot 10^{-3}\,\mathrm{cm}^{-1}$ using the "FFIT program"

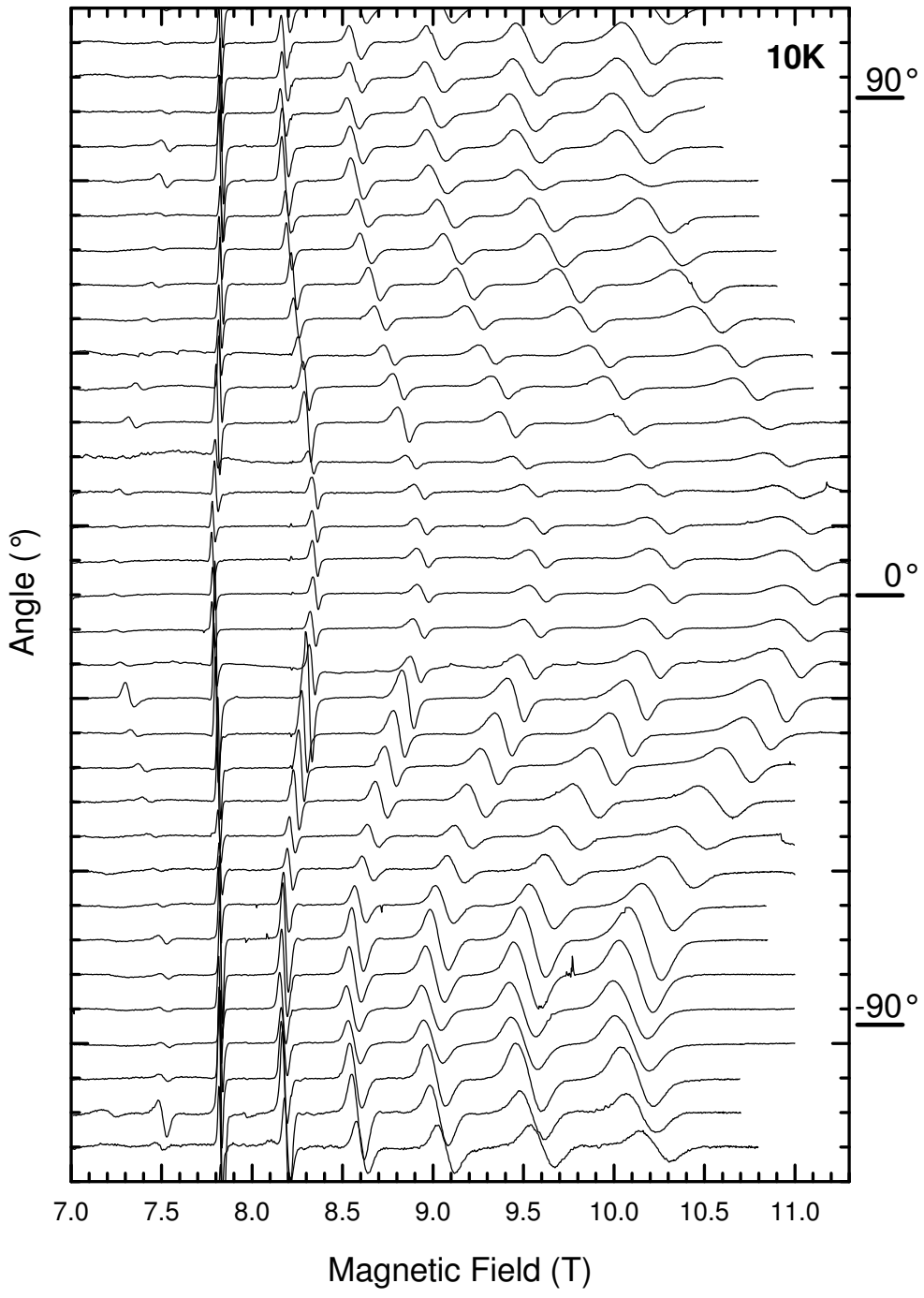


Figure 5.13: HF-EPR spectra of a single crystal of sample **2** at 230 GHz and 10 K. The crystal in the rotating sample holder was rotated around its easy-axis (Fig. 5.12) in steps of 6.74°.

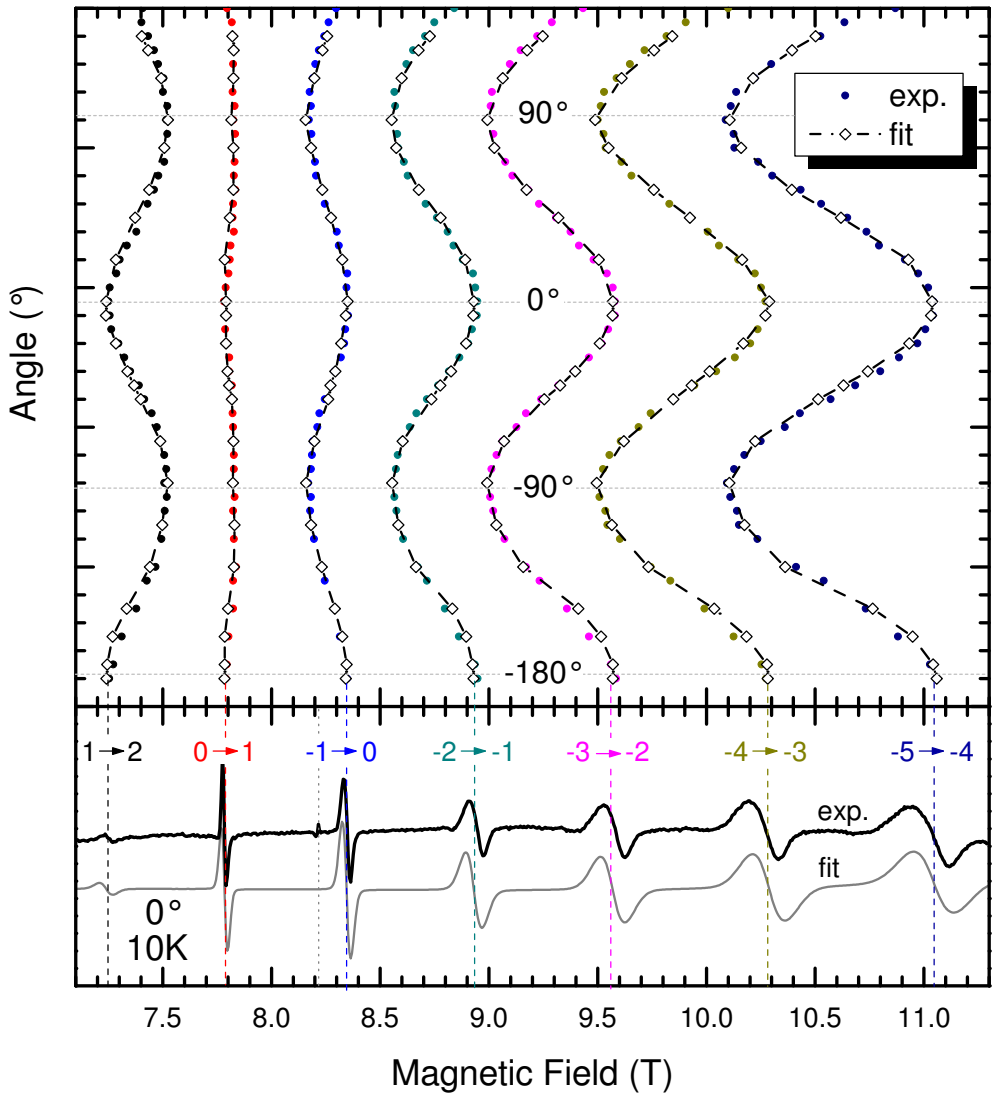


Figure 5.14: Dots, angular dependence of paramagnetic transitions of single crystal of sample **2** (Fig. 5.13). Diamonds, fit of the experimental data at selected positions. The best-fit of the experimental data was obtained for values: $D = -0.4472\,\mathrm{cm}^{-1}$, $E = 0.0354\,\mathrm{cm}^{-1}$, $B_4^0 = 1.4 \cdot 10^{-5}\,\mathrm{cm}^{-1}$ and $B_4^3 = -7.5 \cdot 10^{-4}\,\mathrm{cm}^{-1}$ of the spin Hamiltonian. Bellow, the experimental data with the fit for the spectrum taken at 0°.

written by Dr. H. Weihe. The parameters found are in good agreement with those found previously by the simulation of the powdered sample **2**, see Table 5.2. On the easy-axis, the values obtained from the single crystal study are very close to the ones determined from the powder study. The larger change concerns the $B_4^0$ term which had a large uncertainty, as a value in the range $10^{-5}\,\mathrm{cm}^{-1}$ hardly affects the lowest field line in the powder spectrum (the $S = 5$ spins does not amplify the effect of this term very much); thus any error on the $D$ value will result in large variation on $B_4^0$. Conversely, the second order transverse term $E$ is changing substantially (by more than 10%) probably because of the new and rather large $B_4^3$ term (one order of magnitude larger than $B_4^0$).

As could be seen in Fig. 5.11, complex **2** has an axial anisotropy very similar to that of the previously studied complex **5** [85], leading to similar energy barriers $\Delta$. However, alternating current susceptibility measurements result in quite different effective energy barriers $\Delta_{\mathrm{effective}}$ of 13 K for **2** and 17 K for **5**. This means that efficient relaxation processes (tunneling) are present. The large values found for $E$ and $B_4^3$ could be an explanation for this phenomenon.

## 5.4 Conclusion

The measured HF-EPR spectra of powdered samples **1**-**4** has enabled the extraction of the second order parameters of the spin Hamiltonian ($D$ and $E$) and gave an evaluation of the axial fourth order terms ($B_4^0$ and $B_4^3$). The single crystal spectra obtained on sample **2** gave a more reliable estimation of the fourth order axial term $B_4^0$, and also allowed a better determination of the transverse anisotropy at second order ($E$) and especially at fourth order as the $B_4^3$ term was unknown before this study. The determination of the transverse anisotropy is important with a view to understanding the relaxation processes in the complex.

# Résumé Chapitre 6

## Graphène

La structure du graphène (cristal 2D) était supposée instable jusqu'à ce qu'il soit observé/fabriqué dans le groupe du Prof. A. K. Geim [105] à l'Université de Manchester en 2004 [106, 107, 108].

**Structures cristalline et de Bande:** Le graphène est constitué d'une monocouche plane d'atomes de carbone, liés les uns aux autres par trois liaisons covalentes $sp^2$ dans une structure d'anneau benzénique (réseau en nid d'abeille) (Fig. 6.1). La liaison $p$ restante orientée perpendiculairement au plan du graphène conduit à l'apparition de bandes $\pi$ avec une structure de bande inhabituelle [109, 110, 111]. Dans le graphène, les bandes de conduction et de valence se rejoignent (touchent) en deux points non équivalents K et K' (points de Dirac, DP) dans l'espace des moments. Autour de ces points, la dispersion des particules devient pratiquement linéaire, formant un cône de Dirac. Le mouvement des électrons est mieux décrit par l'équation de Dirac (Weyl) pour des fermions sans masse que par l'équation conventionnelle de Schrödinger [110, 111]. Ce comportement de particule sans masse (fermions de Dirac) résulte de la structure de bande linéaire. La linéarité des bandes crée un lien direct entre le graphène et l'électrodynamique quantique, permettant d'étudier des effets purement relativistes tels que le paradoxe de Klein ou le Zitterbewegung [112, 113].

**Niveaux de Landau du Graphène:** La dynamique des électrons à l'intérieur d'un même cristal relève habituellement de la mécanique quantique non-relativiste. Mais cette approche ne peut s'appliquer dans le cas du graphène avec des électrons sans masse qui se déplacent à vitesse constante proche de celle de la lumière $\tilde{c}$. Quand le mouvement de ces fermions de Dirac est quantifié en niveaux de Landau (Landau levels, LL) par l'application d'un champ magnétique externe, ces niveaux varient, de façon inhabituelle, comme $\sqrt{B}$ au lieu de la classique dépendance linéaire vis-à-vis de $B$, Fig. 6.3.

**Spectroscopie des Niveaux de Landau / Résonance Cyclotron:** Dans le graphène, une masse effective peut être attribuée aux fermions de Dirac via la fameuse relation d'Einstein $m = E/\tilde{c}^2$. Un champ magnétique appliqué perpendiculairement au plan du graphène réarrange la densité d'états des particules de continûment linéaire en niveaux de Landau presque discrets, voir Fig. 6.3 La position des Résonances Cyclotron (CR) ne dépend alors que d'un seul paramètre du matériau, la vitesse de Fermi du graphène $\tilde{c}$. La séparation des niveaux de Landau du graphène est non-équidistante du fait de l'extrême non-parabolicité (linearité) des bandes (Fig. 6.3). L'interaction de fermions sans masse avec la lumière est habituellement exprimée par une conductivité dynamique (optique) [114].

**Spectroscopie des Niveaux de Landau du Graphène à la Surface du Graphite Massif:** Récemment, la présence de lamelles de graphène bien définies a été mise en évidence, sous la forme de feuillets découplés du graphite massif [115]. Dans ce travail, nous présentons la réponse de ces lamelles lors d'expériences de magnéto-absorption MW et montrons que leurs états électroniques de type Dirac sont quantifiés en niveaux de Landau jusqu'à des champs magnétiques aussi bas qu'1 mT et à des températures élevées jusqu'à 50 K (Fig. 6.7). Les signaux simulés de la Fig. 6.9 ont été obtenus avec $\gamma = 35\,\mu$eV pour l'élargissement des raies, une vitesse de Fermi $\tilde{c} = 1.00 \times 10^6\,\mathrm{m.s^{-1}}$ et un niveau de Fermi $E_F = 6.5\,$meV.

La résonance cyclotron a été mesurée avec le spectromètre RPE-HF, décrit au Chapitre 3, en configuration de cavité à double passage (non-résonante) ainsi qu'avec le résonateur FP (Fig. 3.5).

**Conclusion:** Nous avons ainsi montré qu'un état très pur du graphène peut être trouvé à l'état naturel à la surface du graphite massif, sous la forme de lamelles découplées du matériau substrat. En testant ces lamelles par spectroscopie des niveaux de Landau dans le domaine sub-THz à très bas champ magnétique, la qualité électronique supérieure de ces feuillets de très faible densité ($n_0 \sim 3 \times 10^9\,\mathrm{cm^{-2}}$), exprimée par une mobilité des porteurs supérieure à $10^7\,\mathrm{cm^2/(V.s)}$, a été démontrée. Ce résultat représente un challenge pour améliorer les technologies actuellede fabrication du graphène.

# Chapter 6

# Graphene

Carbon appears in many allotropic forms including anisotropic graphite and isotropic diamond (3D), graphene (2D), as well as carbon nanotubes (1D) or fullerenes (0D). Concerning 2D crystals in general, it was presumed that such structures cannot be stable due to thermal fluctuations, which at any temperature lead to their disintegration, i.e. to the creation of small islands or curved structures such as fullerenes or nanotubes when carbon based systems are considered. Nevertheless, graphene was first fabricated by the group of Prof. A. K. Geim [105] at Manchester University in 2004 in a form of a single sheet supported by $Si/SiO_2$ substrate, and later on, in 2008, even as a self-standing membrane, having diameter up to a few hundred microns [106, 107, 108]. Today, after five years of intensive research, the physics of graphene is relatively well established and the understanding of its electronic, optical, as well as mechanical properties is fast progressing.

The main interest in graphene is definitely induced by its unique electronic band structure which is linear in the vicinity of the Fermi level. This peculiar band structure allows us to study phenomena connected with quantum electrodynamics by means of standard methods used in the solid-state physics. Simultaneously, graphene is a promising material from the viewpoint of possible applications, mainly in future carbon-based electronics. To sum up, graphene is one of the most heavily investigated systems studied in the current condensed matter physics.

## 6.1 Crystal and Band Structure

Graphene is a planar monolayer of carbon atoms, which are mutually bound via three covalent bonds ($sp^2$) into a benzene-ring structure (honeycomb lattice) (Fig. 6.1). The hexagonal symmetry of the graphene crystal lattice implies a unit cell with two inequivalent (A and B) atoms, effectively forming two triangular sublattices, see Fig. 6.1. Whereas the three hybrids $sp^2$ bonds in the plane of graphene are responsible for the exceptional stiffness of graphene, the remaining $p$ bond oriented perpendicular to the graphene plane leads to creation of $\pi$ bands with an unusual band structure discussed in the following paragraphs.

The band structure of graphene was first calculated using the tight-binding approximation by P. R. Wallace in 1947 [109], but experimentally confirmed only recently [110, 111]. Wallace used graphene as a natural starting point for further calculations of the graphite band structure. The pioneering work of Wallace on graphite was soon followed

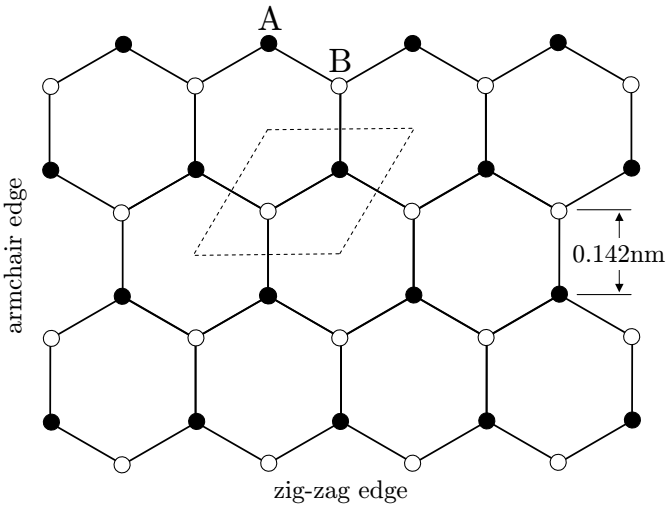


Figure 6.1: Crystallographic structure of graphene consists of two carbon sublattice A (•) and B (○) forming honeycomb lattice. Dashed lines show a unit cell.

by J. C. Slonczewski, P. R. Weiss and J. W. McClure, who all further developed his model, using similar approach (SWM model) [116, 117].

In graphene, the conduction and valence bands meet (touch) at two inequivalent K and K' Dirac points (DP) in momentum space around which the particle dispersion becomes nearly linear, forming thus the so-called Dirac cone (Fig. 6.2). The electron motion is rather described by the Dirac (Weyl) equation for massless fermions than the conventional Schrödinger equation [110, 111]. In undoped graphene, the Fermi level is placed exactly at the Dirac point which makes graphene a zero-gap semiconductor. Due to the unique linear band structure, electrons behave as massless particles, often referred to as massless Dirac fermions, similar to neutrinos or photons (but having non-zero electronic charge), but with an effective velocity of light (Fermi velocity $\tilde{c}$) about $10^6$ m/s, which is about 300× smaller than the speed of light in vacuum. The linearity of bands creates a direct link between graphene and quantum electrodynamics and allows us to study purely relativistic effects such as the Klein paradox[1] or Zitterbewegung[2] [112, 113].

## 6.2 Fabrication of Graphene

Graphene can be prepared in several ways and new types of preparation are still emerging. Graphene was first fabricated in the group of Prof. A. K. Geim in 2004 [105] by an amazingly simple method, by the micromechanical cleavage (exfoliation) of bulk graphite, which is nothing else than a repeated peeling of bulk graphite with a common Scotch tape. This technique can provide us with high quality graphene specimens having the lateral dimension up to 100 $\mu$m. The finding of the one-atom-thick material itself is another tricky point in its fabrication process. Placing graphene on a silicon substrate covered with a $SiO_2$ layer, having an accurately chosen thickness (300 nm in most cases), individual flakes are visible in white light using a standard optical microscope. This way peeled few-layer

[1] Klein paradox is observed on Dirac fermions, telling that relativistic electron has always unit probability to penetrate any protectional barrier, irrespective of the hight and width of the barrier.

[2] Zitterbewegung: Jittery motion of massless Dirac fermions related to uncertainty principle (energy-position) of these particles.

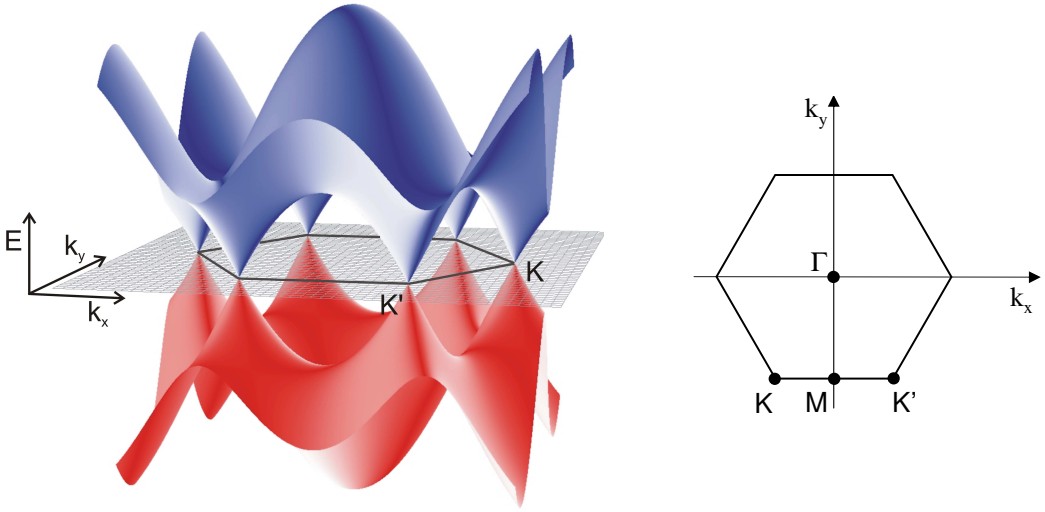


Figure 6.2: Band structure of graphene. The conductance (blue) and valence (red) band touch at K and K' (Dirac) points in momentum space around which the dispersion is linear, creating so-called Dirac cones. Picture reprinted with a kind permission of M. Orlita.

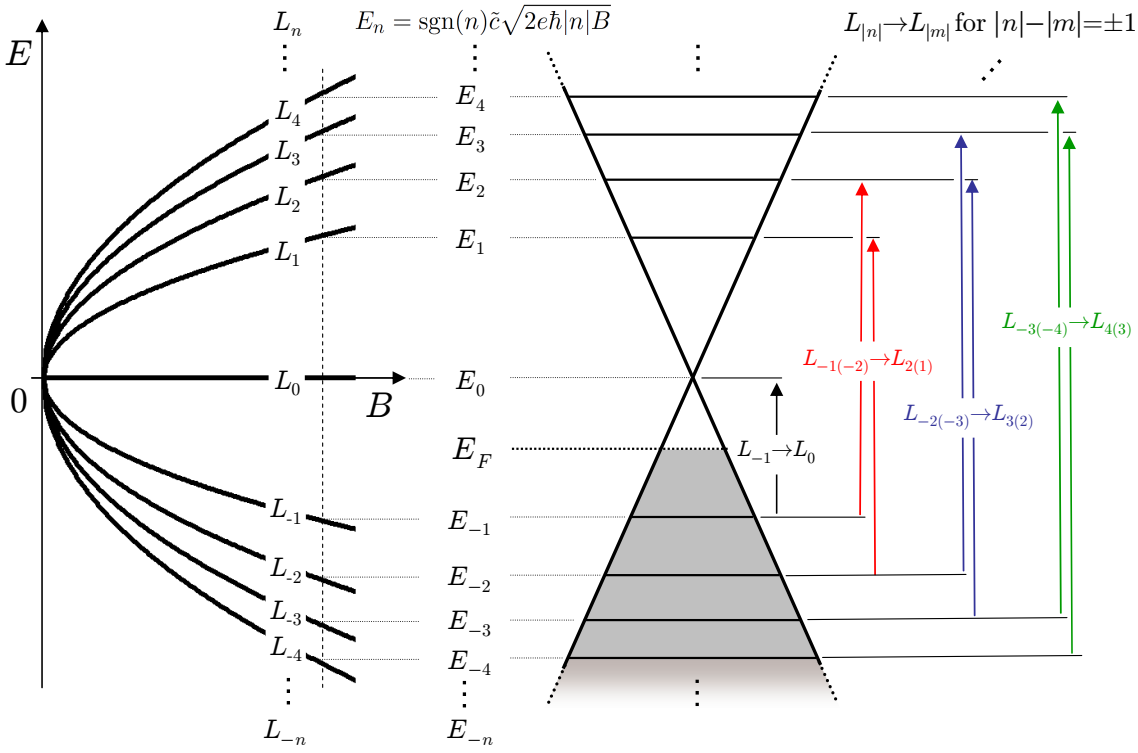


Figure 6.3: **Left:** Schematic evolution of LLs $L_n$ in graphene with applied magnetic field $B$. **Right:** Optically allowed transitions in $p$-doped graphene for given magnetic field $B$. $n$ and $m$ denote indexes of a LLs.

flakes of graphene having various number of layers can be relatively easily identified [107]. This "Schotch tape" peeling technique has a limitation in the size of resulting graphene sheets, which rarely exceeds $5000\,\mu\mathrm{m}^2$(www.grapheneindusties.com). Nevertheless, flakes of this size are largely sufficient for many fundamental experiments.

Significant effort is put in other techniques which could permit production of graphene having larger area. This research on grahene is driven mainly by its possible applications. Nowadays, the epitaxial growth of graphene via thermal annealing of SiC crystal [118, 119, 120] is one of the most promising ways. In this respect, multi-layer graphene prepared on carbon-terminated surface of SiC are of especial interest, where individual sheets are electrically decoupled due to an unusual rotational stacking [121] and have thus properties nearly equivalent to a graphene monolayer. Anyway, the presence of several layers in the epitaxial graphene makes this material more complex compared to exfoliated graphene.

Large graphene specimens can also be prepared by chemical decomposition on metallic surfaces, e.g. on ruthenium or nickel [122, 123, 124]. This technique enables fabrication of large (single-layer) graphene flakes. Their transfer to an arbitrary substrate has been recently demonstrated [125, 126].

Graphene can be also found on the surface of bulk graphite, as a floating sheet electrically decoupled from its bulk support. Such graphene sheets have already been investigated by STM[3] spectroscopy [115]. Magneto-optical measurements on these layers carried out in the THz spectral range [127] are discussed in the following parts of this thesis.

## 6.3 Landau Levels in Graphene

The dynamics of electrons inside a common crystal are usually described by non-relativistic quantum mechanics. A particle is often considered as free with an effective mass $m^*$, and its dispersion relation (approximatively) reads:

$$E = \hbar^2 k^2 / 2m^*. \tag{6.1}$$

When the magnetic field $B$ is applied (here we consider only 2D systems), the free motion of the particle is quantized into circular orbitals having degenerate energies, so-called Landau levels (LLs):

$$E_n = \hbar\omega_c \left(n + 1/2\right), \quad \text{for } n = 0, 1, 2, ..., \tag{6.2}$$

where $\omega_c$ is the cyclotron energy ($\omega_c = eB/m$).

This well-known approach models fails in graphene where electrons are massless with a constant velocity $\tilde{c}$:

$$E = \tilde{c}\hbar k. \tag{6.3}$$

When the motion of a Dirac fermions in this system are quantized by the external magnetic field, we obtain a distinctively different (quasi-)discrete energy spectrum:

$$E_n = \mathrm{sgn}(n)\tilde{c}\sqrt{2e\hbar|n|B}, \quad \text{for } n = ..., -2, -1, 0, 1, 2, ..., \tag{6.4}$$

where $e$ the electron charge and $n$ the LL index. Levels with $n < 0$ ($n > 0$) correspond to hole (electron) states, respectively, and the magnetic-field-independent zero level $n = 0$ is

[3] Scaning Tunnelling Microscopy - STM

shared by both electrons and holes. Untypically, the LLs in graphene evolves as $\sqrt{B}$ [128] instead of a well-known linear in $B$ dependence derived in the previous case, Fig. 6.3.

The existence of the zero-energy LL results in appearance of so-called "half-integer" quantum Hall effect (QHE) [110, 111], which has been observed even at room temperature [129]. This surprising finding is connected with a relatively weak electron-phonon coupling (virtually vanishing at temperatures equal or lower than the room temperature) and mainly with the large energy spacing between Landau levels $E_1 - E_0 = 37\sqrt{B[\mathrm{T}]}\,\mathrm{meV}$, which at high magnetic fields significantly exceeds the energy of thermal excitations at room temperature ($k_bT \approx 25\,\mathrm{meV}$). This interesting insensitivity of graphene to temperature has been confirmed also in magneto-optical experiments on multilayer epitaxial graphene Fig. 6.5 [130].

## 6.4 Landau Level Spectroscopy / Cyclotron Resonance

Compared to standard magneto-transport measurements, where electrical contacts are essential, spectroscopic techniques carried out in the magnetic field represent their non-invasive alternative. LL spectroscopy directly probes (see Fig. 6.3) the energy spectrum in certain range of energies, whereas the magneto-transport measurements are sensitive to the close vicinity of the Fermi level. In the following paragraphs, we will focus on our results of the LL spectroscopy of graphene performed via magneto-absorption measurements in the far infrared (FIR) as well as in the THz range, using either Fourier-transform or HF-EPR techniques. Let us note that LLs in graphene-based materials have recently been observed in several STS experiments (scanning tunnelling spectroscopy), which is another useful way how to visualize them [115, 131, 132].

The massless character of Dirac fermions in graphene calls for magneto-optical measurements, namely cyclotron resonance (CR) experiments. CR experiments in common materials (with parabolic dispersion) are used to determine the effective mass of the charge carriers (electrons and holes). In graphene, an effective mass can be applied to the massless Dirac fermions attributed via the famous Einstein relation $m = E/\tilde{c}^2$. The applied magnetic field perpendicular to the plane of graphene rearranges the continuous linear DOS of particles into quasi-discrete LLs, see Eq. (6.4). The position of CRs are then defined by a single material parameter, the Fermi velocity in graphene $\tilde{c}$. The LLs in graphene are non-equidistantly spaced due to extreme non-parabolicity (linearity) of the bands (Fig. 6.3) the position of CRs then has a square-root dependence on the applied field $B$, Fig. 6.4, which is a hallmark of the presence of Dirac fermions.

The CR measurements have been performed on multilayered epitaxial graphene prepared by annealing of SiC [130, 128] (see Fig. 6.4 and 6.5), on a single flake of exfoliated graphene [133] and nowadays on decoupled graphene sheets found on the surface of bulk graphite as well [127]. The CR on decoupled graphene sheets is discussed in the next, experimental, part.

Interaction of massless fermions with the light is usually expressed by dynamical (optical) conductivity [114]. To reproduce the experimental data, we assume the absorption strength is proportional to the longitudinal conductivity $\sigma_{xx}$ of the system within the Kubo formalism with allowed transitions $L_n \to L_m$ for $|n| \pm |m| = 1$:

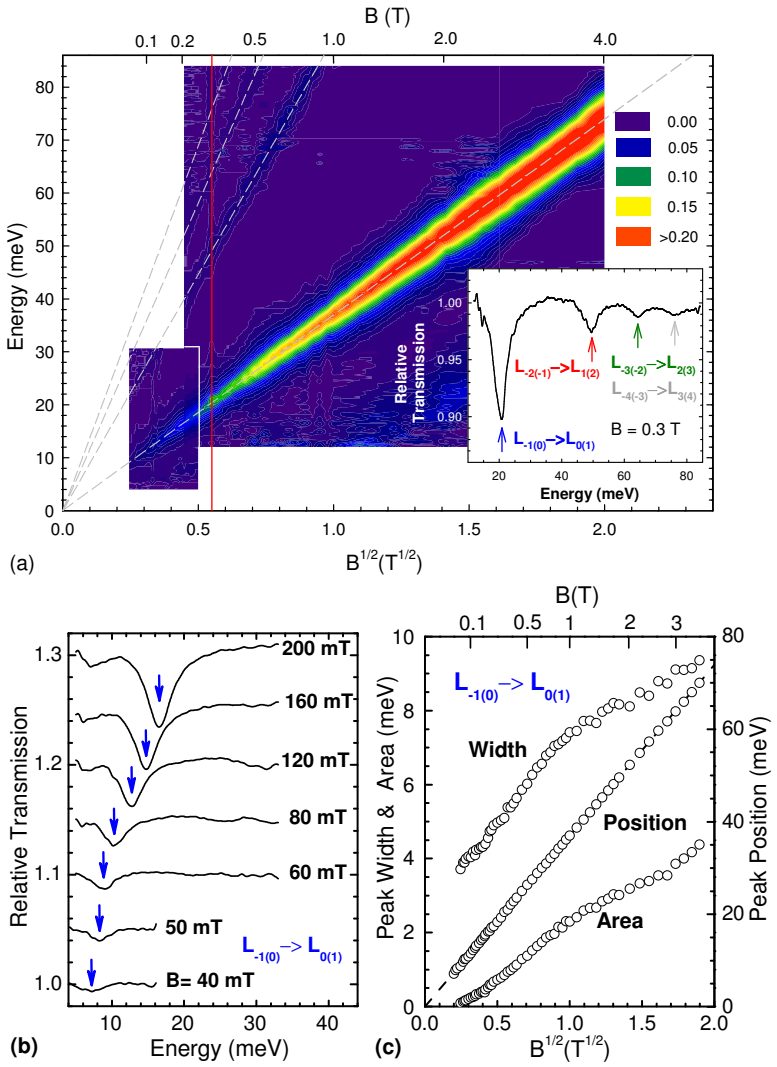


Figure 6.4: Part (a): The FIR transmission $\mathcal{T}$ plotted as $-\ln\mathcal{T}$ as a function of the magnetic field at $T = 2.0$ K. The dashed lines denote the expected transitions for $\tilde{c} = 1.02 \times 10^6$ m.s$^{-1}$. The inset shows the transmission spectrum at $B = 0.3$ T. Part (b): FIR transmission taken at $T = 2$ K in low magnetic fields. Successive spectra are shifted vertically by 0.05. The part (c) shows the peak position, width and area for the $L_{-1(0)} \rightarrow L_{0(1)}$ transition. The dashed line in part (c) is a least squares fit to the peak positions. The measurement was performed on multilayered epitaxial graphene on SiC [130].

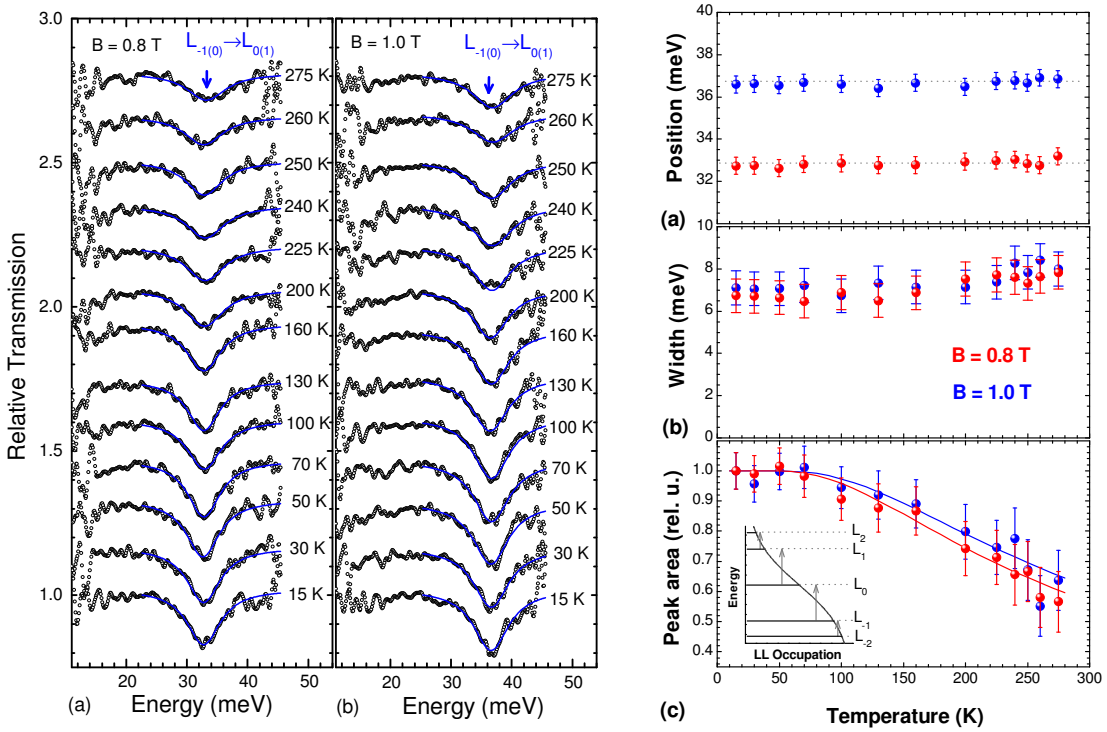


Figure 6.5: **Left:** Temperature dependence of the transmission spectra taken at $B = 0.8$ and 1.0 T in parts (a) and (b), respectively, showing the $L_{-1(0)} \rightarrow L_{0(1)}$ transition up to room temperature. The blue curves represent the Lorentzian fits whose parameters are plotted in right figure. Successive spectra in both parts are shifted vertically by 0.15. **Right:** Parameters of the Lorentzian fits to the transmission spectra. Red and blue color represent data for $B = 0.8$ and 1.0 T, respectively. Whereas position and width of absorption lines in parts (a) and (b) show none or a very a weak temperature dependence, the peak area in the part (c) significantly decreases with T, nearly following the theoretical expectation $1-2f_1$ depicted by solid lines. The inset schematically shows the LL occupation and possible dipole-allowed absorption processes between LLs at finite temperature in undoped graphene ($E_F = 0$). The measurement was performed on multilayered epitaxial graphene on SiC [130].

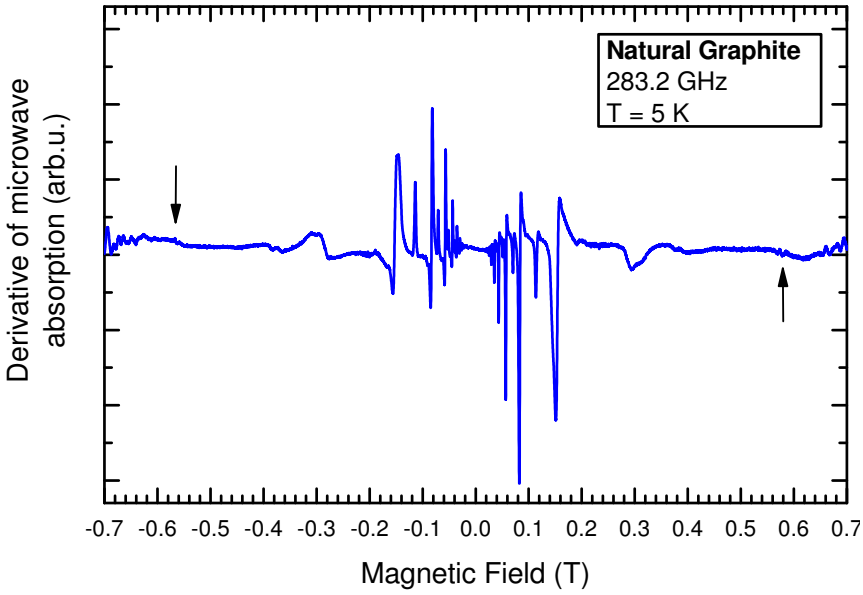


Figure 6.6: Magneto-absorption spectra of bulk natural graphite taken in the FP resonator at temperature 5 K and at MW frequency 283.2 GHz ($\hbar\omega = 1.171$ meV). The black arrows denote the basic cyclotron resonance. More information about cyclotron resonance on bulk graphite can be found in Appendix D.

$$\sigma_{xx}(\omega, B) = \frac{4e^2\tilde{c}^2}{\omega}\frac{|eB|}{h}\sum_{m,n} M_{m,n}\frac{f_n - f_m}{E_m - E_n - (\hbar\omega + i\gamma)}, \tag{6.5}$$

where $\omega$ and $B$ is applied MW and magnetic field respectively, $f_n$, $f_m$ are occupation of the $n$-th, $m$-th LL and $M_{m,n} = \alpha\delta_{|m|,|n|\pm1}$ with $\alpha = 2$ for $n$ or $m$ equal 0 otherwise $\alpha = 1$ [128, 134]. The parameters $\gamma$ describes the phenomenologically introduced broadening of Landau levels.

## 6.5 LL Spectroscopy of Graphene on the Surface of Bulk Graphite

Recently, well-defined graphene flakes have been discovered in form of sheets, decoupled from, but still located on the surface of bulk graphite which naturally serves as a well-matched substrate for graphene [115]. In this work, we report on response from these flakes in MW magneto-absorption experiments and show that their Dirac-like electronic states are quantized into LLs in magnetic fields down to 1 mT and at elevated temperatures up to 50 K. The deduced unprecedented quality of the studied electronic system sets surprisingly high limits for the intrinsic scattering time and the corresponding carrier mobility in graphene.

The cyclotron resonance has been measured in our HF-EPR setup, already described in Chapter 3, in double-pass (non-resonance) cavity as well as in FP resonator configuration (Fig. 3.5). A flake of natural graphite (about size 3 mm×3 mm×0.1 mm) was placed in the variable temperature insert of the magnet. The applied magnetic field was perpendicular to the graphene sheets. Via QO the natural graphite was exposed to the

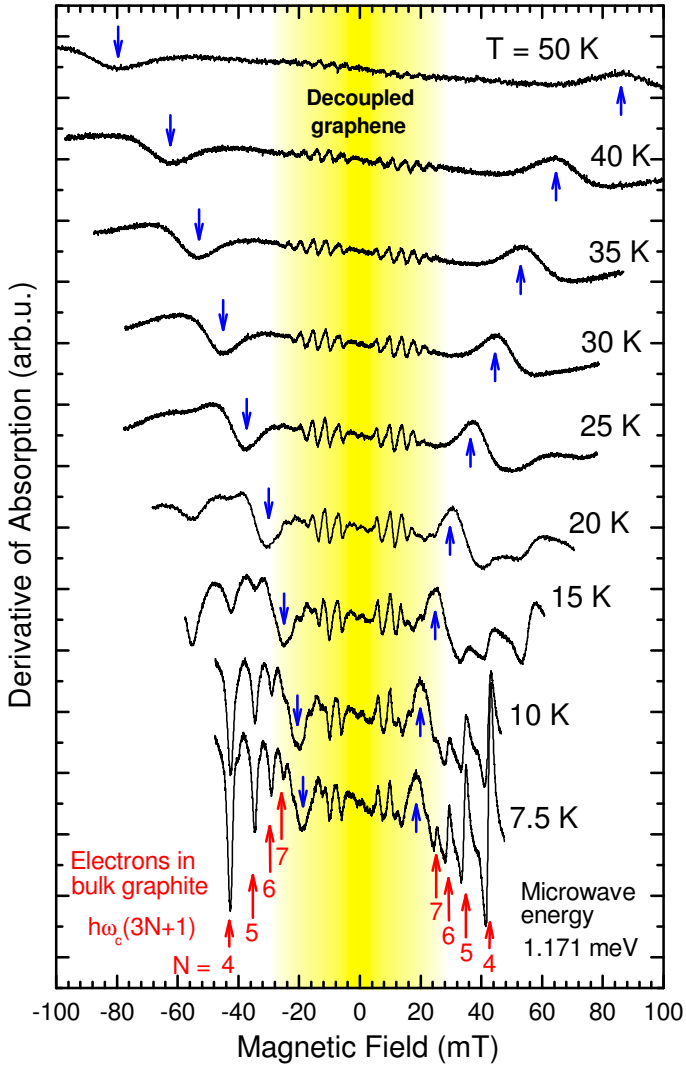


Figure 6.7: Magneto-absorption spectra of natural graphite specimen taken in the temperature interval $7.5 - 50$ K at fixed MW energy $\hbar\omega = 1.171$ meV (230 GHz). The response of low electron concentration graphene layers decoupled from bulk graphite is seen within the yellow highlighted area. High CR harmonics of $K$ point electrons in bulk graphite [135], with basic CR frequency $\omega_c$ corresponding to the effective mass $m = 0.054m_0$ [136] are shown by red arrows, see Fig. 6.6. The origin of features denoted by blue arrows is discussed in the text.

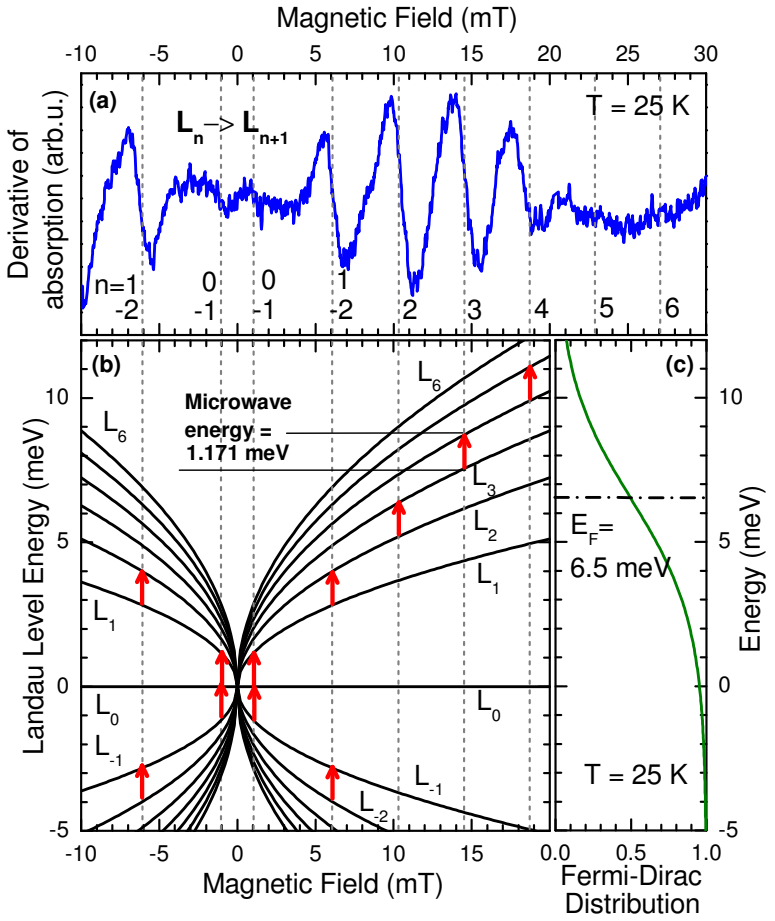


Figure 6.8: Magneto-absorption spectrum (after removing a weak linear background seen in the raw data of Fig. 6.7) measured at $T = 25\,\mathrm{K}$ and MW frequency $\hbar\omega = 1.171\,\mathrm{meV}$ (230 GHz) (a) in comparison with the LL fan chart (b), where the observed CR transitions are shown by arrows. The occupation of individual LLs is given by the Fermi-Dirac distribution plotted in the part (c). For simplicity, we considered only $n$-type doping with $E_F = 6.5\,\mathrm{meV}$. The dashed lines show positions of resonances assuming $\tilde{c} = 1.00 \times 10^6\,\mathrm{m.s^{-1}}$.

linearly polarised MW radiation emitted by a Gunn diode at frequencies 283.2 or 345 GHz (1.171 or 1.427 meV). The absorbed radiation has been followed by either heterodyne detection (283.2 GHz, Fig. 3.9) or by the bolometer (345 GHz). The modulation amplitude ($\Delta B \sim 0.5\,\mathrm{mT}$) had to be chosen close to the CR width, which broadens resonances observed at lower magnetic fields. All spectra have been corrected for the remanent field of the magnet.

Our main experimental finding is illustrated in Fig. 6.7. The traces in this figure represent the best observed magneto-absorption response of the natural graphite specimen at different temperatures, measured as a function of the magnetic field at fixed MW frequency. Strong at 7.5 K, but rapidly vanishing with temperature lines marked with red arrows in Fig. 6.7 can be easily recognized as CR harmonics of $K$ point electrons in bulk graphite, Fig. 6.6 (Appendix D). A possible origin of the temperature dependent transition marked with the blue arrow in the Fig. 6.7 will be discussed later on. The features of primary interest, which we argue are due to decoupled graphene sheets from the bulk graphite, are seen at very low fields, within the yellow highlighted area of Fig. 6.7.

The interpretation of these low-field data is schematically illustrated in Fig. 6.8. The observed spectral lines (Fig. 6.8a) are assigned to cyclotron resonance transitions between adjacent LLs ($|\Delta n| = 1$) with energies: $E_n = \mathrm{sign}(n)\tilde{c}\sqrt{2e\hbar B|n|} = \mathrm{sign}(n)E_1\sqrt{B|n|}$ [110, 111], characteristic of massless Dirac fermions in graphene sheets with an effective Fermi

velocity $\tilde{c}$. As was mentioned previously, this velocity is the only adjustable parameter required to match the energies of the observed and calculated CR transitions. A best match is found for Fermi velocity $\tilde{c} = (1.00 \pm 0.02) \times 10^6\,\mathrm{m.s^{-1}}$ in fair agreement with values found in multilayer epitaxial graphene [128, 137] or exfoliated graphene on $Si/SiO_2$ substrate [133, 138, 139]. As can be seen from Figs. 6.8b,c the multi-mode character of the measured spectra is directly related to thermal distribution of carriers among different LLs. The intensity of a given transition is proportional to the difference in thermal occupation of the involved LLs. Roughly speaking, the strongest transitions imply LLs in the vicinity of the Fermi level, which fixes $E_F$ at around 6-7 meV from the Dirac point.

To reproduce the experimental data, we assume the absorption strength is proportional to the longitudinal conductivity $\sigma_{xx}$ of the system described by Eq. (6.5). The simulated traces in Fig. 6.9 have been drawn taking $\gamma = 35\,\mu$eV for the line broadening, Fermi velocity $\tilde{c} = 1.00 \times 10^6\,\mathrm{m.s^{-1}}$ and the Fermi level $E_F = 6.5\,$meV. To directly simulate the measured traces, the derivative of the absorption with respect to the magnetic field has been calculated taking account of the field modulation $\Delta B = 0.5\,$mT used in the experiment. In spite of its simplicity, our model is more than in a qualitative agreement with our experimental data, see Fig. 6.9. The calculation fairly well reproduces the experimental trends: Multi-mode character of the spectra, the intensity distribution among the lines, as well as its evolution with temperature, and allows to estimate the characteristic broadening of the CR transitions.

Although our modelling could be further improved it would be at the expense of additional complexity, which we want to avoid here. Assuming magnetic-field and/or LL index dependence of the broadening parameter $\gamma$ and taking into account the possible fluctuation of the Fermi level within the ensemble of probed flakes would improve the agreement between experiment and theory, particularly at low temperatures. Comparing both, the measured and simulated traces, we are also more confident in the spectacular observation of the CR transition (involving the $n = 0$ LL) at a magnetic field as low as 1 mT. Bearing in mind the small value of the extracted broadening parameter one may conclude that LL quantization should survive in studied graphene layers down to the field of $B = (\gamma/E_1)^2 \approx 1\,\mu$T. Hence, the magnetic field of the Earth of $\sim 50\,\mu$T is no longer negligibly small. Instead, it can open an energy gap at the Dirac point up to $\Delta \approx 0.3\,$meV, depending on the sample orientation.

To crosscheck our interpretation, we have also measured the spectra using a different (higher) MW frequency 345 GHz ($\hbar\omega = 1.427\,$meV), see Fig. 6.10. Despite the weaker sensitivity of the experimental setup at this frequency[4], we can clearly identify the same set of inter-LL transitions simply shifted to higher magnetic fields.

The finite Fermi energy $E_F \approx 6 - 7\,$meV, corresponding to a carrier density of $n_0 \approx 3 \times 10^9\,\mathrm{cm^{-2}}$, indicates that the probed layers are in thermodynamical contact with the surrounding material, which supplies these carriers. On the other hand, we find no signs of electrical coupling of these graphene layers to bulk graphite. Our experiments show that any possible energy gap opened due to this interaction at the Dirac point cannot exceed a few hundred $\mu$eV. The absence of this gap convincingly confirms that we are indeed dealing with decoupled graphene and not with the $H$ point of bulk graphite, where Dirac-like fermions are also present [137] but a (pseudo)gap of a few meV is expected [124]

[4]For the detection of 345 GHz was used the bolometer and the source of MW has a weaker output power than 283.2 GHz source.

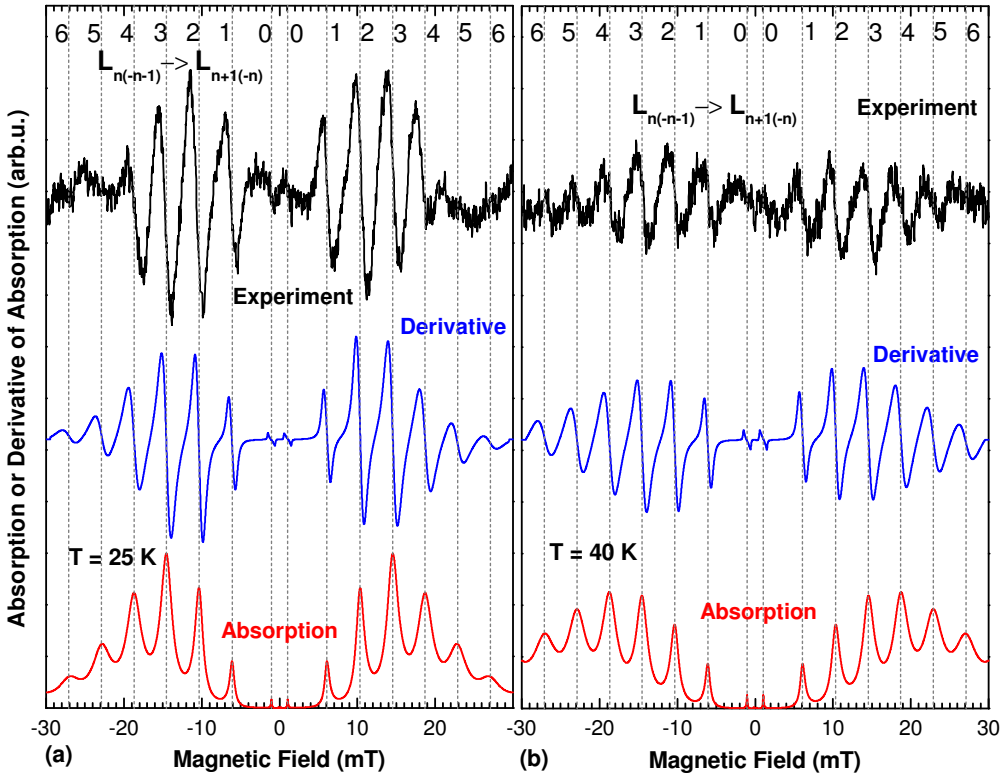


Figure 6.9: Background-removed magneto-absorption spectra from experiment at $T = 25$ and $40\,\mathrm{K}$ (black curves) in comparison to the response at the MW frequency $\hbar\omega = 1.171\,\mathrm{meV}$ (230 GHz) calculated for parameters $\tilde{c} = 1.00 \times 10^6\,\mathrm{m.s}^{-1}$, $\gamma = 35\,\mu\mathrm{eV}$ and $E_F = 6.5\,\mathrm{meV}$. The dashed lines show the calculated positions of the CR transitions.

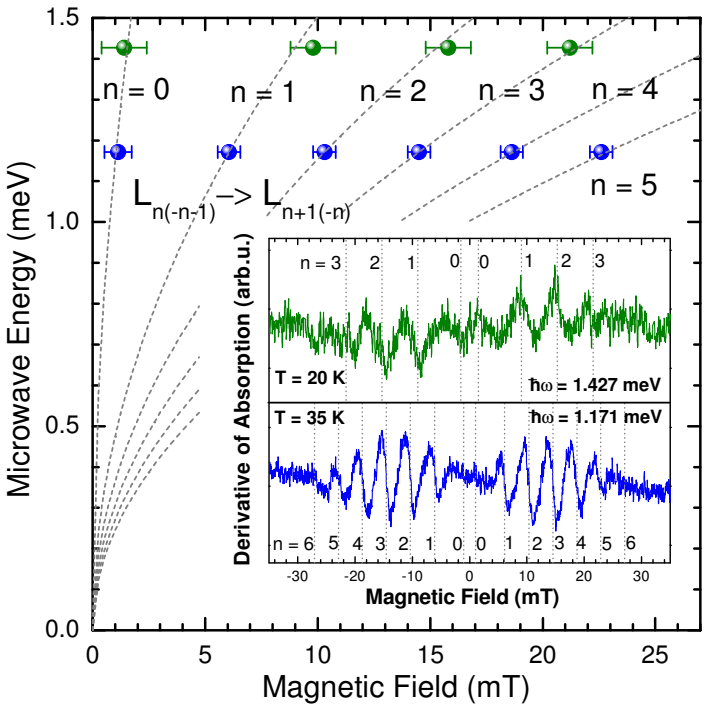


Figure 6.10: Positions of CRs at MW energies $\hbar\omega = 1.171\,\mathrm{meV}$ (230 GHz) and 1.427 meV (345 GHz). Each position represents an average value obtained at different temperatures. One background-removed CR spectrum at each MW frequency with a high number of observed CRs is shown in the inset. The grey curves show positions of CRs for $\tilde{c} = 1.00 \times 10^6\,\mathrm{m.s^{-1}}$.

and indeed observed [140]. The temperature evolution of the measured spectra is another important indication allowing us to discriminate between the graphene and bulk graphite contributions. No (or very weak) temperature broadening of CR transitions is expected for graphene [137, 141, 142], whereas the response of bulk graphite should follow the relatively strong decrease of the carrier scattering time, expressed by the average mobility, which reaches up to $10^6\,\mathrm{cm^2/(V.s)}$ at low temperatures, but falls down by one order of magnitude at $T \approx 50\,\mathrm{K}$ [136]. Indeed, this behaviour is observed in Fig. 6.7. Whereas the CR harmonics of $K$ point electrons in bulk graphite [135] seen in the spectra at $|B| \geq 20\,\mathrm{mT}$, disappear very rapidly upon increasing $T$, the graphene-like features survive and their intensity is simply following the vanishing difference in the occupation between the adjacent LLs. It is worth noticing that the graphene-like signal, although always substantially weaker then the response from bulk graphite (Fig. 6.6), has been observed for a number of different specimens of natural graphite. Here we are showing our best recorded spectra. Mechanical scratching of the sample surface and fast thermal cooling of the sample has been found to enhance the signal from decoupled graphene in comparison with bulk graphite, likely helping in detaching graphene sheets from the graphite crystal.

Since the well-defined LL quantization in our graphene flakes is observed down to $|B| = 1\,\mathrm{mT}$, see Fig. 6.8, we obtain via the semi-classical LL quantization condition $\mu B > 1$ the carrier mobility $\mu > 10^7\,\mathrm{cm^2/(V.s)}$, two orders of magnitude higher in comparison with suspended graphene specimen $\mu > 2 \times 10^5\,\mathrm{cm^2/(V.s)}$ [142, 143, 144] or epitaxial graphene $\mu > 2.5 \times 10^5\,\mathrm{cm^2/(V.s)}$ [130]. The LL broadening $\gamma$, obtained via comparison of our experiment with the simulated traces, allows us to estimate the scattering time $\tau \approx 20\,\mathrm{ps}$ ($\tau = \hbar/\gamma$), which significantly exceeds those reported in any kind of manmade graphene samples, see e.g. Refs. [142, 143], and gives an independent estimation for the mobility $\mu = e\tau\tilde{c}^2/E_F \approx 3 \times 10^7\,\mathrm{cm^2/(V.s)}$ in good agreement with the estimate

above. Even though we cannot verify this estimate by a direct electrical measurement, a near correspondence of the scattering time derived from CR measurements and transport scattering time was recently verified on samples with a significantly lower mobility [133]. Moreover, the estimated mobility should not decrease with temperature, as no broadening of CRs is observed up to $T = 50\,\mathrm{K}$, when CR intensities become comparable with the noise. This extremely high value of mobility combines two effects: the long scattering time $\tau$ and a very small effective mass $m = E_F/\tilde{c}^2 \approx 2 \times 10^{-4} m_0 E_F[\mathrm{meV}]$. Remarkably, the same scattering time in a moderate density sample ($n_0 = 10^{11}\,\mathrm{cm}^{-2}$), would imply the mobility still remaining high, around $\mu \approx 5 \times 10^6\,\mathrm{cm}^2/(\mathrm{V.s})$, and comparable to best mobilities of two-dimensional electron gas in GaAs structures $\mu > 10^7\,\mathrm{cm}^2/(\mathrm{V.s})$ at $0.1\,\mathrm{K}$) at these densities [145].

The model (Eq. (6.5)) we used here to describe the magneto-absorption response of Dirac fermions in graphene is amazingly simple, based on a one-particle approximation, and it is perhaps surprising that it is so well applicable to simulate the experimental data, particularly in context of the outstanding quality of the electronic system studied. At first sight, the observation of collective excitations, due to, e.g., magneto-plasmons could be expected in our experiments and only preliminary theoretical work addresses the surprising approximate validity of Kohn's theorem in graphene [146, 147]. Also size-confined magneto-plasmons are apparent in the microwave-absorption spectra of two-dimensional gas of massive electrons [148], but apparently not seen in our experiments on graphene. This perhaps points out the qualitative difference in the plasmon behaviour in systems with quadratic and linear dispersion relations [149, 150]. On the other hand, we speculate that the transition, marked with blue arrows in Fig. 6.7 has a character of a collective excitation (Brillouin function). It is characterized by a sensitivity to the magnetic field and by softening with temperature. The energy of this excitation can be deduced to scale roughly as $B/T$, and this points towards its magnetic origin. For example, $B/T$ energy scaling is typical of a ferromagnetic resonance, see e.g. Ref. [151]. Nevertheless, the origin of the spectral feature marked by blue arrows in Fig. 6.7 remains an intriguing puzzle. We see this feature repeatedly on different samples, but at slightly different energies, each time however characteristically evolving with temperature. With its apparent magnetic characteristics one should seek its origin in impurities [152], structural defects [153] or edge states [154] in graphene, but possibly also on the surface of bulk graphite [155].

## 6.6 Conclusion

Fabrication of graphene has triggered vast research efforts focusing on the properties of two-dimensional systems with massless Dirac fermions. Nevertheless, further progress in exploring this quantum electrodynamics system in solid-state laboratories seems to be limited by insufficient electronic quality of manmade structures and the crucial question arises whether existing technologies have reached their limits or major advances are, in principle, possible.

The substrate, and more generally any surrounding medium, have been recently identified as the dominant source of extrinsic scattering mechanisms, which effectively degrade the electronic quality of currently available graphene samples [143, 156]. Despite significant advances in technology, including the fabrication of suspended specimens [142, 144], the realistic limits of the scattering time and mobility in graphene, achievable after elimi-

nation of major extrinsic scattering sources, remain an open issue.

Here we have shown that graphene in a significantly purer state can be found in nature on the surface of bulk graphite, in the form of flakes decoupled from the substrate material. Probing such flakes with Landau level spectroscopy in the sub-THz range at very low magnetic fields, we demonstrated a superior electronic quality of these ultra low density layers ($n_0 \sim 3 \times 10^9\,\mathrm{cm}^{-2}$) expressed by the carrier mobility in excess of $10^7\,\mathrm{cm}^2/(\mathrm{V.s})$. This finding represents an important challenge for further improvements of current graphene technologies.

# Chapter 7

# Overall Conclusion and Perspectives

In this work, we were upgrading the existing cw-HF-EPR spectrometer to a pulsed one which should operate close to a frequency of 285 GHz. The existing cw-HF-EPR spectrometer was based on QO MW propagation, phase-locked Gunn diodes and on bolometric detection. Except for the bolometric detection, the existing components were used for the new set-up. The slow bolometric (homodyne) detection, used previously, was replaced by a fast superheterodyne detection, adapted to detecting MW pulses. A MW source, based on a 141.6 GHz phase-locked Gunn diode with a frequency doubler, which produces MW at frequency close to the existing 285 GHz, was initially implemented as the excitation source for the heterodyne system, as described in Chapter 3. The MW pulses were produced by inserting a fast PIN switch on the 141.6 GHz frequency of the Gunn diode before multiplication to 283.2 GHz. Furthermore, a Fabry - Pérot (FP) resonator was developed in order to enhance the excitation MW power on the sample (Chapter 4). A FP resonator in a half-symmetric configuration was constructed using a piezoelectric nanopositioner for the mirrors adjustment. To the best of our knowledge, it is the first fully piezoelectric tuned FP resonator used in HF-EPR. The flat semitransparent mirrors (meshes), used in our FP resonator, were fabricated in house on glass cover slips by photolithography. The developed photolithographic process is described in detail in Appendix C. As a side project, we also built a new rotating holder for a single crystal orientation study based on a construction similar to the FP resonator one. The new rotating holder enables controlling and reading of the sample orientation with a precision better than 1°. Both systems rely on piezoelectric nanopositioners, which allow controlling either the distance between the mirrors or the angular position of a single crystal very precisely and comfortably (see Chapter 3). Using the FP resonator the absolute sensitivity of the cw-HF-EPR spectrometer at room temperature was enhanced by one order of magnitude to $3 \times 10^8$ spins/G$\cdot\sqrt{\text{Hz}}$ with respect to the previous configuration. The measured finesse $F_{exp}$ of the FP resonator obtained with superheterodyne detection at 283.2 GHz approaches 400, depending on the resonator mode and on the sample (Figs. 3.6 and 4.8). Such a high finesse indicates that the FP resonator can be successfully used for the spectrometer operating in the pulsed mode.

However, the progress in our pulsed HF-EPR spectrometer development was negatively affected and slowed down by the failure of the semiconducting element in the main excitation source based on a Gunn diode. This situation required the replacement of the excitation source by a new one, based on an actively multiplied DRO, and did not allow

pulsed experiments before the submission of this thesis. Nevertheless, the performance of the FP resonator with the previous superheterodyne detection could be demonstrated. The sensitivity, as well as the other results described in this work, were measured only with the old 283.2 GHz excitation source (Fig. 3.9). The sensitivity is expected to be better with the new excitation source due to its higher output power. Hopefully, pulsed operation will be soon possible.

In this manuscript, experimental studies performed with these new systems are presented, illustrating their performances. The FP resonator together with the superheterodyne detection allowed us to perform very precise cyclotron resonance measurements on natural graphite as well as to detect cyclotron resonance signal of decoupled graphene sheets located on the surface of bulk graphite (Chapter 6 and Appendix D). Analyzing these data, a superior quality of this low density layer ($n_0 \sim 3 \times 10^9\,\mathrm{cm}^{-2}$), expressed in terms of the charge carrier mobility exceeding $10^7\,\mathrm{cm}^2/(\mathrm{V.s})$ was demonstrated, setting new and surprisingly high limits for intrinsic properties of graphene.

The advantage of using HF-EPR to study the magnetic anisotropy of systems with high ZFS such as SMMs is well known. In Chapter 5, we focused on SMMs from the family of tetrairon(III) complexes with propeller-like structure. These complexes are particularly appealing because they are good candidates to realize addressable SMMs as they have been shown to keep their SMM behaviour even when are grafted on a surface. We describe the investigation of four new species in the polycrystalline powder form. A detailed single crystal study was then performed on one of them. Measurements of powdered samples allowed us to extract the second order parameters $D$ and $E$ and estimate the axial fourth order term $B_4^0$ of the spin Hamiltonian. Furthermore, it was possible to correlate the axial ZFS term $D$ with the structure obtained by the X-ray diffraction (Fig. 5.11). The single crystal study of a sample using the newly developed rotating holder, allowed a more reliable estimation of the axial fourth order term $B_4^0$ as well as of the transverse anisotropy, the second term $E$ and especially the fourth order term $B_4^3$. The last term $B_4^3$ was unknown before the single crystal study. The determination of the transverse anisotropy terms is important for the understanding of the relaxation processes in the complex. The study of the $Fe_4$ complexes will be completed, especially with the single crystal study of the other three complexes.

The technical improvement of the HF-EPR spectrometer is still in progress in our laboratory. Currently, a new magnet with a higher maximum field (16 T instead of 12 T), a better homogeneity over the sample volume (5 ppm) and equipped with a VTI of 50 mm inner bore is being installed. The magnet will allow the use of sources operating at higher frequency, for instance the 345 GHz source with central field (g = 2) above 12 T. The magnet is also better suited for pulsed experiments with respect to the current one where the magnetic field stability is poor. The new magnet is furnished with a superconducting switch and a sweep coil. The space in the cryostat will not be limiting as it was until now. For instance, the rotating holder will be simplified by removing the gear mechanism and the sample will be directly placed on the rotating piezoelectric nanopositioner located in vertical position beside the sample. This change will lead to an even higher precision of the sample orientation ($\sim 0.05°$). Another perspective for the improvement of the spectrometer concerns the resonator. The FP resonator was designed in such a way to allow the future implementation of a single-mode cavity; thus the structure can support both the FP resonator and the single-mode cavity. The housing of the FP resonator need

only to be replaced by a new housing with a metallic cavity; the cavity tuning will then be performed by a simple mechanism which will use the same piezoelectric nanopositioner as the one used for the FP resonator tuning. Below the actual piezoelectric nanopositioner, there is some space left for another piezoelectric nanopositioner which could rotate the cavity and its coupling hole with respect to the single-mode waveguide transition.

These new developments are intended especially for the pulsed HF-EPR spectroscopy. This technique is indeed developing more and more, with a special focus on distance measurements in large biomolecules. Another motivation for the pulsed operation deals with the understanding of the decoherence in SMMs, especially for the tetrairon(III) derivatives discussed in the text. However, very high MW irradiation power for pulsed spectrometers operating at 300 GHz is needed. Excite enough spins which will participate to the signal or even excite whole spectrum is very hard, thus pulsed HF-EPR still remains technically challenging.

# References


[1] *www.microwaves101.com* .

[2] *Custom Microwave INC* .

[3] Blume, R. J. *Phys. Rev.* **109**, 1868–1873 (1958).

[4] Kaplan, D. E., Browne, M. E., and Cowen, J. A. *Rev. Sci. Instrum.* **32**, 1182–1186 (1961).

[5] Mims, W. B., Nassau, K., and McGee, J. D. *Phys. Rev.* **123**, 2059–2069 (1961).

[6] Grinberg, O. and Berliner, L. J. *Bio. Mag. Reson.* **22**, 353 (2004).

[7] Haindl, E., Möbius, K., and Oloff, H. *Z. Naturforsch.* **40**, 169–172 (1985).

[8] Lynch, W. B., Earle, K. A., and Freed, J. H. *Rev. Sci. Instrum.* **59**, 1349 (1988).

[9] Weber, R. T., Disselhorst, J. A. J. M., Prevo, L. J., Schmidt, J., and Wenckebach, W. T. *J. Magn. Reson.* **81**, 129–144 (1989).

[10] Muller, F., Hopkins, A., Coron, N., Grynberg, M., Brunel, L.-C., and Martinez, G. *Rev. Sci. Instrum.* **60**, 3681–3684 (1989).

[11] Barra, A.-L., Brunel, L.-C., and Robert, J. B. *Chem. Phys. Lett.* **165**, 107–109 (1990).

[12] Kutter, C., Moll, H. P., van Tol, J., Zuckermann, H., Maan, J. C., and Wyder, P. *Phys. Rev. Lett.* **74**, 2925–2928 (1995).

[13] Smith, G. M., Lesurf, J. C. G., Mitchell, R. H., and Riedi, P. C. *Rev. Sci. Instrum.* **69**, 3924 (1998).

[14] Feher, G. *Bell Syst. Tech. J.* **36**, 449 (1957).

[15] Poole, C. P. *ELECTRON SPIN RESONANCE: A Comprehensive Treatise on Experimental Techniques.* DOVER, Mineola, New York, second edition, (1997).

[16] Budil, D. E. and Earle, K. A. *Bio. Mag. Reson.* **22**, 353 (2004).

[17] Freed, J. H. *Bio. Mag. Reson.* **22**, 19 (2004).

[18] Möbius, K., Savitsky, A., Schnegg, A., Plato, M., and Fuchs, M. *Phys. Chem. Chem. Phys.* **7**, 19–42 (2005).

[19] Hassan, A. K., Pardi, L. A., Krzystek, J., Sienkiewicz, A., Goy, P., Rohrer, M., and Brunel, L.-C. *J. Magn. Res.* **142**, 300–312 (2000).

[20] Prisner, T. F. *Advances in Magnetic and Optical Resonance* **20**, 245–299 (1997).

[21] Barnes, J. P. and Freed, J. H. *Rev. Sci. Instrum.* **69**, 3022 (1998).

[22] Wertz, J. E. and Bolton, J. R. *ELECTRON SPIN RESONANCE: Elementary Theory and Applications*. Chaptman and Hall, New York, (1988).

[23] Burghaus, O., Rohrer, M., Gtzinger, T., Plato, M., and Möbius, K. *Meas. Sci. Technol.* **3**, 765 (1992).

[24] Carrington, A. and McLachlan, A. D. *INTRODUCTION TO MAGNETIC RESONANCE with application to chemistry and chemical physics*. A Harper International Edition, (1967).

[25] Schweiger, A. and Jeschke, G. *Principles of Pulsed Electron Paramagnetic Resonance*. Oxford University Press, (2001).

[26] Reijerse, E., Schmidt, P. P., Klihm, G., and Lubitz, W. *Appl. Magn. Reson.* **31**, 611–626 (2007).

[27] Hofbauer, W., Earle, K. A., Dunnam, C. R., Moscicki, J. K., and H.Freed, J. *Rev. Sci. Instrum.* **75**, 1194 (2004).

[28] Morley, G. W., Brunel, L.-C., and van Tol, J. *Rev. Sci. Instrum.* **79**, 064703 (2008).

[29] Reijerse, E. J. *J. Magn. Reson.* **37**, 795–818 (2010).

[30] Cruickshank, P. A. S., Bolton, D. R., Robertson, D. A., Hunter, R. I., Wylde, R. J., and Smith, G. M. *Rev. Sci. Instrum.* **80**, 103102 (2009).

[31] Collin, R. *Foundations for Microwave Engineering*. Second Edition, John Wiley & Sons, New York, (2000).

[32] Purcell, E. M., Torrey, H. C., and Pound, R. V. *Phys. Rev.* **69**, 37–38 (1946).

[33] *nobelprize.org* .

[34] Hahn, E. L. *Phys. Rev.* **80**, 580 (1950).

[35] *www.bruker-biospin.com* .

[36] Bennati, M. and Prisner, T. F. *Rep. Prog. Phys.* **68**, 411–448 (2005).

[37] Boehme, C. and Lips, K. *Phys. Rev. Lett.* **91**, 246603 (2003).

[38] Overhauser, A. W. *Phys. Rev.* **92**, 411–415 (1953).

[39] Prisner, T. and Köckenberger, W. *Appl. Magn. Reson.* **34**, 213–218 (2008).

[40] Barra, A.-L., Gatteschi, D., and Sessoli, R. *Phys. Rev. B* **56**, 8192–8198 (1997).

[41] Barra, A.-L., Gatteschi, D., and Sessoli, R. *Chem. Eur. J.* **6**, 1608–1614 (2000).

[42] Martinelli, M., Massa, C. A., Pardi, L. A., Bercu, V., and Popescu, F. F. *Phys. Rev. B* **67**, 014425 (2003).

[43] Mukhin, A. A., Travkin, V. D., Zvezdin, A. K., Lebedev, S. P., Caneschi, A., and Gatteschi, D. *Europhys. Lett.* **44**, 778 (1998).

[44] Mukhin, A. A., Gorshunov, B., Dressel, M., Sangregorio, C., and Gatteschi, D. *Phys. Rev. B* **63**, 214411 (2001).

[45] Kutter, C. *Pulsed Electron Paramagnetic Resonance in High Magnetic Fields using Far Infrared Lasers.* Dissertation, Freie Universität Konstanz, (1995).

[46] Grishin, Y. A., Fuchs, M. R., Schnegg, A., Dubinskii, A. A., Dumesh, B. S., Rusin, F. S., Bratman, V. L., and Möbius, K. *Rev. Sci. Instrum.* **75**, 2926–2936 (2004).

[47] Bajaj, V. S., Farrar, C. T., Hornstein, M. K., Mastovsky, I., Vieregg, J., Bryant, J., Eléna, B., Kreischer, K. E., Temkin, R. J., and Griffin, R. *J. Magn. Reson.* **160**, 85–90 (2003).

[48] Fuchs, M. R. *A High-Field / High-Frequency Electron Paramagnetic Resonance Spectrometer (360 GHz / 14 T).* Dissertation, Freie Universität Berlin, (1999).

[49] Blok, H., Disselhorst, J. A. J. M., Orlinskii, S. B., and Schmidt, J. *J. Magn. Reson.* **166**, 92 (2004).

[50] Rohrer, M., Brügmann, O., Kinzer, B., and Prisner, T. F. *Appl. Magn. Reson.* **21**, 257–274 (2001).

[51] Cardin, J. T., Kolaczkowski, S. V., Anderson, J. R., and Budil, D. E. *Appl. Magn. Reson.* **19**, 273–292 (1999).

[52] Born, M. and Wolf, E. *Principles of optics.* Cambridge University Press, (2006).

[53] Goldsmith, P. F. *QUASIOPTICAL SYSTEMS: Gausian Beam Quasioptical Propagation and Applications.* IEEE Press, New York, (1998).

[54] Fuchs, M. R., Prisner, T. F., and Möbius, K. *Rev. Sci. Instrum.* **70**, 3681 (1999).

[55] van Tol, J., Brunel, L.-C., and Wylde, R. J. *Rev. Sci. Instrum.* **76**, 74101 (2005).

[56] Hertel, M. M., Denysenkov, V. P., Bennati, V. P., and Prisner, T. F. *Mag. Reson. Chem.* **43**, 248–255 (2005).

[57] Blok, H. *Electron Paramagnetic Resonance and Electron Nuclear Double Resonance Spectroscopy at 275 GHz.* Ph.D. Thesis, Universiteit Leiden, (2006).

[58] Kogelnik, H. and Li, T. *Appl. Opt.* **5**, 1550 (1966).

[59] Boyd, G. D. and Kogelnik, H. *Bell Syst. Tech. J.* **41**, 1347–1369 (1962).

[60] Kogelnik, H. *LASERS: A series of advances, Chapter Five: Modes in Optical Resonators.* Edward Arnold, London, (1966).

[61] Wylde, R. J. *IEE Proceedings* **131**, 258–262 (1984).

[62] Hunter, R. I., Robertson, D. A., Goy, P., and Smith, G. M. *IEEE Trans. Micro. Theo. Tech.* **55**, 890–898 (2007).

[63] Kogelnik, H. *Coupling and Conversion Coefficients for Optical Modes - Presented at the Symphosium on Quasi-Optics.* Polytechnic Instutute of Brooklyn, (1964).

[64] Barra, A.-L., Hassan, A. K., Janoschka, A., Schmidt, C. L., and Schnemann, V. *Appl. Magn. Res.* **30**, 385–397 (2006).

[65] Portis, A. M. and Teaney, D. *J. Appl. Phys.* **29**, 1692–1698 (1958).

[66] Tkach, I., Rogulis, U., Greulich-Weber, S., and Spaeth, J.-M. *Rev. Sci. Instrum.* **75**, 4781 (2004).

[67] Lamb, J. W. *Int. J. Infrared and Millimeter Waves* **17**, 1997–2034 (1996).

[68] Neugebauer, P. and Barra, A.-L. *Appl. Magn. Res.* **37**, 833–843 (2010).

[69] Rohrer, M., Krzystek, J., Williams, V., and Brunel, L.-C. *Meas. Sci. Technol.* **10**, 275 (1999).

[70] Earle, K. A., Tipikin, D. S., and Freed, J. H. *Rev. Sci. Instrum.* **67**, 2502–2513 (1996).

[71] Lide, D. R. *CRC Handbook of Chemistry and Physics.* CRC Press, 74. Edition, (1993).

[72] Ulrich, R. *Infrared Phys.* **7**, 37–55 (1967).

[73] Botten, L. C., MvPhedran, R. C., and Lamarre, J. M. *Int. J. Infrared and Millimeter Waves* **6**, 511–575 (1985).

[74] Nemoto, S. *Appl. Opt.* **27**, 1833–1839 (1988).

[75] Lesurf, J. C. G. *Millimetre-wave Optics, Devices and Systems.* Adam Hilger, Bristol and New York, (1990).

[76] Halpern, M., Gush, H. P., Wishnow, E., and Cosmo, V. D. *Appl. Opt.* **25**, 565–570 (1986).

[77] Caneschi, A., Gatteschi, D., Sessoli, R., Barra, A. L., Brunel, L.-C., and Guillot, M. *J. Am. Chem. Soc.* **113**, 5873–5874 (1991).

[78] Leuenberger, M. N. and Loss, D. *Nature* **410**, 786 (2001).

[79] Leuenberger, M. N. and Loss, D. *Phys. Rev. B* **61**, 12200 (2000).

[80] Ardavan, A., Rival, O., Morton, J. J. L., Blundell, S. J., Tyryshkin, A. M., Timco, G. A., and Winpenny, R. E. P. *Phys. Rev. Lett.* **98**, 057201 (2007).

[81] Bogani, L. and Wernsdorfer, W. *Nature Mat.* **7**, 179 (2008).

[82] Rocha, A. R., García-Suárez, V. M., Bailey, S. W., Lambert, C. J., Ferrer, J., and Sanvito, S. *Nature Mat.* **4**, 335 (2005).

[83] Gatteschi, D., Sessoli, R., and Villain, J. *Molecular Nanomagnets*. Oxford University Press, New York, (2006).

[84] Abragam, A. and Bleaney, B. *Electron Paramagnetic Resonance of Transition Ions*. Dover Publications, New York, (1986).

[85] Accorsi, S., Barra, A.-L., Caneschi, A., Chastanet, G., Cornia, A., Fabretti, A. C., Gatteschi, D., Mortalo, C., Olivieri, E., Parenti, F., Rosa, P., Sessoli, R., Sorace, L., Wernsdorfer, W., and Zobbi, L. *J. Am. Chem. Soc.* **128**, 4742–4755 (2006).

[86] Barra, A.-L., Bianchi, F., Caneschi, A., Cornia, A., nad L. Gorini, D. G., Gregoli, L., Maffini, M., Parenti, F., Sessoli, R., Sorace, L., and Talarico, A. M. *Eur. J. Inorg. Chem.* **2007**, 41454152 (2007).

[87] Cornia, A., Gregoli, L., Danieli, C., Caneschi, A., Sessoli, R., Sorace, L., Barra, A.-L., and Wernsdorfer, W. *Inor. Chem. Acta* **361**, 3481–3488 (2008).

[88] Condorelli, G. G., Motta, A., Pellegrino, G., Cornia, A., Gorini, L., Fragalà, I. L., Sangregorio, C., and Sorace, L. *Chem. Mater.* **20**, 24052411 (2008).

[89] Bogani, L., Danieli, C., Biavardi, E., Bendiab, N., Barra, A.-L., Dalcanale, E., Wernsdorfer, W., and Cornia, A. *Angew. Chem. Int. Ed.* **48**, 746 750 (2009).

[90] Gregoli, L., Danieli, C., Barra, A.-L., Neugebauer, P., Pellegrino, G., Poneti, G., Sessoli, R., and Cornia, A. *Chem. Eur. J.* **15**, 6456–6467 (2009).

[91] Sessoli, R., Gatteschi, D., Caneschi, A., and Novak, M. A. *Nature* **365**, 141 – 143 (1993).

[92] Friedman, J. R., Sarachik, M. P., Tejada, J., and Ziolo, R. *Phys. Rev. Lett.* **76**, 3830 (1996).

[93] Thomas, L., Lionti, F., Ballou, R., Gatteschi, D., Sessoli, R., and Barbara, B. *Nature* **383**, 145–147 (1996).

[94] Wernsdorfer, W., Sessoli, R., Caneschi, A., Gatteschi, D., Cornia, A., and Mailly, D. *J. Appl. Phys.* **87**, 5481–5486 (2000).

[95] Lis, T. *Acta Cryst.* **B46**, 10367–10375 (1992).

[96] Inglis, R., Jones, L. F., Milios, C. J., Datta, S., Collins, A., Parsons, S., Wernsdorfer, W., Hill, S., Perlepes, S. P., Piligkos, S., and Brechin, E. K. *Dalton Trans.* , 34033412 (2009).

[97] Milios, C. J., Inglis, R., A, V., R, B., Wernsdorfer, W., Parsons, S., Perlepes, S. P., Christou, G., and Brechin, E. K. *J. Am. Chem. Soc.* **129**, 12505–12511 (2007).

[98] Mannini, M., Sainctavit, P., Sessoli, R., dit Moulin, C. C., Pineider, F., Arrio, M.-A., Cornia, A., and Gatteschi, D. *Chem. Eur. J.* **14**, 7530–7535 (2008).

[99] Mannini, M., Pineider, F., Sainctavit, P., Danieli, C., Otero, E., Sciancalepore, C., Talarico, A. M., Arrio, M.-A., Cornia, A., Gatteschi, D., and Sessoli, R. *Nature Mat.* **8**, 194–197 (2009).

[100] Margheriti, L., Mannini, M., Sorace, L., Gorini, L., Gatteschi, D., Caneschi, A., Chiappe, D., Moroni, R., Bautier de Mongeot, F., Cornia, A., Piras, F. M., Magnani, A., and Sessoli, R. *Small* **5**, 1460–1466 (2009).

[101] Wende, H. *Nature Mat.* **8**, 165–166 (2009).

[102] Danieli, C., Cornia, A., Cecchelli, C., Sessoli, R., Barra, A.-L., Ponterini, G., and Zanfrognini, B. *Polyhedron* **28**, 2029–2035 (2009).

[103] Gatteschi, D. *High Magnetic Fields - Applications in Condensed Matter Physics and Spectroscopy.* Springer, (2001).

[104] Barra, A.-L., Caneschi, A., Gatteschi, D., and Sessoli, R. *J. Am. Chem. Soc.* **117**, 8855–8856 (1995).

[105] Novoselov, K. S., Geim, A. K., Morozov, S. M., Jiang, D., Zhang, Y., Dubonos, S. V., Grigorieva, I. V., and Firsov, A. A. *Science* **306**, 666–669 (2004).

[106] Meyer, J. C., Geim, A. K., Katsnelson, M. I., Novoselov, K. S., Booth, T. J., and Roth, S. *Nature* **446**, 60–63 (2007).

[107] Geim, A. K. and Novoselov, K. S. *Nature Mat.* **6**, 183–191 (2007).

[108] Geim, A. K. and MacDonald, A. H. *Phys. Today* , 35–41 (2007).

[109] Wallace, P. R. *Phys. Rev.* **71**, 622–634 (1947).

[110] Novoselov, K. S., Geim, A. K., Morozov, S. M., Jiang, D., Katsnelson, M. I., Grigorieva, I. V., Dubonos, S. V., and Firsov, A. A. *Nature* **438**, 197–200 (2005).

[111] Zhang, Y., Tan, Y.-W., Stormer, H. L., and Kim, P. *Nature* **438**, 201–204 (2005).

[112] Katsnelson, M. I. *Mat. Today* **10**, 20–27 (2007).

[113] Castro Neto, A. H., Guinea, F., Peres, N. M. R., Novoselov, K. S., and Geim, A. K. *Rev. Mod. Phys.* **81**, 109–162 (2009).

[114] Orlita, M. and Potemski, M. *Semicond. Sci. Technol.* , to be published.

[115] Li, G., Lucian, A., and Andrei, E. Y. *Phys. Rev. Lett.* **102**(17), 176804 (2009).

[116] Slonczewski, J. C. and Weiss, P. R. *Phys. Rev.* **109**, 272–279 (1958).

[117] McClure, J. W. *Phys. Rev.* **108**, 612–618 (1957).

[118] Berger, C., Song, Z., T. Li, X. L., Ogbazghi, A. Y., Feng, R., Dai, Z., Marchenkov, A. N., Conrad, E. H., First, P. N., and de Heer, W. A. *J. Phys. Chem. B* **108**, 19912 (2004).

[119] de Heer, W. A., Berger, C., Wu, X., First, P. N., Conrad, E. H., Lu, X., Li, T., Sprinkle, M., Haas, J., Sadowski, M. L., and Martinez, M. P. G. *Solid State Commun.* **143**, 92–100 (2007).

[120] Berger, C., Song, Z., Li, X., Wu, X., Brown, N., c. Naud, Mayou, D., Li, T., Hass, J., Marchenkov, A. N., Conrad, E. H., First, P. N., and de Heer, W. A. *Science* **312**, 1191–1196 (2006).

[121] Hass, J., Varchon, F., Millán-Otoya, J. E., Sprinkle, M., Sharma, N., de Heer, W. A., Berger, C., First, P. N., Magaud, L., and Conrad, E. H. *Phys. Rev. Lett.* **100**, 125504 (2008).

[122] Sutter, P. W., Flege, J.-I., and Sutter, E. A. *Nature Mat.* **7**, 406–411 (2008).

[123] Vázques de Parga, A. L., Calleja, F., Borca, B., Passeggi, Jr., M. C. G., Hinarejos, J. J., Guinea, F., and Miranda, R. *Phys. Rev. Lett.* **100**, 056807 (2008).

[124] Grüneis, A., Attaccalite, C., Wirtz, L., Shiozawa, H., Saito, R., Pichler, T., , and Rubio, A. *Phys. Rev. B* **78**, 205425 (2008).

[125] Kim, K. S., Zhao, Y., Jang, H., Lee, S. Y., Kim, J. M., Kim, K. S., Ahn, J.-H., Kim, P., Choi, J.-Y., and Hong, B. H. *Nature* **457**, 706–710 (2009).

[126] Gruneis, A., Kummer, K., and Vyalikh, D. V. *New J. Phys.* **11**, 073050 (2009).

[127] Neugebauer, P., Orlita, M., Faugeras, C., Barra, A.-L., and Potemski, M. *Phys. Rev. Lett.* **103**, 136403 (2009).

[128] Sadowski, M. L., Martinez, G., Potemski, M., Berger, C., and de Heer, W. A. *Phys. Rev. Lett.* **97**, 266405 (2006).

[129] Novoselov, K. S., Jiang, Z., Zhang, Y., Morozov, S. V., Stormer, H. L., Zeitler, U., Maan, J. C., Boebinger, G. S., and nadA. K. Geim, P. K. *Science* **315**, 1379 (2007).

[130] Orlita, M., Faugeras, C., Plochocka, P., Neugebauer, P., Martinez, G., Maude, D. K., Barra, A.-L., Sprinkle, M., Berger, C., de Heer, W. A., and Potemski, M. *Phys. Rev. Lett.* **101**, 267601 (2008).

[131] Li, G. and Andrei, E. *Nature Phys.* **3**, 623 (2007).

[132] Miller, D. L., Kubista, K. D., Rutter, G. M., Ruan, M., de Heer, W. A., First, P. N., and Stroscio, J. A. *Science* **324**, 924–927 (2009).

[133] Jiang, Z., Henriksen, E. A., Tung, L. C., Wang, Y.-J., Schwartz, M. E., Han, M. Y., Kim, P., and Stormer, H. L. *Phys. Rev. Lett.* **98**, 197403 (2007).

[134] Gusynin, V. P., Sharapov, S. G., and Carbotte, J. P. *Phys. Rev. Lett.* **98**, 157402 (2007).

[135] Noziéres, P. *Phys. Rev.* **109**, 1510–1521 (1958).

[136] Brandt, N. B., Chidinov, S. M., and Ponomarev, Y. G. *Semimetals 1: Graphite and its Compounds*, volume 20.1 of *Modern Problems in Condensed Matter Sciences*. North-Holland, Amsterdam, (1988).

[137] Orlita, M., Faugeras, C., Martinez, G., Maude, D. K., Sadowski, M. L., and Potemski, M. *Phys. Rev. Lett.* **100**, 136403 (2008).

[138] Deacon, R. S., Chuang, K.-C., Nicholas, R. J., Novoselov, K. S., and Geim, A. K. *Phys. Rev. B* **76**, 081406 (2007).

[139] Li, Z., Henriksen, E. A., Jiang, Z., Hao, Z., Martin, M. C., Kim, P., Stormer, H. L., and Basov, D. N. *Nature Phys.* **4**(7), 532 July (2008).

[140] Toy, W. W., Dresselhaus, M. S., and Dresselhaus, G. *Phys. Rev. B* **15**, 4077 (1977).

[141] Morozov, S. V., Novoselov, K. S., Katsnelson, M. I., Schedin, F., Elias, D. C., Jaszczak, J. A., and Geim, A. K. *Phys. Rev. Lett.* **100**, 016602 (2008).

[142] Bolotin, K. I., Sikes, K. J., Hone, J., Stormer, H. L., and Kim, P. *Phys. Rev. Lett.* **101**, 096802 (2008).

[143] Tan, Y.-W., Zhang, Y., Bolotin, K., Zhao, Y., Adam, S., Hwang, E. H., Das Sarma, S., Stormer, H. L., and Kim, P. *Phys. Rev. Lett.* **99**, 246803 (2007).

[144] Du, X., Skachko, I., Barker, A., and Andrei, E. Y. *Nature Nanotech.* **3**, 491 (2008).

[145] Hwang, E. H. and Sarma, S. D. *Phys. Rev. B* **77**, 235437 (2008).

[146] Bychkov, Y. A. and Martinez, G. *Phys. Rev. B* **77**, 125417 (2008).

[147] Asano, K. and Ando, T. (2009).

[148] Allen, S. J., Tsui, D. C., and Logan, R. A. *Phys. Rev. Lett.* **38**(17), 980 (1977).

[149] Hwang, E. H. and Sarma, S. D. *Phys. Rev. B* **75**, 205418 (2007).

[150] Polini, M., MacDonald, A., and Vignale, G. (2009).

[151] Liu, X. and Furdyna, J. K. *J. Phys.: Condens. Matter* **18**(13), 245 (2006).

[152] Uchoa, B., Kotov, V. N., Peres, N. M. R., and Castro Neto, A. H. *Phys. Rev. Lett.* **101**(2), 026805 (2008).

[153] Yazyev, O. V. and Helm, L. *Phys. Rev. B* **75**(12), 125408 (2007).

[154] Yang, L., Cohen, M. L., and Louie, S. G. *Phys. Rev. Lett.* **101**(18), 186401 (2008).

[155] Červenka, J., Katsnelson, M. I., and Flipse, C. F. J. *Nature Phys.* **5**, 840 – 844 (2009).

[156] Martin, J., Akerman, N., Ulbricht, G., Lohmann, T., Smet, J. H., von Klitzing, K., and Yacoby, A. *Nature Phys.* **4**, 144 (2008).

[157] Galt, J. K., Yager, W. A., and H. W. Dail, J. *Phys. Rev.* **103**, 1586–1587 (1956).

[158] Williamson, S. J., Surma, M., Praddaude, H. C., Patten, R. A., and Furdyna, J. K. *Solid State Commun.* **4**, 37–41 (1966).

# Appendix A

# Basic Theory of the Gaussian Beam

The starting point for the derivation of the Gaussian beam is the Helmholz wave equation

$$\left(\nabla^2 + k^2\right)\psi = 0, \tag{A.1}$$

where the function $\psi$ represents either an electric $\mathbf{E}$ or a magnetic $\mathbf{B}$ field, and $k$ is the wave number, $k = 2\pi/\lambda$. We assume that the wave propagation is along the positive direction of the $z$ axis. Then the function $\psi$ is of the form:

$$\psi(x, y, z) = u(x, y, z)\exp(-ikz), \tag{A.2}$$

where $u$ is a complex scalar function. Based on this assumption, the Helmholz equation reads:

$$\frac{\partial^2\psi}{\partial x^2} + \frac{\partial^2\psi}{\partial y^2} + \frac{\partial^2\psi}{\partial z^2} + k^2\psi = 0. \tag{A.3}$$

Carrying out the partial derivatives we obtain the **reduced (quasi-plane) wave equation**:

$$\frac{\partial^2 u}{\partial x^2} + \frac{\partial^2 u}{\partial y^2} + \frac{\partial^2 u}{\partial z^2} - 2ik\frac{\partial u}{\partial z} = 0. \tag{A.4}$$

To derive the paraxial approximation two assumptions are needed. The variation of the amplitude $u$ has to be small over a distance comparable to the wavelength and the axial variation has to be small compared to the perpendicular variation of the propagation direction ($z$ axis). This leads to the final paraxial wave equation, where the third term is omitted because it is smaller than the other terms in the Eq. (A.4)

$$\frac{\partial^2 u}{\partial x^2} + \frac{\partial^2 u}{\partial y^2} - 2ik\frac{\partial u}{\partial z} = 0. \tag{A.5}$$

It is convenient to write the Eq. (A.5) using cylindric coordinates

$$\frac{\partial^2 u}{\partial r^2} + \frac{1}{r}\frac{\partial u}{\partial r} + \frac{1}{r}\frac{\partial^2 u}{\partial \varphi^2} - 2ik\frac{\partial u}{\partial z} = 0. \tag{A.6}$$

Assuming that there exist an axial symmetry around $z$ axis, the Eq. (A.6) is reduced to:

$$\frac{\partial^2 u}{\partial r^2} + \frac{1}{r}\frac{\partial u}{\partial r} - 2ik\frac{\partial u}{\partial z} = 0. \tag{A.7}$$

To solve the Eq. (A.7), we consider $u$ in the form of:

$$u(r,z) = A(z)\exp\left(\frac{-ikr^2}{2q(z)}\right), \tag{A.8}$$

where *A(z)* and *q(z)* are two complex functions, which remain to be determined. From the form of Eq. (A.8) we can see a similarity with the Gaussian distribution function:

$$f(x) = \frac{1}{\sigma\sqrt{2\pi}}\exp\left(\frac{-(x-\mu)^2}{2\sigma}\right). \tag{A.9}$$

This similarity is used for the next steps. To obtain the functions *A(z)* and *q(z)*, we insert (A.8) in (A.7) and get:

$$-2ik\left(\frac{A}{q} + \frac{\partial A}{\partial z}\right) + \frac{k^2 r^2 A}{q^2}\left(\frac{\partial q}{\partial z} + 1\right) = 0. \tag{A.10}$$

The Eq. (A.10) has a solution only if:

$$\frac{\partial A}{\partial z} = -\frac{A}{q} \qquad \text{and} \qquad \frac{\partial q}{\partial z} = 1. \tag{A.11}$$

We will consider $q$ in the form:

$$\frac{1}{q} = \frac{1}{\mathcal{R}(z)} - \frac{i\lambda}{\pi w(z)^2}, \tag{A.12}$$

where $\mathcal{R}(z)$ and $\omega(z)$ are the **wave front radius** and $w$ the **beam radius**, respectively, see Fig. 2.1. The $q$ is referred to as the **complex beam parameter** or the **Gaussian beam parameter**. We define the beam radius at $z = 0$:

$$w_0 = \left(\frac{\lambda q(0)}{i\pi}\right). \tag{A.13}$$

$w_0$ is called the **beam waist radius** or simply the **waist**. With this definition, we obtain the second important equation for the Gaussian beam parameter $q$:

$$q = \frac{i\pi w_0^2}{\lambda} + z. \tag{A.14}$$

Eqs. (A.12) and (A.14) allow us to obtain the final product of the derivation, i.e. the **wavefront radius** $\mathcal{R}$ and the **beam radius** $w$ as a function of $z$:

$$\boxed{\mathcal{R} = z + \frac{1}{z}\left(\frac{\pi w_0^2}{\lambda}\right)^2} \tag{A.15}$$

$$\boxed{w = w_0\left[1 + \left(\frac{\lambda z}{\pi w_0^2}\right)\right]^{1/2}}. \tag{A.16}$$

We should also add the equation for the **Gaussian beam phase shift** $\phi_0$ which comes out from the Eqs. (A.11)

$$\boxed{\tan\phi_0 = \frac{\lambda z}{\pi w_0^2}}. \tag{A.17}$$

The last three equations together with the normalized[1] electric field distribution *E(r,z)*, which is shown in the Fig. 2.1b and described by equation

$$\boxed{E(r,z) = \left(\frac{2}{\pi w^2}\right)^{1/2} \exp\left(\frac{-r^2}{w^2} - ikz - \frac{i\pi r^2}{\lambda\mathcal{R}} + i\phi_0\right)}, \tag{A.18}$$

completely describe the behaviour of the fundamental Gaussian beam mode in the paraxial approximation.

For practical purposes, it is useful to have inverse formulas of the equations for the beam waist $w_0$ and his location $z$. Dividing the wavefront radius $\mathcal{R}$, in Eq. (A.15), by the square of the beam radius $w^2$, in Eq. (A.16), we obtain the relation:

$$\frac{\pi w^2}{\lambda z} = \frac{\mathcal{R}\lambda}{\pi w_0^2}, \tag{A.19}$$

from which we can express $w_0$ and $z$:

$$w_0 = \frac{w}{[1 + (\pi w^2/\lambda\mathcal{R})^2]^{1/2}} \tag{A.20}$$

and

$$z = \frac{\mathcal{R}}{1 + (\lambda\mathcal{R}/\pi w^2)^2}. \tag{A.21}$$

[1]The power carried by the wave is proportional to the square of electric intensity $E$, thus the normalization is given by the integral over the area of the beam $\int_0^\infty \mid E \mid^2 \cdot 2\pi r dr = 1$.

# Appendix B

# Experiment Control and Data Acquisition (LabView)

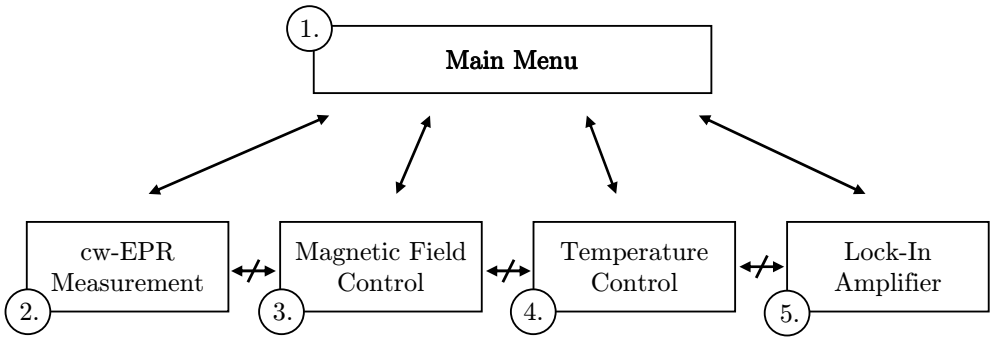


Figure B.1: Program diagram for cw-EPR experiments. Schematic diagram showing links between the main menu of the program (No. 1.) and other subprograms (No. 2., 3., 4. and 5.). The user interface with the corresponding numbers is shown in Fig. B.3.

The program used to control the EPR experiment was written in LabView 6.1. The block scheme of the final program is shown in Fig. B.1 where the user interface is depicted in Fig. B.3. The program is created in a way that even persons to whom the program has not been introduced should be able to safely control the experiment.
The program is organized in the following manner:

**1. Main Menu:** The program is controlled by the main menu (No. 1.). From the main menu the user can enter any subprogram (No. 2., 3., 4. or 5.). The main menu is organized in the following way. It allows opening and running only one subprogram. To run any other subprogram one has to close the currently used subprogram before opening a new subprogram from the main menu. This is illustrated in Fig. B.1 by double arrows.

**2. cw-EPR Measurement (Data Acquisition):** This is a subprogram which allows measuring cw-EPR spectra. After pressing the bar from the main menu a window with all the necessary basic information for cw-EPR measurements appears, see Fig. B.3. The basic parameters are the temperature, the range of the magnetic field and the sweeping rate of the magnet, which can be chosen only within limits of the system. The temperature cannot exceed 300 K and the minimal temperature is given by the intensity of pumping the

helium gas (about 1.5 K). The magnetic field can be swept in the range -12 to +12 T with a maximal sweeping rate 20 mT/s. The measurement can be interrupted in any moment and recorded spectra (if wanted) saved. The number of data points in each scan is limited to 16 000, giving a maximal resolution of a measurement 7.5 G for sweep from 0 to 12 T.

If desired, the subprogram allows accumulating of an arbitrary number of scans as well. After each scan (measurement), the following scan is launched, and the accumulated data are averaged with those already stored in memory. Such a cycle continues until the required number of accumulated scans is performed. Arbitrary number of scans can thus be collected without significant growth of the data size and without enhanced request on the hardware (memory).

**3. Magnetic Field and 4. Temperature Control:** Drivers, from Oxford Instruments upgraded to our needs, to control the magnetic field (IPS120-10) and the temperature (ITC503) in the allowed limits of the system.

**5. Lock-In Amplifier:** This subprogram allows reading and controlling the settings of the lock-in amplifier (Stanford SR830) such as the phase, the reference frequency, the sensitivity, the time constant etc.

Not all the experimental parameters can be controlled via the program. The modulation field $B_{mod}$ has to be adjusted manually, because we use an analog instrument (Ferisol GBT516) without any available communication interface. The parameters (frequency $f_{mod}$ and amplitude $B_{mod}$) of the modulation are read by the lock-in amplifier and by the multimeter (Keithley 175) via the GPIB interface. $B_{mod}$ is proportional to AC current in the modulation coil, and is written in the headings of the data file, see Fig. B.2. The modulation coils are calibrated and thus the AC current is directly associated to a proper modulation field $B_{mod}$.

The program allows future updates of either elemental instruments or allow us to implements new subprograms, e.i. a subprogram for the operation of the EPR spectrometer in the pulsed mode.

```
      Date: 02/03/2007                                          Time: 15:57
-------------------------------------------------------------------------------
Sample Name: Penta 3.2*10-4
Note: QO , iso
Frequency: 295.00 GHz
Field Modulation: 9.00 mA
Temperature: 10.00 K
Field:  From:   10.130 T
        To:     10.230 T
        Sweep:  0.80 mT/s
-------------------------------------------------------------------------------
Value/Parameter:                At Start:       At End:         Mean:
Magentic Field (IPS):           10.131 T        10.230 T        10.181 T
Temperature (ITC):              40.000 K        40.000 K        40.000 K
Modulation Field (Multimeter):  9.000 mA        9.000 mA        9.000 mA
Reference Frequency (Lock-In):  675.1 Hz        675.1 Hz        675.1 Hz
Phase of Reference (Lock-In):   174.62 °        174.62 °
Sensitivity (Lock-In):          500 uV/pA       500 uV/pA
Time Constant  (Lock-In):       300 ms          300 ms
Pass Fileter Slope (Lock-In):   12 dB/oct       12 dB/oct
Reserve mode (Lock-In):         Normal          Normal
-------------------------------------------------------------------------------
Number of points: 529
Time of one measurment: 123.7 s
Average: 1
Time of whole measurment (approximately): 123.7 s ( 1 x 123.7 )
-------------------------------------------------------------------------------

 Field. X Y
 10.131175 -1.579530E-6 447.037000E-9
 10.131351 -1.609330E-6 596.050000E-9
 10.131539 -774.864000E-9 1.013290E-6
```

Figure B.2: Heading of a data file.

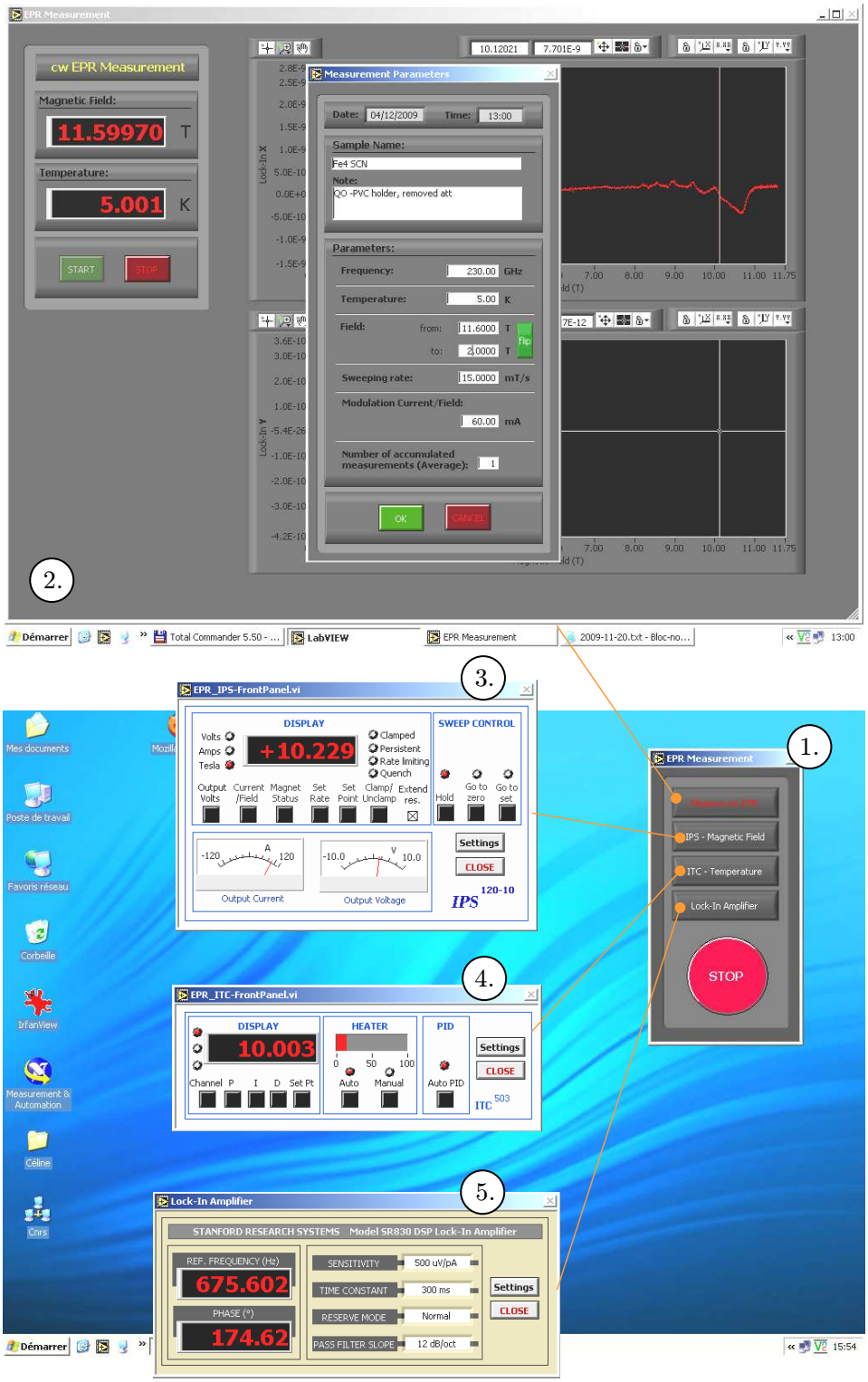


Figure B.3: The user interface of the program for EPR experiments: 1. Main menu of the program, 2. Window of the cw-EPR measurement, where user controls parameters of the measurements, 3., 4. and 5. control panels of the power supply of the superconducting magnet (Oxford Instruments IPS120), the variable temperature insert (VTI) (Oxford Instruments ITC503) and the lock-in amplifier (Stanford SR830).

# Appendix C

# Preparation of Meshes by UV-Lithography

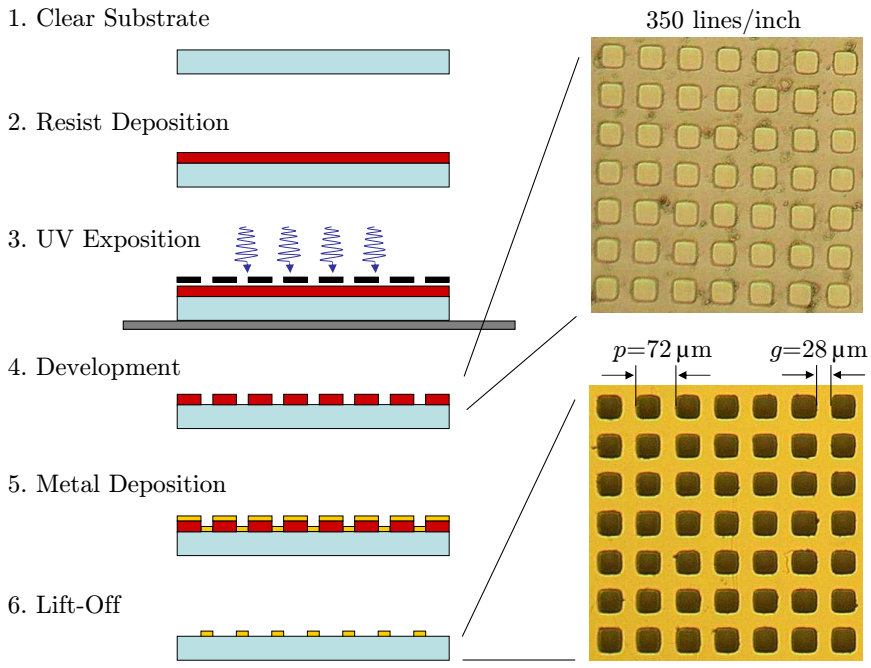


Figure C.1: UV-lithographical process is split into six subsequent steps explained in the text. Two images on the righthand site show the inductive mesh in the $4^{th}$ (before reactive etching) and $6^{th}$ steps of the preparation.

Inductive meshes of squared symmetry can be used as planar non-polarizing semitransparent mirrors for MWs [72, 73] in a half-symmetric FP resonator. The MW is coupled into the FP resonator using a mesh. Hence, the performance of the FP resonators is directly affected by the quality of the mesh.

The commercially available meshes are often prepared by the electroforming[1]. The electroformed meshes are thin freestanding sheets which cause difficulties in manipulation. The fine mesh has to be carefully stretched on a suitable dielectric substrate. The different

[1]The commercially available meshes can be bought from Buckbee-Mears or any suppliers for electron microscopy.

temperature expansion coefficients of meshes (metals) and substrates (dielectrics) can lead to serious distortions of the meshes at cryogenic temperatures. These difficulties together with size limitations of commercially available meshes mean that these meshes are not very suitable for EPR applications.

The meshes prepared by photolithographical methods, on a suitable dielectric substrate, allow to create metallic meshes of arbitrary shapes. The mesh is easy to handle and to manipulate with. The substrate, on which the mesh is created preserves the mesh geometry even at cryogenic temperatures.

In our work, we take advantage of the lab facility and we mainly concentrate on inductive meshes prepared by the UV-lithographical process, Table 4.4, for which either glass or quartz microscopy cover slips are used as substrates. The UV-lithographical technique together with the plasma sputtering of metals allow us to create meshes of very high quality, including the mechanical stability, high metal conductance and precision within micrometres.

In the following text, we describe the fabrication of meshes which we divide into six subsequent steps, see Fig. C.1.

1. **Substrate Cleaning:** The metallic meshes are created on microscope cover slips of thickness $t < 20\,\mu$m. The cover slips were made either from BK7 (borosilicate glass), Gold-Seal®(pre-selected, pre-cleaned silicate glass - fused silica) or quartz. The substrate (a cover slip) is first washed in an acetone bath and ultrasound, for couple of minutes, and finally dried by nitrogen gas.

2. **Resist Deposition:** The photolithographical negative resist S1818 is uniformly deposited over the clean substrate by spin coating. Suitable set of spinning parameters (rotation speed 4000 rpm, acceleration 400 rpm/s and time of spinning 30 second) creates a 1.8 $\mu$m thick film of the resist. The resist on the substrate is then baked for 1 minute at temperature of 115 °C before the UV exposition.

3. **UV Exposition:** The substrate with the resist, placed on a supporting silicon wafer[2], is exposed to UV radiation (mercury lamp) through a mask (Table 4.4). The negative mask, according to the S1818 resist, is designed in the CleWin software and printed on a UV transparent plastic sheet by a 6000 dpi resolution printer (Laser Technologie, Trappes France). The exposition time depends on the resist itself, as well as on the UV radiation intensity and has to be calculated, or found empirically. In our case, the theoretical resist exposition time is around 25 s for the actually measured intensity of mercury lamp. However, the UV light is reflected/scattered on the supporting silicon wafer and, as the UV transparent substrate has a finite thickness, creeps under the mask. This unwanted backward reflected irradiation causes deformations of the edges of the final mesh. To prevent this unwanted issue the exposition time has to be decreased and found empirically.

4. **Development:** After the exposition, the resist is developed. The exposed resist is developed (removed) by a concentrated developer mixed 1:1 with distilled water. After 50 s of shaking in the developer, the substrate is washed in flowing deionized water to remove rests of the resist. The substrate is then dried by nitrogen gas (Fig. C.1).

[2]The wafer is used as a mirror for transparent cover slip.

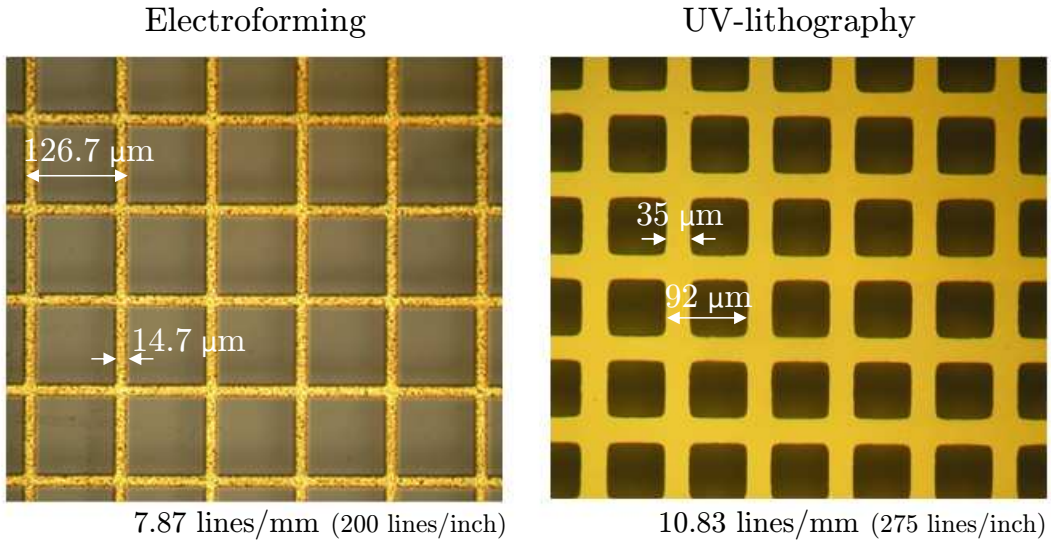


Figure C.2: Qualitative comparison of two inductive meshes one prepared by electroforming (left) and the second one by UV-lithography (right). The quality of the surface is apparent from the figure. Whereas the mesh prepared by electroforming has rough and grainy metallic surface, the mesh made by UV-lithography and deposited by sputtering has a smooth and clean surface leading to smaller resistive losses with respect to meshes prepared by electroforming.

The time of the resist developing is often known approximately. However, the optimal time has to be found empirically. If a reactive plasma etching is available, it can be used to remove rests of the resist.

5. **Metal Deposition:** The substrate, with the pattern created by the resist on, is now prepared for the metal (Cu or Au) deposition. In spite of the better conductivity (reflectivity) of copper, see Table 4.1, gold is preferred due to its chemical stability. For the metal deposition, we use a sputtering apparatus accessible in the Institute Néel. Before the gold deposition, a transfer layer composed of easily oxidized metals (Ti, Al or Cr) is sputtered. The transfer layer is used to improve adhesion and chemical bonding of the deposited metal to the oxidized substrate. A transfer layer of about 5 nm thick is created and then the metal of the mesh itself is deposited. The thickness of the mesh is in the range from 250 to 300 nm. The mesh thickness has to be few times greater than the skin depth $\delta$, see Table 4.1. The typical theoretical value of the skin depth for well conducting metals is about 150 nm at room temperature and for the MW frequency 285 GHz. However, the skin depth decreases with the temperature and reaches tens of nanometres at cryogenic temperatures, i.e. at the operation temperature of the FP resonator. The thickness of the mesh plays an important role for the estimation of the losses as well. The ideal mesh is very thin but at certain thickness the roughness and the quality of the thin metal become very important parameters [72].

6. **Lift-Off** After the metal deposition, the lift-off in a solvent is made. The solvent removes the resist with the metal deposited on top of it. For the lift-off process, generally 2-3 hours are needed depending on the solvent. As a solvent, we use acetone, trichlorethan or tetrachlormethan. However, the "Microdeposit remover 1165",

where the lift-off process is evidently faster than in the previous solvents was found to be the most suitable. To accelerate the lift-off, the ultrasound can be applied. Nevertheless, the agitation by hand is preferable. Very strong ultrasound can cause serious damage of the meshes. Finally, when all the resist is removed, the mesh is washed from the solvent by ethanol or by deionized water, and dried by nitrogen gas.

The UV lithography is a simple technique which enables the preparation of the high quality meshes with parameters optimized for our needs. If the sputtering or a vapor deposition is used for the metal deposition, the surface of the metal is smooth and the resistance of the mesh is close to theoretical value [53], see figure Fig. C.2 (comparison of meshes prepared by electroforming and UV lithography). The list of meshes prepared by UV-lithography is given in Table 4.4.

The UV lithography and the metal deposition were performed at Institut Néel in Grenoble with kind permission of Dr. W. Wernsdorfer and Dr. L. Ranno.

# Appendix D

# Cyclotron Resonance on Natural Graphite

The crystal of graphite (Fig. D.1) can be considered as many graphene sheet coupled together with so-called Bernal stacking (AB). The band structure of bulk graphite was well described by Slonczewski-Weiss-McClure (SWM) model [116, 117]. The first cyclotron resonance recorded by J. K. Galt *et al.* at $\omega_c$=24 GHz [157] was used to determine the effective mass of the electron and was analyzed by P. Nozières [135]. Later on, S. J. Williamson *et al.* [158] performed further cyclotron resonance measurements. Their data were however not rich and thus not easy to interpret. Here we report an cyclotron resonance measurements recorded at sub THz frequencies, i.e. meV energies (Fig. D.2).

Galt and Williamson found that resonance positions scale as $\hbar\omega_c/B \approx 2.0\,\mathrm{meV/T}$ which correspond to an effective mass of electrons $m^* = 0.057m_0$, together with two series of harmonics:

$$\hbar\omega_c(3N+1)N = 0, 1, 2, ... \tag{D.1}$$

$$\hbar\omega_c(3N-1)N = 1, 2, 3, ... \tag{D.2}$$

The $3N+1$ and $3N-1$ series can be understood by considering trigonal warping around the $K$ point of the Brillouin zone of graphite.

In our data we observe the same behaviour. In Fig. 6.6 the cyclotron resonance at 5 K and at 283.2 GHz (1.17 meV) is shown. The basic resonance frequency is observed for a magnetic field close to $B = 0.6\,\mathrm{T}$ ($B = -0.6\,\mathrm{T}$) marked by black arrows in the Fig. 6.6. As the peaks are periodic in $B^{-1}$ the same plot (Fig. 6.6) can be plotted in normalized units $\omega/\omega_c$ (Fig. D.3), where the periodicity of the harmonics is demonstrated. In Fig. D.3, the observed harmonics for $\hbar\omega_c(3N+1)$ are assigned by blue arrows and for $\hbar\omega_c(3N-1)$ by red arrows.

The experiment was also performed at other frequencies. The cyclotron resonance positions are plotted in Fig. D.2 revealing a linear dependence on exciting energy $\hbar\omega_c$.

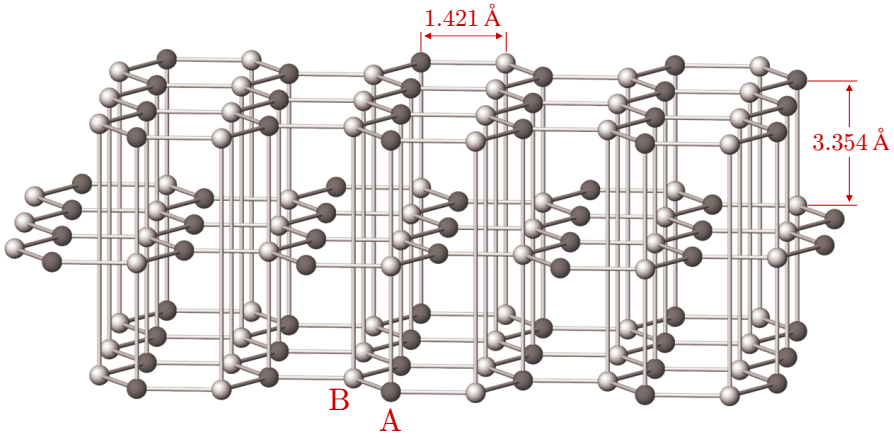


Figure D.1: Crystal structure of graphite. Bulk graphite consists of many coupled graphene sheets which are Bernal stacked (AB). Picture reprinted with a kind permission of J. Schneider.

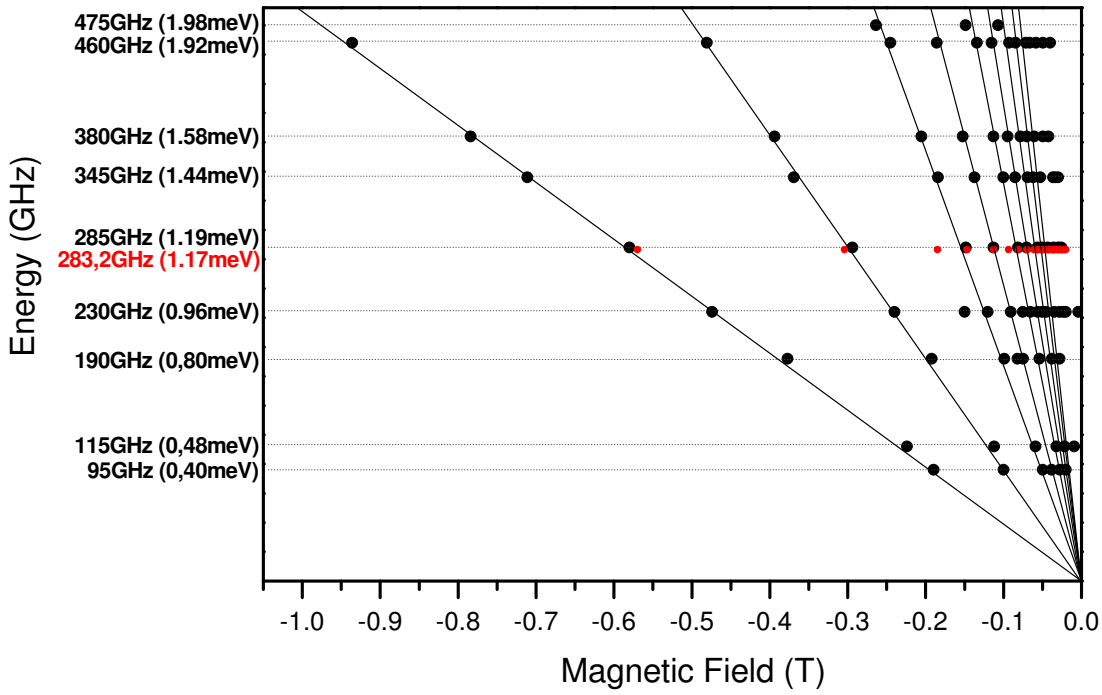


Figure D.2: The cyclotron resonance positions taken from recordings on several frequencies, scaling linearly with the exciting energy $\hbar\omega_c$.

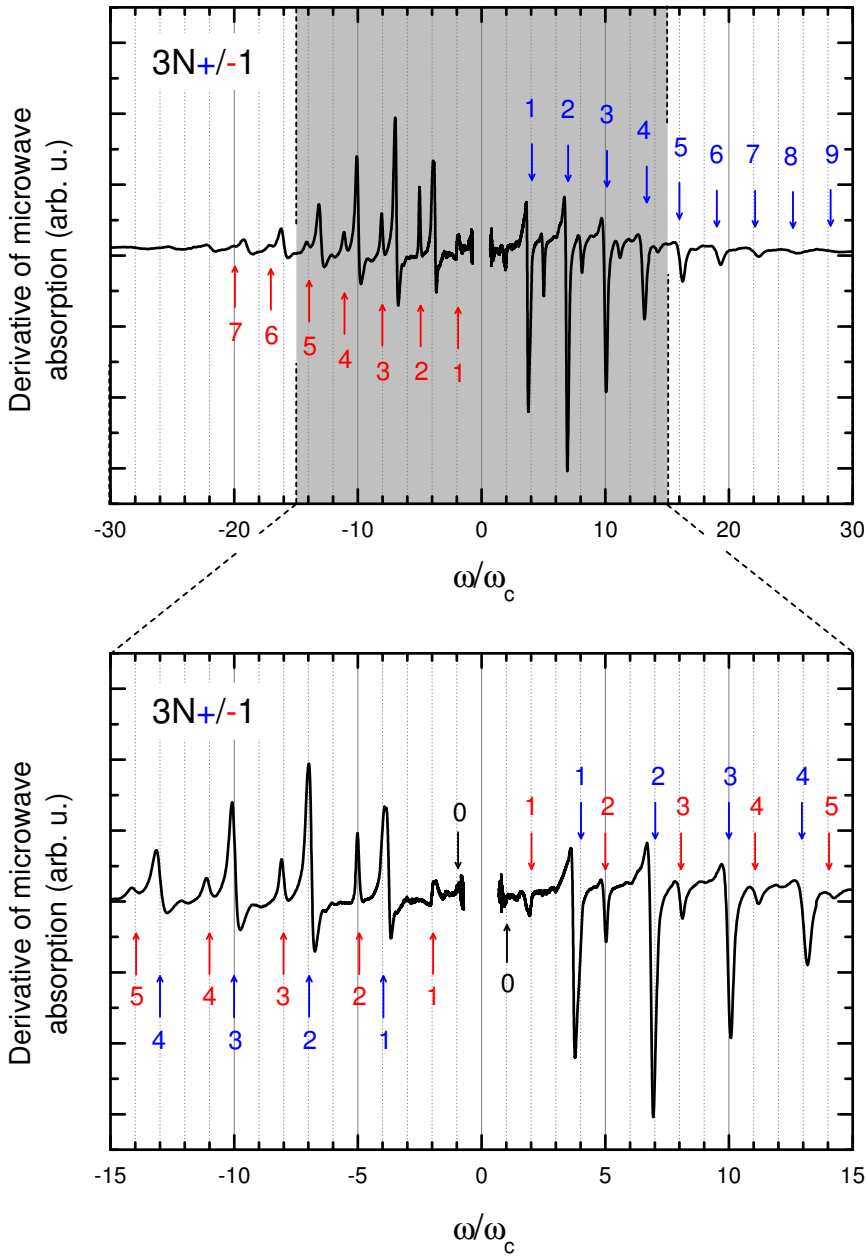


Figure D.3: Magneto-absorption spectra of natural graphite from Fig. 6.6 normalized to a MW frequency 283.2 GHz in units of $\omega/\omega_c$. The figure clearly shows the consequences of trigonal warping. i.e. two series of CR harmonics explained in text. The black arrow denotes the basic cyclotron resonance at 2.05 meV/T

# Appendix E

# List of Publications

**P. Neugebauer** and A.-L. Barra
"New Cavity Design for Broad-band Quasi-Optical HF-EPR spectroscopy"
Appl. Magn. Res. **37**, 833-843 (2010)

**P. Neugebauer**, M. Orlita, C. Faugeras, A.-L. Barra and M. Potemski
"How perfect can graphene be?"
Phys. Rev. Lett. **103**, 136403 (2009)

L. Gregoli, C. Danieli, A.-L. Barra, **P. Neugebauer**, G. Pellegrino, G. Poneti, R. Sessoli and A. Cornia
"Magnetostructural Correlations in Tetrairon(III) Single-Molecule Magnets"
Chem. Eur. J. **15**, 6456-6467 (2009)

M. Orlita, C. Faugeras, P. Plochocka, **P. Neugebauer**, G. Martinez, D. K. Maude, A.-L. Barra, M. Sprinkle, C. Berger, W. A. de Heer and M. Potemski
"Approaching the Dirac Point in High-Mobility Multilayer Epitaxial Graphene"
Phys. Rev. Lett. **101**, 267601 (2008)

C. Aronica, Y. Chumakov, E. Jeanneau, D. Luneau, **P. Neugebauer**, A.-L. Barra, B. Gillon, A. Goujon, A. Cousson, J. Tercero and E. Ruiz
"Structure, Magnetic Properties, Polarized Neutron Diffraction, and Theoretical Study of a Copper(II) Cubane"
Chem. Eur. J. **14**, 9540-9548 (2008)

## Développement d'un Spectromètre de Résonance Paramagnétique Électronique Haute Fréquence / Haut Champ Hétérodyne fonctionnant autour de 285 GHz

Le travail de cette thèse concerne le développement d'un spectromètre de résonance paramagnétique électronique haute fréquence en mode continu (RPE-HF en mode continu) existant au laboratoire pour l'utiliser en mode pulsé. Cette thèse est divisée en deux parties: la première, technique, décrit les essais entrepris pour développer un spectromètre RPE-HF opérant à 283 GHz en mode pulsé; la seconde, expérimentale, a permis d'appliquer cet outil pour l'étude de molécules aimants (SMMs) et de monocouches de graphite (graphène). La partie dédiée au développement donne une description détaillée du spectromètre RPE-HF ainsi que les bases de la propagation Quasi-Optique. Cette partie théorique (résumée) est appliquée au pont "quasi-optique" déjà existant utilisé pour la propagation des micro-ondes (MW) et à la construction d'un résonateur Fabry-Pérot. Le signal RPE est enregistré par un détecteur superhétérodyne optimisé pour une fréquence de 283.2 GHz, utilisé en remplacement du bolomètre valable uniquement pour des mesures multifréquences en mode continu. La conception et la construction d'un résonateur Fabry-Pérot (FP), nécessaire pour augmenter la puissance d'excitation MW, sont aussi décrites en détail ainsi que le porte-échantillon tournant nouvellement développé pour l'étude des monocristaux. Ces deux nouveaux systèmes ont ensuite été utilisés avec succès dans la partie expérimentale de cette thèse (deux chapitres). D'abord, une étude complète de molécules-aimants de tétrafer(III) a été réalisée. Après une étude sur poudre, celle sur monocristal réalisée avec le porte-échantillon tournant a permis d'obtenir des paramètres plus précis pour l'anisotropie magnétique des complexes, ce qui est nécessaire pour mieux comprendre les processus de relaxation. Le second chapitre expérimental est dédié au graphène (cristal 2D). Dans ce chapitre, la haute performance de la cavité Fabry-Pérot a permis la mise en évidence de graphène de qualité exceptionnelle caractérisé par une mobilité des porteurs de charge dépassant $10^7$ cm$^2$/(V.s).

**Mots Clés:** RPE-HF, détection hétérodyne, résonateur Fabry - Pérot, magnétisme moléculaire, complexes tétranucléaires de fer(III), graphène

## Development of a Heterodyne High Field / High Frequency Electron Paramagnetic Resonance Spectrometer at 285 GHz

The thesis is devoted to an extension of the existing continuous wave high frequency electron paramagnetic resonance (cw-HF-EPR) spectrometer in order to work in a pulsed mode. The thesis is split into two parts. Whereas the first part is devoted to our attempt to develop a pulsed HF-EPR spectrometer which operates close to 285 GHz, the second experimental part illustrates the application of the technical developments presented in the first part to the study of single molecule magnets (SMMs) and of single layers of graphite (graphene). In the development part, a detailed description of the HF-EPR spectrometer is given together with the basis of Quasi-Optical propagation. This theoretical summary is then applied to the existing quasi-optical bridge for the propagation of microwave (MW) and to the building up of a Fabry-Pérot resonator. The EPR signal is recorded by a superheterodyne detector optimised for a 283.2 GHz frequency, which was implemented during this work and replaces a slow bolometeric detection suitable only for multi-frequency cw-HF-EPR. The design and construction of a Fabry - Pérot (FP) resonator, necessary to enhance the MW excitation power, are also described in detail together with a newly developed rotating holder for single crystal studies. These two new devices were then successfully applied in the experimental part of the thesis (two chapters). First, a complete study of tetrairon(III) Single-Molecule Magnets was performed. After a powder study, a single crystal study performed with the rotating sample holder allowed obtaining refined parameters for the magnetic anisotropy, which are necessary for a deeper understanding of the relaxation processes. The second experimental chapter is devoted to graphene (2D crystal). In this chapter, the high performance of the Fabry-Prot cavity led to the observation of outstanding quality of graphene expressed by a charge carrier mobility exceeding $10^7$ cm$^2$/(V.s).

**Keywords:** HF-EPR, heterodyne detection, Fabry - Pérot resonator, molecular magnetism, tetrairon(III) complexes, graphene